

A feasibility study of electrorotation as an alternative to impedance measurements

Characterization of single biological cells and spheroidal particles

Anders Jansen



Thesis submitted for a degree of
Master of Science (M.Sc.)
Electronics and Computer Technology
Medical Technology
60 Credits

Department of Physics
Faculty of Mathematics and Natural Sciences
University of Oslo

Spring 2018

dedication (optional)

Acknowledgements and Dedications

I would like to thank all that helped me so much throughout this thesis. Special thanks goes to my supervisor Ørjan G. Martisen that never gave up on me. A large thank to ELAB at the Department of Physics for all help.

To all fellow students, the whole of ELDAT and all others that helped me in my thesis. Thank you.

Abstract

Most common method for manipulating particles by applying an external electric field to a medium holding polarizable particles is a technique called dielectrophoresis. This is a method that we can observe effects of interactions between a dipole which acts in phase with the applied electric field. However, there are other techniques and methods that are closely related as a second class of AC electrokinetic phenomena which depend on the interactions between out-of-phase dipole spatially moving electric field. An induced dipole may experience force with both out-of-phase and in-phase components simultaneously. The induced forces will be experienced at the same moment of time due to these components with the respective induced forces being superimposed.

Electrorotation is one of these methods. If a polarizable particle is placed in a rotating electric field (usually suspended in an aqueous medium) the particle should rotate in perfect synchrony with the applied electric field. However, if the angular frequency of the rotating field becomes sufficiently large enough, the time taken for the dipole to "re-form" (*the relaxation time* of the dipole) according to the rotating field orientation becomes a significant factor. The dipole will lag behind the field frequency and results in a nonzero angle between field and dipole. This will induce a torque in the particle and cause it to rotate asynchronously with the field. This asynchronous lag can cause either a co-field or anti-field rotation direction depending on the properties of the medium and particle and if the phase-lag is less or more than 180°

The electrorotation spectra obtained in this thesis contained the transition through both dispersions describing electrorotation had been performed on the yeast cell for the given frequency range. This was the proof of concept and electrorotation on yeast cells had been reproduced according to similar electrorotation experiments on yeast cells.

Abbreviations

AC	=	Alternating Current
CCD	=	Charged Couple Device
CMF	=	Clausius Mossotti Factor
COV	=	Curvature of field
DC	=	Direct Current
DP	=	Dielectrophoresis
DEP	=	Dielectrophoresis
IC	=	Integrated Circuit
ED	=	Electrodeformation
EO	=	Electro-Orientation
ER	=	Electrorotation
FOV	=	Field Of View
FPS	=	Frames Per Second
MP	=	Mega Pixel
NA	=	Numerical Aperture
PSF	=	Point-Spread Function
PCB	=	Printed Circuit Board
RC	=	Resistor-capacitor
ROT	=	Electrorotation spectra
UIO	=	The University of Oslo

Table of Contents

Acknowledgements and Dedications	i
Abstract	iii
Abbreviations	v
Table of Contents	x
List of Tables	xi
List of Figures	xvi
1 Introduction	1
2 Basic Theory	5
2.1 Electrorotation	5
2.1.1 Introduction	5
2.1.2 Theory: general part	7
2.1.2.1 General theory of electrorotation (ER)	10
2.1.2.2 Brief introduction to dielectrophoresis (DP) and electrodeformation (ED)	12
2.1.2.3 Electro-orientation (EO)	15
2.1.2.4 Shelled particle models and polarizability	16
2.1.2.5 Electrorotation spectrum's ROT, characteristic frequency and external conductivity correlation	24

TABLE OF CONTENTS

2.1.2.6	Characteristic equations derived and explained by RC-models	29
2.1.2.7	Electric field variations due to shape and design of the electrodes	35
2.1.2.8	Rotational direction and other linked parameters	39
2.1.2.9	DC and electrode deterioration	44
2.2	Optical microscopy	46
2.2.1	Introduction	46
2.2.2	Köhler illumination	46
2.2.3	Numerical aperture of condenser and objective	47
2.2.3.1	Condensers numerical aperture	47
2.2.3.2	Numerical aperture of the objective	48
2.2.4	Microscope Resolution	50
2.2.4.1	Airy discs and George Biddell Airy	50
2.2.4.2	Abbe's Diffraction Limit (1873)	52
2.2.4.3	The Rayleigh Criterion	55
2.2.4.4	Matching camera and optical resolution	56
3	Method and materials	59
3.1	Introduction	59
3.2	The circuit from paper sketch to final design	61
3.2.1	The electrode chamber	61
3.2.2	PCB - Design, production and assembly	64
3.2.2.1	PCB design	64
3.2.2.2	Manufacturing the PCB	68
3.2.3	Extending the volume capacity of well in the electrode chamber	70
3.3	Preparation of yeast cell samples and storage	71
3.4	Cleaning routines for the electrode chamber	73
3.5	Calibration of oscilloscope probes	75
3.6	The microscope setup	76
3.6.1	Microscope calibration and setup	76
3.6.2	Resolution limitation calculations of the camera needed	78

3.7	Conductivity measurements of sterile water against two different populations of yeast emulsions	79
3.8	Anomalies concerning signal output characteristics	80
3.9	Counting cell rotations	80
4	Results	83
4.1	Introduction	83
4.2	Electrorotation spectrum's for <i>Saccharomyces cerevisiae</i>	83
4.3	Conductivity measurements	89
4.4	Relation measurements between signal input magnitudes and supply voltage (Vcc)	90
5	Discussion	95
5.1	A broad analysis of the system setup	95
5.1.1	Ensuring the accuracy of the results and the reproducibility	96
5.1.2	Choosing the system setup for the specific task	97
5.1.2.1	Suitability of the microscope system	97
5.1.2.2	Suitability of the electrorotation chamber	98
5.1.3	Suitability of yeast samples	102
5.1.4	Performance deviation due to the amplitude relation of signal and supply voltage for the integrated circuit	103
5.2	Measurement analysis of the electrorotation spectra	106
6	Conclusion and future progress	111
	Bibliography	113
	Appendix	i
A	First appendix - The depolarizing factors	i
B	Second appendix - Equipment used in thesis	iii
C	Third appendix - Data sheet for Idun dry bakers yeast	vii
D	Fourth appendix -Electrorotation test-sessions for completed and non-completed testing series on yeast	ix
E	Fifth appendix - Additional theory regarding the art of microscopy . .	xi

TABLE OF CONTENTS

F	Sixt appendix - Calculations of characteristic equations based on RC models	xvii
---	---	------

List of Tables

3.1	Truth table for the ER-device proving the signal measurements from figure.3.5	64
3.2	Pre-calculations for matching optical resolution of microscope system to camera.	79
4.1	Conductivity measurements for sterile water and yeast cell emulsion over time .	89
6.1	Equipment list (appendix)	v
6.2	Electrorotation test-sessions for completed and non-completed series on yeast (appendix)	x

List of Figures

2.1	Shell models	16
2.2	A spheroidal dielectric particle situated in a uniform electric field.	17
2.3	Air and water models for polarization.	19
2.4	Influential radius showed for potential difference of a spherical object.	21
2.5	Equipotential plane distribution through and around a spherical single-shelled model.	23
2.6	Typical electrorotation and dielectrophoresis spectrum. The imaginary part of the CMF is the plot with the two characteristic peaks R1 and R2 which represent electrorotation and the plot having two characteristic frequencies denoted as f_{ct1} and f_{ct2} represents the real part of the CMF and is the dielectrophoresis spectrum.	25
2.7	Electrorotation spectrum of <i>Saccharomyces cerevisiae</i> in different conductivity levels for the external medium	27
2.8	Electrorotation spectra of yeast cell for different values of conductivity of the external medium	28
2.9	Combined ER and DEP spectrum of Schematic DP ($\text{Real}_{\text{CMF}^*}$) and ER ($\text{Imag}_{\text{CMF}^*}$)	29
2.10	CMF at maximum and minimum described by the depolarizing factor	32
2.11	Figure (left) is an Rc model consisting of RC pairs i,m and e describing the inner media, the membrane and the external media, respectively. Ψ_e is given in equation.2.1.29 and is the reference potential in the external solution at distance r from the symmetry plane. Over the membrane thickness d the potential difference $\Delta\Psi_m^*$ is induced. The denotation n is the depolarizing factor (see appendix.A).	32

2.12	<i>"Criteria and simplified schemes for the derivation of the DP (a) and ER (b) spectra characteristics"</i> (Gimsa and Wachner, 1999) according to figure.2.9. Image source: (Gimsa and Wachner, 1999).	33
2.13	36
2.14	36
2.15	Deviation in torque and electric field strength according to different electrode designs	37
2.16	Electrode designs of different shapes simulations	38
2.17	The concept of numeric aperture and for objectives and condensers	48
2.18	Immersion medium and numerical aperture	49
2.19	Airy disc and airy disc pattern	51
2.20	Resolution Limit Imposed by Wave Nature of Light	54
2.21	Rayleigh Criterion	56
3.1	The letter from Professor J. Gimsa describing how to get started to construct a basic electrorotation device.	60
3.2	Arc of the the electrode tip. Radius of the arc was 0.285 mm resulting in a electrode width of 0.57 mm or 570 μm	61
3.3	Measurements of electrode chambers sides, center cavity and electrode distance.	62
3.4	Substrate thickness and center cavity of the top substrate	63
3.5	Signal measurements done at the electronics laboratory at UIO.	64
3.6	Schematics for prototype electrorotation device made in Cadstar 17.0. This was the final setup that was used to produce the final PCB.	66
3.7	Routing schematics for prototype electrorotation device made in Cadstar 17.0. This was the final setup that was used to produce the final PCB.	67
3.8	PCB finished etched top and the bottom ground layer. ground	69
3.9	PCB top layer with fitted IC and electrode chamber at its respective placement.	69
3.10	The parafilm rings attached to the top substrate of the electrode chamber increasing the volume capacity of the well.	71
3.11	Illustrates the level of cleanliness obtained on the electrode chamber using certified cleanroom wipes and swabs	74

3.12	Calibration of the probe after the internal square wave generator on the oscilloscope.	75
3.13	Microscope objectives for the used microscope system	77
3.14	Calibration slides tested to ensure the yeast cells would be resolvable of the microscope setup.	78
4.1	ROT spectrum for series 1 Vcc 4V Signal 4V	84
4.2	ROT spectrum for series 2 - Vcc 4V Signal 4V	85
4.3	ROT spectrum for series 4 - Vcc 4V Signal 4V	85
4.4	ROT spectrum for series 7 - Vcc 4V Signal 4V	86
4.5	ROT spectrum for series 8 - Vcc 4V Signal 4V	86
4.6	ROT spectrum for series 2 Vcc 5V Signal 5V	87
4.7	ROT spectrum for series 3 Vcc 5V Signal 5V	87
4.8	ROT spectrum for series 7 Vcc 5V Signal 5V	88
4.9	ROT spectrum for series 11 Vcc 5V Signal 5V	88
4.10	Conductivity measurements for sterile water and yeast cell emulsion over time .	89
4.11	Similarities in a discontinuous and contentious ROT spectrum.	91
4.12	Differences in the output signal related to magnitude setting for the supply voltage and signal input.	92
4.13	Differences in the output signal related to magnitude setting for the supply voltage and signal input.	93
4.14	Differences in the output signal related to magnitude setting for the supply voltage and signal input.	94
5.1	Illustration shows how the protection diode is connected to the Vcc terminal. The connection path through the diode, Vcc terminal and further back to the voltage source have more or less no resistance. This will be the path of least resistance and how the diode protects the IC against sudden fluctuations on the signal input.	105
5.2	ROT spectrum for series 8 - Vcc 4V Signal 4V with calculated spectrum	107
5.3	Standard parameters for model calculations on the single-shell spheroid	110
6.1	Conjugate focal planes in the microscope for Köhler illumination	xi

LIST OF FIGURES

6.2	Spherical aberration	xiii
6.3	Coma aberration	xiv
6.4	Coma aberration	xiv
6.5	Curvature of field	xv
6.6	Distortion	xv
6.7	Spherical aberration	xvi
6.8	Spherical aberration	xvi
6.9	First rotaion peak (R1)	xviii
6.10	Second rotaion peak (R2)	xix
6.11	First characteristic frequency (Fc1)	xx
6.12	First characteristic frequency (Fc2)	xxi

Introduction

This chapter describes the goals for this thesis and the background of the project. A short introduction to what the electrokinetic effect of electrorotation is presented.

The foundation of this thesis evolved from an academic collaboration between the School of Pharmacy (FAI), The Department of Physics (FI) and the Radiumhospital - Oslo University Hospital (OUS). The main title of the project is "Improving Medical diagnostics - Affinity for Impedance". The project is divided into three separate segments named Work package #1 to Work package #3. The two first segments are part of a post-doc and a Ph.D. study. Work package #3 was named "*The possibilities*" with under-title "*explore real-time properties of impedance derived electroanalysis for optimization of mass spectrometry-based medical diagnostic protocols.*". Professor Ørjan G. Martinsen is the supervisor for this thesis and has a central role in the project.

Electrorotation had been presented to Professor Martinsen years in advance through a colleague from the University of Rostock, and as an alternative approach to impedance measurements, electrorotation was chosen to be more closely investigated as a possible alternative for characterization of biological cells. Studies on electrorotation have not been performed at the University of Oslo before, so this thesis was outlined as a feasibility study where two primary goals were decided upon as well as a last third optional goal were implemented in the thesis description dependent on the progression of the two first primary goals.

The two primary goals of this thesis have been first, acquire a profound understanding of the theoretical concepts of electrorotation and to design, prototype and produce an electroro-

tation device. The second primary goal has been to perform electrorotation measurements on yeast cells (*Saccharomyces cerevisiae*), analyze the results and establish a connection to the theoretical concept of electrorotation. The third optional goal was to perform electrorotation measurements on treated and untreated biomagnetic beads for characterization and analytical purposes.

Most common method for manipulating particles by applying an external electric field to a medium holding polarizable particles is a technique called dielectrophoresis. This is a method that we can observe effects of interactions between a dipole which acts in phase with the applied electric field. However, there are other techniques and methods that are closely related as a second class of AC electrokinetic phenomena which depend on the interactions between out-of-phase dipole spatially moving electric field. An induced dipole may experience force with both out-of-phase and in-phase components simultaneously. The induced forces will be experienced at the same moment of time due to these components with the respective induced forces being superimposed (Goddard et al., n.d.).

Electrorotation is one of these methods. If a polarizable particle is placed in a rotating electric field (usually suspended in an aqueous medium) the particle should rotate in perfect synchrony with the applied electric field. However, if the angular frequency of the rotating field becomes sufficiently large enough, the time taken for the dipole to "re-form" (*the relaxation time* of the dipole) according to the rotating field orientation becomes a significant factor. The dipole will lag behind the field frequency and results in a nonzero angle between field and dipole. This will induce a torque in the particle and cause it to rotate asynchronously with the field. This asynchronous lag can cause either a co-field or anti-field rotation direction depending on the properties of the medium and particle and if the phase-lag is less or more than 180° . Dielectrophoresis in AC-fields is depended on the factor known as the Clausius Mossotti factor that "*arises when dealing with the polarization of a particle embedded in a medium whose dielectric properties differ from that of the particle*" (Pethig, 2017). Hence, where dielectrophoresis is dependent on the real part of the complex Clausius Mossotti factor, electrorotation is depended on the imaginary part and the torque respectively. A particle may experience both dielectrophoresis and electrorotation simultaneously. The directions and magnitudes are both related to the interaction between the dielectric properties of medium and particle where the relative magnitudes of force and torque are proportional respectively to the real and imaginary parts of the Clausius

Mossotti factor(Goddard et al., n.d.)

Basic Theory

2.1 Electrorotation

2.1.1 Introduction

Electrorotation as a phenomena is explained by Grimnes et al. (2002) and states that a particle suspended in a liquid exposed to a rotating electric field may experience torque. The particle will obtain an induced dipole moment. Electrorotation is performed on single cell. The polarization process is not immediate so the induced dipole will lag after the external rotating electric field. A frequency-dependent torque will thereby exist. This torque is the force that causes the particle either to rotate with the direction of the external field or counter-field wise.

From (Gimsa, 2001) it is mentioned that besides impedance measurements there are various methods of approach for dielectric characterization of single objects based on different force effects. The same principal can be used for manipulation, separation and trapping of different particles and objects. These methods are currently being developed and Gimsa states that one of the reasons that these methods, regardless of their high potencies, has not found a larger view of acceptance might be linked to the complexity of all present theory. In addition Gimsa mentions that an impression has been gained by the communities working on various dielectric methods not fully recognizes the strong interrelations between the diverse methods for dielectric characterization mentioned above. An experimental result obtained by uses of one method on an object, e.g. electro-optics are commonly not perceived by other researcher working on the same object by, e.g. electrorotation. Nevertheless, numerous approaches that leads toward a unified theory exists (Gimsa, 2001). Some of the strongly interrelated methods mentioned here

are electro-orientation (EO), electrodeformation (ED), dielectrophoresis (DP) and electrorotation (ER) and all methods are frequency dependent. Gimsa further states that Maxwell's stress tensor is the start for calculations of the frequency dependencies of the force effect affecting spherical objects of general ellipsoidal shape. The objects are either homogeneous or covered by a thin low conductive layer and fitted as single-shell models. A simpler approach is by the Laplace equation and as a curiosity Gimsa mentions that the general Laplace solution given for a single-shell ellipsoid experiencing polarization viewed as the standard model for a biological cell (Paul and Otwinowski, 1991; Sokirko, 1992) has already been derived from meteorological research on challenges surrounding dust particles covered by a layer of water (Bohren and Huffman, 1983).

Gimsa further states (Gimsa, 2001) for an explicit solution using Laplace equation the shape of an ellipsoid with a confocal shell must be assumed. This is explained due to the reason that confocal shells surfaces of an ellipsoid can be described within a single coordinate system. By the Laplace model, a homogeneous ellipsoid or a ellipsoid with a shelled homogeneous core always exhibits a constant field. Notions by Maxwell for a shelled sphere for any given frequency there can be found a homogeneous equivalent sphere. The equivalent sphere will exhibit a constant local field and an external dipole field as the shelled model. Hence, the equivalent sphere will experience the same forces as the shelled model.

The model presented by Gimsa (2001) extends the equivalent sphere notion to that of a single-shell ellipsoid by following the arguments of Maxwell. From the Laplace solution for homogeneous ellipsoid in a homogeneous field and here the structural properties of a biological cell can be taken into account accordingly to its low conductive membrane shell. For the constant local field inhibited within the homogeneous ellipsoid (or equivalent) three field components along the three principal axes of the ellipsoid must be considered. It is by the principal axes of the ellipsoid these field components can be calculated respectively as well as the induced potentials at the poles of the ellipsoid's surface.

From (Gimsa, 2001) these potentials were obtained by implementing a finite element ansatz(shape) function. Gimsa states further that the length of the external medium elements is defined by the influential radius of the object. *"For a given shape, the influential radii are parameters which are related to the characteristic distances up to which the dipole field may effectively project*

into the suspension medium. They are directly related to the electrostatic depolarizing factors (see ??)" (Gimsa, 2001). By then integrating over the field of the homogeneous (or equivalent) ellipsoid will unveil the objects dipole moment leading consequently to the expressions for electro-orientation (EO), electrodeformation (ED), dielectrophoresis (DP) and electrorotation (ER). Gimsa outlines when only the frequency dependencies are of interest it is enough to consider the Clausius Mossotti factor (CMF). The CMF is the frequency dependent part of the induced dipole moment. The CMF is key to the explanation of electrorotation. From (Gimsa, 2001) "In ER, a circularly polarized rotating field induces a circulating dipole moment. Any dispersion process causes a spatial phase shift of the external field vector and the induced dipole moment. The torque on the object is resulting from the interaction of the out-of-phase part of the induced dipole moment and the external field. Consequently, the torque is proportional to the imaginary part of the CMF. It describes the frequency dependence of the individual object rotation in or against the sense of field rotation."

Gimsa outlines that no isolated effects is common when observing either of these effects. Gimsa explains that ER was first discovered in EO and DP studies or EO and ED were observed in combinations of DP and ER. By Gimsa's studies that will be used in this thesis for the theoretical fundament of electrorotation it is stated that for simplistic reasons only electrical effects are considered. Hydrodynamic friction or thermally induced motions is not taken into account (Gimsa, 2001).

2.1.2 Theory: general part

The following theory in this subsection is elaborated more widely in an article published in the publication Bioelectrochemistry (Gimsa, 2001). In the article expressions is given for EO, ED, DP and ER for the forces and torques arising from the induced dipole moment. In this thesis only electrorotation will be method of focus, hence the only method derived but dielectrophoresis will be mentioned due to the strong correlation the two methods share.

Theory presented is in the rest of this subsection is found in (Gimsa, 2001): Following expressions for ellipsoidal objects in homogeneous, homogeneous and rotating AC fields. For the dipole approximations the object/particle size is presumed to be small in comparison to the variations of the characteristic field strength distances. In a field like this a time averaged force

$\langle F \rangle$ working on a homogeneous particle of general ellipsoidal form can be expressed followingly by the real part of the dot product of the induced dipole moment m and the gradient of the complex conjugate of the external electric field E^* :

$$\langle F \rangle = \frac{1}{2} \Re \left[m \nabla E^* \right] \quad (2.1.1)$$

The time average torque $\langle N \rangle$ given for polarised circularly electrical fields is found by the cross product of the induced dipole moment and the conjugate electric field given by:

$$\langle N \rangle = \frac{1}{2} \Re \left[m_x E^* \right] \quad (2.1.2)$$

The external AC field E in component notation can be written as following expression where E_0 is the field amplitude and ω , j and t is respectively circular frequency, the imaginary unit number $\sqrt{-1}$ and time:

$$E = \begin{pmatrix} E_x \\ E_y \\ E_z \end{pmatrix} = E_0 e^{j\omega t} \begin{pmatrix} e_x \\ e_y \\ e_z \end{pmatrix} \quad (2.1.3)$$

The components of the field vectors E_x, E_y, E_z are parallel to the the vectors i, j, k , respectively, and belong to the orthonormal base system. Different values of the e -components give different field properties (it should be noted that the selection of e -components also determines different overall values for the field amplitude). The induced dipole moment m is proportional to the external field E , the external permittivity $\epsilon_0 \epsilon_e$ and the V for volume of the ellipsoid. If the vectors of the base system is aligned parallelly to the principal axes of the ellipsoid m is written in component notation as:

$$\begin{aligned}
m &= (m_x \ m_y \ m_z) = \epsilon_0 \epsilon_e V C M F E \\
m &= \epsilon_0 \epsilon_e V \left(C M F_x^{\Re} + j C M F_x^{\Im} C M F_y^{\Re} \right. \\
&\quad \left. + j C M F_y^{\Im} C M F_z^{\Re} + C M F_z^{\Im} \right)
\end{aligned} \tag{2.1.4}$$

The frequency depended part of each component along the three principal axes of the ellipsoid is described with three CMF components. These components are indexed x, y, z . The CMF components a real part and an imaginary part. The real part is in phase with the inducing external field component (eq. 2.2.3) and are indexed \Re . The imaginary part is out of phase of the external field component and indexed \Im . The CMF component for a homogeneous ellipsoidal particle is given in x -direction as:

$$CMF_x = \frac{\epsilon_i - \epsilon_e}{\epsilon_e + (\epsilon_i - \epsilon_e)n_x} \tag{2.1.5}$$

where ϵ_i is the complex permittivity of the particle, ϵ_e is the complex permittivity of the external medium and n_x is the depolarization factor in x -direction (see Appendix A). Gimsa makes a notation of that the numerical values of the CMF from eq.(2.1.5) are three times larger than those factors mostly used in the literature. This is due to that the factor "3" appears in the volume and the depolarizing factors of a spheroid are not cancelled out.

Implementing equations (2.1.3) and (2.1.4) into equation (2.1.2) and solving for determinant obtained from the cross product gives:

$$\langle N \rangle = \frac{1}{2} \Re \begin{pmatrix} m_y E_z^* - m_z E_y^* \\ m_z E_x^* - m_x E_z^* \\ m_x E_y^* - m_y E_x^* \end{pmatrix} \tag{2.1.6}$$

All of the products of the elements of the vectors in Eq. (2.1.6) is coming from orthogonal

vectors, hence it is enough to only consider their absolute values.

2.1.2.1 General theory of electrorotation (ER)

In consideration of ER Gimsa (2001) explains that an electric circulating field that has a constant amplitude rotating in the x-y plane has to be assumed. This field can be described as, e.g. $e_x = 1$, $e_y = j$ and $e_z = 0$. The electric circulating fields components is followingly given as:

$$E_y = jE_x \quad E_y^* = -jE_x^* \quad (2.1.7)$$

Gimsa then explains that for practicality only fitting cases are taken into consideration. These cases are where the ellipsoid is oriented by the electrical external field. When the field is a circularly rotating field this implies that one of the principal axes of the ellipsoid always will be oriented perpendicular to the plane of the spinning field. The value of the z -component of the external field is zero, as will it be for the oriented ellipsoid and followingly the z -component of the induced dipole moment of the ellipsoid will also be zero and vanish. Gimsa further explains that the ellipsoid will rotate at a lot lower pace than the external circular field and the ellipsoidal object/particle will experience the same field amplitudes along the axes a and b . Relative to the x - and y -directions, respectively, the actual orientation of the axes these amplitudes are considered independent. With such a field Eq.(2.1.6) becomes:

$$\begin{aligned} \langle N_\kappa \rangle = & \frac{1}{2} \epsilon_0 \epsilon_e V \Re \left[(CMF_x^{\Re} + jCMF_x^{\Im}) E_x E_y^* \right. \\ & \left. - (CMF_y^{\Re} + jCMF_y^{\Im}) E_y E_x^* \right] \kappa \end{aligned} \quad (2.1.8)$$

further this can be simplified to:

$$\langle N_\kappa \rangle = \epsilon_0 \epsilon_e V E_0^2 \frac{CMF_x^{\Im} + CMF_y^{\Im}}{2} \kappa \quad (2.1.9)$$

Equation (2.1.9) shows that it is only the out-of-phase (imaginary CMF^{\Im}) parts of the induced dipole moment that affect the the magnitude of the torque. Furthermore Gimsa points out

that three different ER spectra will be obtained since a general ellipsoid can have three possible orientations and from that you can get three different combinations of the CMF . Gimsa adds *"at certain field frequencies, reorientation of the particles will be observed which results in an abrupt jump from one ER spectrum to another"* (Gimsa, 2001).

2.1.2.2 Brief introduction to dielectrophoresis (DP) and electrodeformation (ED)

Dielectrophoresis is described in (Kirby, 2010) as a mechanism to manipulate particles in microsystems. The particle response can change due to the frequency and the phase of the applied electric external field. The variation of the particle response can easily be operated by the user of the microsystem by changing the settings on the function generator driving the field and because of this DP has been used for many applications from sorting and capturing cells to separation of distinct particles as some examples. The term dielectrophoresis refers to ” *the Coulomb response of an electrically polarized object in a nonuniform electric field. In contrast to linear electrophoresis, it (a) does not require that the object have a net charge and (b) has a nonzero time-averaged effect even if AC electric fields are used*” (Kirby, 2010). Kirby mentions as an example a spherical, uncharged, uniform ideal dielectric particle with finite polarizability that is expressed by its electrical permittivity ϵ_p is placed in empty space. An uniform electric field is applied to the system and the sphere will be polarized. Then a net positive charge will be present at one end of the sphere and a net negative charge will be present on the other end of the sphere. Given that the electric field is classified as uniform and the sphere has the characteristics as mentioned above the Coulomb forces on either end of the sphere will be equal and opposite resulting in that the net Coulomb force is zero. However, if the field is non-uniform the side of the sphere with the larger electric field will experience a larger attractive force and the net total force will move the sphere toward the area of high electric field and movement towards high electric field areas is noted as positive dielectrophoresis.

Further from (Kirby, 2010) it is explained that in most microfluidic systems usually particles will be suspended in a medium (most commonly aqueous solutions) denoted with electric permittivity ϵ_m . If the medium is presumed to be a perfect dielectric as well as the sphere described above is immersed in the medium all arguments are similar except now both medium and particle polarize. For a particle submerged in a medium the net force working on the particle is dependent on the difference between the polarization of medium and particle. If the medium polarizes less than the the particle, the particle will experience positive DP forces and will move towards regions of higher electric field. The opposite case will be that the medium polarizes more than that of the particle and the particle will move towards regions of low electric field there by experience negative DP. For both cases is the orientation of the direction the

particle will move along a function of the electric field magnitude and not the polarity. Given this argument the dielectrophoretic response of an uncharged, uniform, ideal dielectric particle suspended in a ideal dielectric medium will be independent of whether a DC or AC field is applied. It is also independent of the frequency of the field as long the permittivity is independent of the frequency.

By (Kirby, 2010) it is explained that the preceding description is a way to highlight the basics physics of DP. Controlling the polarization of a particle and the medium it is suspended in, leads to a charge is generated at the interface between the particle and medium. This charge leads further to a net force generated if the applied field is non-uniform and the particle motion is dictated by the sign and magnitude of the charge generated at the interface. This interface charge is known as the Maxwell-Wagner interfacial charge (Kirby, 2010).

In most real cases especially looking at a biological cell as one example ideal dielectrics is not that common. From (Kirby, 2010) it is noted that if we still consider a particle or sphere that is uniform, uncharged but extend the analysis to include media and particles with finite conductivity and permittivity, quantifying the DP response is different. A extensive derivation is shown in (Kirby, 2010, p. 373-379) for following expression for a time-averaged DP response, spherical, uniform, isotropic, uncharged particle in an AC field:

$$\langle \vec{F}_{DP} \rangle = \pi \epsilon_m a^3 \text{Re}(CMF) \nabla (\vec{E}_0 \cdot \vec{E}_0) \quad (2.1.10)$$

where the angle brackets denote time averaging, $\text{Re}(CMF)$ is the the portion of the effective dipole moment in phase with the applied field and E_0 is the peak magnitude of the applied field. All the different components of Eq.(2.1.32) illustrates the role of different physical phenomena. The real part of the Clausius Mossotti factor $\text{Re}(CMF)$, ranges from 1 for $(|\epsilon_p^*| \gg |\epsilon_m^*|)$ to $-\frac{1}{2}$ for $(|\epsilon_m^*| \gg |\epsilon_p^*|)$ where subscript p , m and $*$ stands for particle, medium and complex denotation, respectively, and captures the phase relation between the effective dipole and the applied electric field. It is the sign of $\text{Re}(CMF)$ that determines whether the particle is attracted towards or are repelled from, regions of high electric field magnitude. In (Kirby, 2010) the CMF is given as:

$$CMF^* = \frac{\epsilon_p - \epsilon_m}{\epsilon_p + 2\epsilon_m} \quad (2.1.11)$$

In the high-frequency limit the ϵ^* can be replaced by ϵ in Eq.(2.1.33) and the DP effects

are/become strictly due to the polarization of the medium and particle as expressed by their permittivities. In the low-frequency limit ϵ^* can be replaced by σ in Eq.(2.1.33) and DP effects are/become strictly a function of the conductivities of the particle and medium. Kirby further notes that since the force is proportional to a^3 , the force is proportional to the volume of the sphere. The denotation a is the radius of the sphere and there for DP effects *"is a second-order electrokinetic effect that scales with applied voltage squared, and if the separation between electrodes is changed at constant voltage, dielectrophoretic effects scale with electrode spacing to the 3 power"*(Kirby, 2010).

In (Gimsa, 2001) DP is also explained but then from a view of an ellipsoidal shaped particle rather than an uniform and isotropic particle/sphere as described above from (Kirby, 2010). From (Gimsa, 2001) it is explained that its assumed an external field in a x -direction and a freely suspended particle of ellipsoidal shape has a parallel orientation of a certain principal axis (denoted as axis a that has a CMF index x), Its noted that thermal motion for a given field frequency is neglected so that it may be assumed that one of the principal axes of the ellipsoidal particle will always be oriented in parallel to the field. If Eq.(2.1.4) is introduced into Eq.(2.1.1) an expression for the time averaged DP force can be derived:

$$\langle F_i \rangle = \frac{1}{2} \epsilon_0 \epsilon_e V \Re[(CMF_x^{\Re} + jCMF_x^{\Im}) E_x \nabla E_x^*] i \quad (2.1.12)$$

Further, Gimsa describes if an assumed field is weakly inhomogeneous in x -direction can be approximated by Eq.(2.1.3) where $e_x = 1 + \gamma x$ and the other components are neglected ($e_y = e_z = 0$). The denotation γ is a parameter that describes the small field gradient (causing the inhomogeneity in the field, x -direction in this case) and Eq.(2.1.12) can be reduced to:

$$\langle F_i \rangle = \epsilon_0 \epsilon_e V CMF_x^{\Re} E_0^2 \frac{\gamma}{2} i \quad (2.1.13)$$

Eq.(2.1.13) from (Gimsa, 2001) shows that it is the real part of the CMF , along the axis that is parallely oriented with the applied field that describes the DP forces frequency dependence

and $\langle F_i \rangle$ is denoted as the time average force that is vector based with vector axis i for x . A reorientation of the ellipsoidal particle would change the index of the CMF . It is also noted by Gimsa that from Eq.(2.1.14) it can be explained that the particle will reorient giving the particle a subsequent change of the effective particle properties. This again will lead to a discontinuity in the DP spectra for the particle. Given value $\mu = 0$, the external field will be homogeneous and as result the DP forces will vanish. Gimsa explains that the forces acting on the two hemi-ellipsoids are balanced and will have a resultant net force of zero. However, there will still be forces affecting the particle and these forces will be translated into a ED-force that will be induced leading to compression or elongation of the particle (Gimsa, 2001).

2.1.2.3 Electro-orientation (EO)

From (Gimsa, 2001) and Eq.(2.1.3) for $e_x = e_y = e_z = 1$ is describing a linearly polarized AC field that is usually applied in EO. A general ellipsoid with its three principal axes is assumed that is parallelly oriented with the three base vectors. The magnitude of the external field that the ellipsoid is experiencing along all the principal axes is equal. The torque around each axis will only be dependent on the ellipsoid's properties. Gimsa elaborates that for a case like this Eq.(2.1.6) can be simplified and rewritten as:

$$\langle N \rangle = \frac{1}{2} \epsilon_e \epsilon_0 V E_0^2 \begin{pmatrix} CMF_y^{\Re} - CMF_z^{\Re} \\ CMF_z^{\Re} - CMF_x^{\Re} \\ CMF_x^{\Re} - CMF_y^{\Re} \end{pmatrix} \quad (2.1.14)$$

Gimsa further explains that for a given frequency and external conductivity the expression Eq.(2.1.14) can be used to isolate the two largest torque components that is induced around two of the three principal axes and consequently this will lead to an orientation of the particle that will occur along the the third axis of the weakest torque force. Permutation of the axes orientation within the coordinate system would not change the result as Gimsa describes that these relations has been considered by complicated tables of the signs of the components of Eq.(2.1.14) (for reference to these tables see (Gimsa, 2001, p.25, EO)). The model used is of the basis an ellipsoid that consists of a lossy dielectric core and an insulating shell (Gimsa,

2001).

2.1.2.4 Shelled particle models and polarizability

Describing a model for a shelled spherical particle is well documented. There are many different derivations of it. Most commonly used is a model describing a a single shell spherical structure or a dual-shelled structure. The dual-shelled model is often used were this reflects often enough a basic biological cell. However, from (Qian et al., 2014) it is highlighted that most bioparticles are complex, heterogeneous structures that contains a cell membrane, cytoplasm and a nucleus.

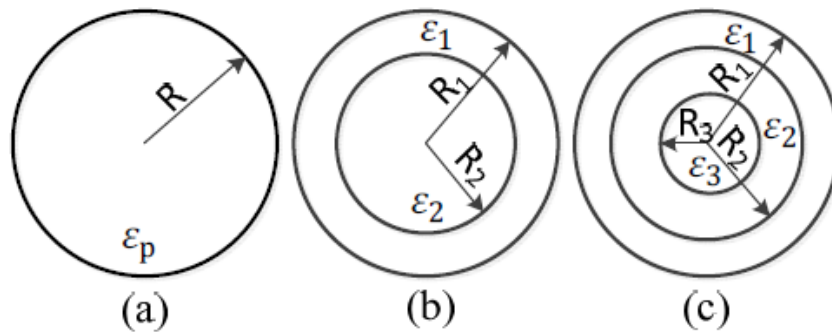


Figure 2.1: (a) Single-shell; (b) Dual-shell; (c) Multi-shell
Image source: (Qian et al., 2014)

Quian has showed that each of these models have different electrical properties and the single-shell model from figure (2.1 - a) would not correctly describe a biological cell as mentioned above, but rather the models from figure (2.1 - b or c) would be more suitable. The dual-shell model in figure (2.1 - b) R_1 and R_2 are the radius of the sphere outermost layer and innerlayer, respectively. ϵ_1 and ϵ_2 are the permittivity of each layer where the subscript corresponds to the R_1 and R_2 respectively. When AC electric fields are applied, the complex permittivity must be used. An equivalent permittivity for model (b) from figure (2.1 - b) is given by:

$$\epsilon_p = \epsilon_1 \frac{\left(\frac{R_1}{R_2}\right)^2 + 2\left(\frac{\epsilon_2 - \epsilon_1}{\epsilon_2 + 2\epsilon_1}\right)}{\left(\frac{R_1}{R_2}\right)^2 - 2\left(\frac{\epsilon_2 - \epsilon_1}{\epsilon_2 + 2\epsilon_1}\right)} \quad (2.1.15)$$

(Qian et al., 2014) mentions that a spherical model is quite common and simple, but most bioparticles are not of spherical shapes but closer to an ellipsoidal structure and clearly makes

the calculations more complex.

In (Jones, 1984) it is given an derivation for the effective dipole moment for a non-spherical particle. A spheroid shape imparts a geometric anisotropy to the particle which results in that the induced dipole moment is parallel to the imposed electric field only if the particle is oriented in alignment with one of the particles principal axes which is parallel to the field. Many bioparticles are often shaped relatively close to a form of an oblate spheroid which is fairly close to that of an ideal spheroid with three semi-major axes in the approximate ratio of 4:2:1.

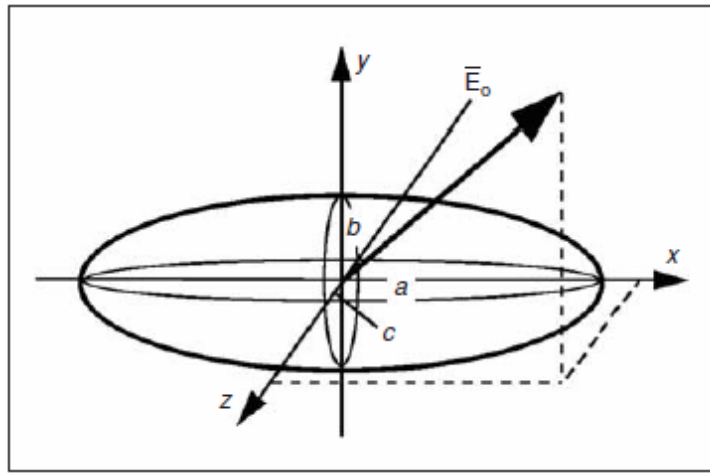


Figure 2.2: A spheroidal dielectric particle situated in a uniform electric field. a , b and c are the semi-major axes. The particle will experience an electrical torque that will try to align the particle with either of the axes, but only alignment along the longest axis is stable. In this case that would be axis (a). Image source: (Jones, 1984)

Described by Jones, the effective induced dipole moment of a homogeneous spheroid with three semi-major axes a , b and c as viewed in Fig.(2.2) may be expressed by:

$$\bar{P}_{eff} = \frac{4\pi abc}{3} (\epsilon_2 - \epsilon_1) \bar{E}^* \quad (2.1.16)$$

Subscripts 1 and 2 denote medium and particle, respectively and \bar{E}^* is the uniform internal electric field to the particle which is in general not parallel to the external field \bar{E}_0 . Where L is the depolarizing factor, the internal field \bar{E}^* is described as (Jones, 1984):

$$E_x^* = \frac{E_{0,x}}{\left[1 + \frac{(\epsilon_2 - \epsilon_1)L_x}{\epsilon_1}\right]} \quad (2.1.17)$$

For a derivation of the depolarizing factor for Eq.(2.1.16) and Eq.(2.1.17) see (Jones, 1984).

Another model is explained in (Gimsa et al., 2014) and is linked closer to an particle of ellipsoidal shape described by polarization of a single-shell model using Maxwell's equivalent body.

The article (Gimsa et al., 2014) is the source for all the material further presented in the next paragraphs until other citations are presented. AC-electrokinetics as ER and DP covers a large frequency range that spans over many decades ($< 1kHz$ to $> 1GHz$) making AC-electrokinetics a flexible choice of polarization effects that generate forces to manipulate objects. Generally, the forces generated will increase with the relative changes between the object and the suspending medium. For AC-electrokinetics different methods exist to increase this contrast differences, e.g by changing optimal field frequency or the conductivity of the medium. AC-electrokinetic effects occurs from the interaction of the induced polarization of the objects with the inducing external field. AC-electrokinetics characterization requires high field strength ($> 1000 \frac{V}{m}$) and a (microscopic) way to observe the induced movement. As of this an advantage is gained in form of a higher parameter resolution and the discrimination against electrode effects. *"AC-electrokinetic methods are differential, i.e. impedance determines the integral polarizability of suspension medium and the objects, while AC-electrokinetics is based on the difference in the effective polarizabilities of medium and object. Nevertheless, in both approaches, analytic descriptions are based on the same geometrical models, e.g. multi-shell ellipsoidal cell models"*.

Gimsa et al. notes that electric force effects on suspended objects in media may also be induced by the interaction of DC or AC fields with electric double layer for DC electrokinetics or dipole charges as Debye effects. If an external AC field is applied, a distortion of the equilibrium the distribution of such charges, objects or media are polarized. This polarization frequency dependent in α -, β -, γ and δ -frequency dispersion's (see Gimsa and Wachner (1998)). However, the article (Gimsa et al., 2014) focuses on AC field-induced polarizations at the structural interfaces in inhomogeneous media (Maxwell-Wagner polarization i.e. β dispersion). Further from (Gimsa et al., 2014) it is explained that the AC fields induce polarization charges at the structural interfaces inside inhomogeneous media which is known as Maxwell-Wagner

polarization. Suspensions or emulsions of micro- and nano-scale objects like particles, air bubbles or biological cells are introduced by medium boundaries. An example of such a boundary can be biological membranes.

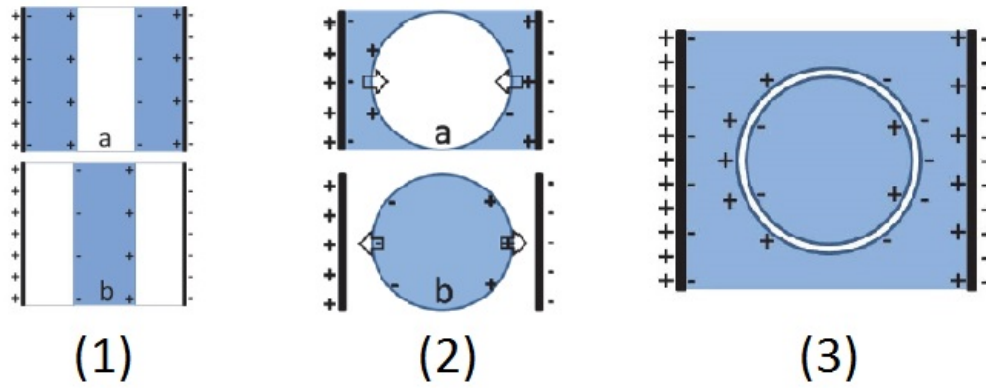


Figure 2.3: In all models (1, 2, 3) the induced charges is drawn for either DC or AC for the half-wave during which the right electrode is negatively charged.

(1) Represents two complementary models that consists of blocks of air and water. The external electrode charges influence charges in water but not air. (a) one air block confined by two water blocks (b) two air blocks confining one water block.

(2) Complementary polarization and force effects in air-water models. The induced charges are situated in the medium (water) with the higher polarizability. The interaction of these induced charges with the electrode charges, i.e. the external field, leads to compression of the air bubble (a) and elongation of the water droplet (b).

(3) Single-shell cell model obtained by combining the water droplet (2b) and a slightly larger air bubble from (2a) creating a thin air film (i.e. a "biological membrane") surrounding the water droplet's surface. It is assumed that the external medium has a lower conductivity than the internal medium and both mediums are considered isotonic.

Image and caption source : (Gimsa et al., 2014)

AC-electrokinetic effects are based on the forces that is generated as a result by the interaction of these polarization charges with the inducing field. The general dielectric structure of biological cells introduced by two media of complementary electrical properties. Biological membranes have relative permittivities below 10 and specific conductivities in the range of $10^{-6} \frac{S}{m}$. Aqueous solution (cytoplasm, nucleoplasm and interstitial solution) have values of relative permittivity of 70 and conductivities in the range of $1 \frac{S}{m}$. Gimsa et al. explain that from a physical point of view the lipid and aqueous phases can qualitatively be represented by air (or vacuum) and water, respectively to the lipid and aqueous phase (see figure 2.3). The simple block model in figure (2.3- 1) consists of air and water blocks isolated by electrodes. The charges on the electrodes will influence charges in the water but not in air. The interfacial

charges are carried by ions (conductivity differences) and dipoles (permittivity differences). In figure (2.3- 2) a geometrical transition into spherical objects of a water droplet and air bubble immersed in air or water respectively, will not change the charge distribution qualitatively. Figure (2.3-2) illustrates two complementary situations of effective polarization of spherical objects that are less or more polarizable than the surrounding medium. Figure (2.3- 3) represent a single-shell model of a biological cell. With low external conductivity, biological cells may qualitatively behave like air bubbles (below membrane dispersion) or as water droplets (above membrane dispersion) dependent on the frequency of the applied external field. The cytoplasm is almost field-free at low frequencies and the membrane experience extremely high field around its poles which will be oriented in the field direction (Gimsa et al., 2014).

Gimsa et al. further elaborates that in general AC-electrokinetic effects are modelled by using the induced dipole moment of the object/particle. The dipole moment is proportional to the difference of the integrals over the effective local fields in inner volume of the particle/object and that of the undisturbed external field in the same volume when the object/particle is absent. The second integral is frequency-independent for constant external field strength. The model of the biological cell illustrated in figure (2.3-3) illustrates that the volume integral is dominated by the membrane field at low frequencies. When high field frequency is applied the membrane is capacitively bridged and the membrane-field contributions will decrease and the volume integral becomes dominated by the cytoplasmic field. The orientations of the dipole moments are antiparallel in the two cases (Gimsa et al., 2014).

In (Gimsa et al., 2014) it is described a method that implements a influential-radius concept that allows for the separation of the geometric and electric problem. The influential-radius concept also allows for a simple description of the induced dipole moment in addition to the transmembrane potential (see Gimsa and Wachner (2001)). In (Gimsa et al., 2014) it is explained that due to physical principles, potential differences generate forces, e.g. the difference between the potential at the site of the pole in the presence and the absence of the object/particle (see figure 2.4). Gimsa et al. makes a notation concerning that the effective field in confocally shelled objects/particles that is polarized in a homogeneous external field is constant and corresponds to Maxwell's equivalent body.

The influential radius mentioned above describes the dependence of the maximum pole

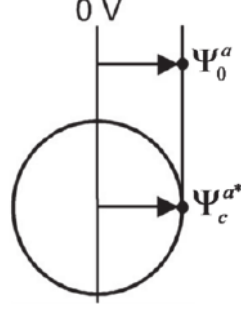


Figure 2.4: The external field (horizontal oriented component) E_a induces potentials $\Psi_0^a = aE_a$ and Ψ_c^{a*} . Subscripts 0 and c denotes in absence and presence, respectively, of an ellipsoidal object at the site of the pole. Its semi-axis is denoted a . Ψ_c^{a*} is at its highest for a vacuum object with a polarizability similar to that of a membrane covered cell at low frequency. As an example a vacuum sphere attracts the equipotential plane that is located at the "influential radius" a_{inf} distance of $\frac{3a}{2}$ from the symmetry plane which can be set to being 0 V. The maximum of $\Psi_c^{a*} = a_{inf}E_a$ is determined by the influential radius i.e. which is the geometry of the object. The actual value is determined by the effective electric properties of the object and the suspending medium.

Image and caption source : (Gimsa et al., 2014)

potential to the shape of an ellipsoidal object. In general the induced complex dipole moment along semi-axis a for a object of the volume $V = \frac{4\pi abc}{3}$ is:

$$m_a^* = \epsilon_e \epsilon_0 V C M F_a^* E_a \quad (2.1.18)$$

where $\epsilon_e \epsilon_0$, $(C M F_a^* = C M F_a^{\Re} + C M F_a^{\Im})$ and E_a denotes the permittivity of the external medium, the complex Clausius-Mossotti factor consisting of a real and imaginary part and the external field component along semi-axis a . Complex terms is denoted by asterisks (*). $C M F_a^*$ is derived by the normalization of the potential difference at the site of pole a in absence or presence of the ellipsoidal object (See figure 2.4):

$$C M F_a^* = \frac{1}{n_a} \left(\frac{\Psi_0^a - \Psi_c^{a*}}{\psi_0^a} \right) \quad (2.1.19)$$

where n_a being the depolarizing factor (see appendix A). Further from (Gimsa et al., 2014) its made a notation of that for objects of ellipsoidal shape $n_a + n_b + n_c = 1$ and for spherical objects $n_a = n_b = n_c = \frac{1}{3}$. "The distances from the object's respective symmetry planes to those equipotential planes that is just touching the respective poles of a vacuum object with the shape of the actual object are along each semi-axis of an ellipsoidal object" (Gimsa et al., 2014)

denoted as a_{inf} , b_{inf} , c_{inf} . Along the semi-axis a the influential radius is given as:

$$a_{inf} = \frac{1}{a - n_a} a \quad (2.1.20)$$

These three influential radii provide the solution for the geometric problem. Solving the electric problem for single shelled ellipsoid can be realized by assuming a series circuit of three resistor-capacitor (RC) pairs for the internal, membrane and external medium along each semi-axis (see figure 2.5). The length of the three external elements (e.g. Z_e^{a*} which is along semi-axis a) need to be of a size that is long enough to ensure the maximal possible potentials at the poles (Gimsa et al., 2014).

There are at least two augmentations for how correct the description is by three stacked "finite" elements (RC pairs) along the semi-axis cited from (Gimsa et al., 2014):

1. "For symmetry reasons, field lines must exist that are oriented along the semi axes. For a current along these field lines, the voltage drop relations are correctly described by chains of RC pairs with infinitely small but equal cross sections" (equation. 2.1.22).
2. "In analogy to Maxwell's equivalent-sphere notion, the fields in the ellipsoidal internal homogeneous bulk (cytoplasm) and in the equivalent body of the whole single shell object are constant. These fields (or more general: field components) are oriented in parallel to the inducing external field (or field components). Accordingly, the internal bulk and the membrane-field components at the poles are oriented along their respective semi-axis and the voltage drops over the membrane correspond to the induced transmembrane potentials, i.e. the differences of the potentials at the poles of the internal bulk object and the whole object."

The impedance Z^* of the the tree RC pairs in figure (2.5) along a semi-axis is possible to calculate. Derived from (Gimsa et al., 2014) the calculations are based on the geometries of prismatic elements described by their lengths l , i.e. semi-axis ($l = a$), membrane thickness

($l = d$), ($l = a_{inf} - a$) and constant cross-sectional area A :

$$z^* = \frac{1}{\sigma + j\omega\epsilon\epsilon_0} \left(\frac{l}{A} \right) \quad (2.1.21)$$

where $j = \sqrt{-1}$, $\omega = 2\pi f$. The denotations σ , ϵ , ϵ_0 and f stands for the specific conductivity, relative permittivity of the considered medium, the permittivity of free-space and the field frequency.

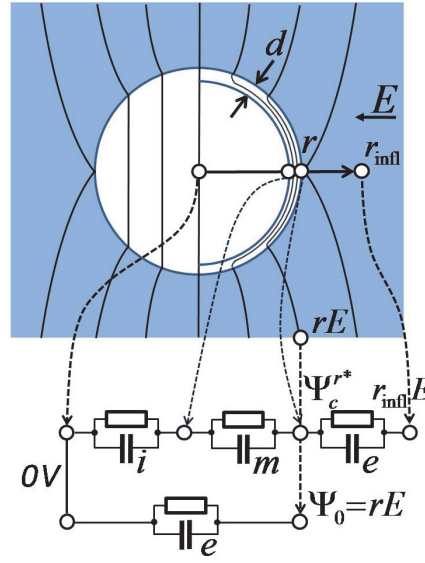


Figure 2.5: The illustration above shows equipotential plane distribution through and around a spherical single-shelled model of a radius r . Sketched on the left hemisphere is the external distribution that is identical to Maxwell's equivalent body and the membrane-covered object that is sketched at the right hemisphere. Important points are marked in the model as circles, the potential at these circular points can be obtained from the RC-model underneath the illustration. This will permit the calculations of the induced dipole moment and the transmembrane potential. "From the existence of Maxwell's equivalent body, it follows that electric measurements (detecting the induced dipole moment) do not allow one to distinguish whether frequency-dependent object properties stem from internal structures or from the frequency dependent properties of the media of which the object is composed of." (Gimsa et al., 2014)

Image and caption source : (Gimsa et al., 2014)

From the voltage-divider chains seen in figure (2.5), the potentials at the semi-axes poles can be obtained. Chosen semi-axis a the potential is obtained (Gimsa et al., 2014) :

$$\Psi_c^{a*} = \frac{Z_i^{a*} + Z_m^{a*}}{Z_i^{a*} + Z_m^{a*} + Z_e^{a*}} \left(\frac{a_{inf}}{a} \right) \Psi_0^a \quad (2.1.22)$$

2.1.2.5 Electrorotation spectrum's ROT, characteristic frequency and external conductivity correlation

In this section, the pivotal points of dielectrophoresis and electrorotation spectra are explained. The primary focus will be on electrorotation spectra. However, there are a complemented relations between the real and imaginary part of the induced dipole moment (DEP and ER, respectively) through the frequency range of the spectrum. The complemented connection between the in-phase and out-of-phase components of the induced dipole moment is explained as well as all pivotal characteristic and critical frequencies.

Interpretation of the spectrum and the transition between the different dispersions

The rate of rotation for electrorotation is plotted for the imaginary part of the CMF and real part of the CMF for dielectrophoresis. Electrorotation spectra can be plotted directly through visually observing the rotation rate for a single cell through a selected range of frequency that will represent the imaginary part of the CMF. Rotation rate spectra are commonly presented in the literature as plots normalized by the field magnitude squared where E_0 is the external field magnitude, and T is the time for one revolution, respectively :

$$\text{Rotation rate} = \frac{2\pi}{E_0^2 * T} \quad (2.1.23)$$

Figure. 2.9 from (Gimsa and Wachner, 1999) is a typical interrelated single-shell model that represents the real and the imaginary part of the CMF. However, this spectrum is plotted from calculated values and not a representation of visual observations. The calculations are based on a set of derived characteristic equations for on an RC-model representing a spherical cell-model with standard biological parameters (see section. 2.1.2.6). Figure. 2.9 is used here for illustrative purposes for how a typical electrorotation spectrum (ROT) is graphically presented and what it represents. The characteristic frequencies, plateaus and rotation peaks in the spectrum are denoted as f_* , F_* and R_* , respectively.

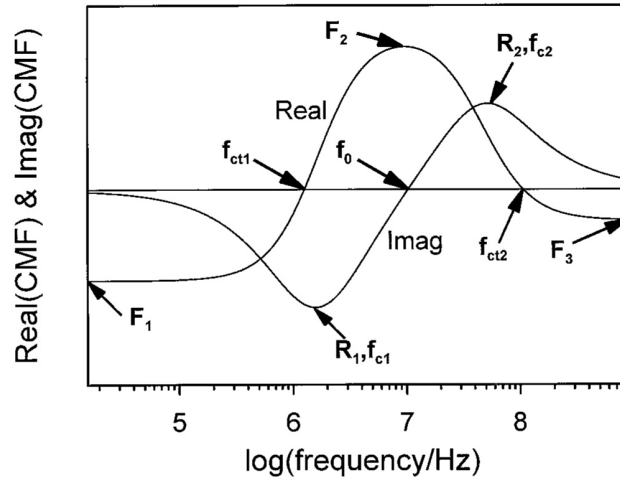


Figure 2.6: Typical electrorotation and dielectrophoresis spectrum. The imaginary part of the CMF is the plot with the two characteristic peaks R1 and R2 which represent electrorotation and the plot having two characteristic frequencies denoted as f_{ct1} and f_{ct2} represents the real part of the CMF and is the dielectrophoresis spectrum.

From (Gimsa, 2018) the spectrum's denotations and the unique dispersions represented in the figure is explained. The anti-field rotation peak (R1) is located at the half-value of the DEP dispersion from the negative to positive plateaus in namely F_1 to F_2 . At the rotation peak, R_1 the out-of-phase part of the induced dipole moment is 45° . It can be looked on as two different dispersion's related to R_1 and R_2 . The capacitive membrane dispersion mediates the transformation of the cell polarization, which is dominated by the non-conducting membrane below the dispersion to a polarization governed by the relations of the ionic conductivities of the inner and outer media (bulk media). The membrane dispersion can also be explained as the transition between the force plateaus F_1 and F_2 which results in the first anti-field rotation peak R_1 around the characteristic frequency f_{c1} . The second dispersion comes from the superseding of the bulk conductivity related to polarization by a bulk permittivity-related polarization. The second dispersion (bulk dispersion) mediates the transition between force plateaus F_2 to F_3 while giving rise to the second co-field rotation peak R_2 around the characteristic frequency f_{c2} . Gimsa further explains at low conductivity values given for the external medium and the membrane, the force plateaus F_1 and F_3 are usually negative and F_2 positive for biological cells and intact membranes. The DEP forces disappear at the characteristic critical frequencies f_{ct1} and f_{ct2} , i.e., the magnitude of the real part (in-phase) of the induced dipole moment is zero. Figure. 2.9 shows that the real part (in-phase) of the induced dipole moment is complemented by the transition in the imaginary part (out-of-phase) (Gimsa, 2018). The critical frequency denoted f_0

is the frequency between the two rotation peaks R_1 and R_2 where there are no induced torque on the particle meaning that the imaginary part of the CMF is zero (Gimsa and Wachner, 1999), i.e. the imaginary part of the induced dipole moment is zero (see equation 2.1.4 and 2.1.18).

The transitions from the membrane dispersion to the bulk dispersion and further up in the frequency range can be described for the cell through the definition of admittance (Y). The imaginary part of admittance is susceptance (B), and if susceptance is derived through capacitance (C) it can be expressed so that the permittivity (ϵ) becomes a more prominent factor the higher the frequency is. Equation. 2.1.24 shows how conductivity dominates the lower frequency range of the induced dipole moment. Further up in the frequency range through the membrane dispersion where the membrane of the object is bridged, the bulk conductivities becomes prominent to where the permittivity relations for the bulk conductivities becomes decisive for the polarization and the induced dipole moment. Admittance can be derived as shown in the equation. 2.1.24 where ϵ_0 , ϵ_r , j , ω , f , A , and d is the permittivity of free-space, relative permittivity, $\sqrt{-1}$, angular frequency, frequency, plate area and distance between the plates, respectively. The derivations for the equation. 2.1.24 is explained in (Grimnes and Martinsen, 2015):

$$Y = G + jB = G + j\omega C = G + j2\pi f\epsilon_0\epsilon_r \frac{A}{d} \quad (2.1.24)$$

Dielectrophoresis and electrorotation are both based on the interaction of the induced dipole moment and the external field strength. It was mentioned at the start of this section that it is common practice to normalize the electrorotation and dielectrophoresis spectra with the square of the field strength. Both effects of DEP and ER are both proportional to the square of the same field strength (see equation. 2.1.13 and 2.1.9). For better comparability of the experiments yielding the DEP and ROT spectra, the data is normalized to the square the external field strength (Gimsa, 2018).

Electrorotation spectra and correlation to the conductivity of the media

The conductivity of the medium is a decisive factor as the one parameter that can be controlled or adjusted for an emulsion of particles. In (Hölzel and Lamprecht, 1992) and (Hölzel, 1997) electrorotation experiments on yeast cells (*Saccharomyces cerevisiae*) are presented. Both stud-

ies surround how the rotation spectra are affected by external medium conductivity. In (Hölzel and Lamprecht, 1992) it is explained that when examining a two-shell model fitting a yeast cell (cell wall and cell membrane) certain critical and characteristic frequencies changed due to a change in the external medium conductivity. Hölzel found that with increasing conductivity of the external medium from $20 \mu\text{S/cm}$ to $2200 \mu\text{S/cm}$ the zero crossing (f_0) was shifted to higher frequencies. The spectra presented in the figure. 2.7 from (Hölzel and Lamprecht, 1992) gives an indications that the first rotation peak (R1) also was shifted to higher to frequencies with increasing external medium conductivity. However, it is noted that the second rotation peak remained unaffected up to $300 \mu\text{S/cm}$. The spectrum gives no data for frequencies below 3 MHz, but for conductivity levels above $200 \mu\text{S/cm}$, it is indicated the first rotation peak exists for conductivity values between $200 \mu\text{S/cm}$ and $500 \mu\text{S/cm}$. For conductivity levels above $500 \mu\text{S/cm}$, the first rotation peak is found between 5 and 10 MHz. The decisive factors for the first rotation peaks for different given characteristic frequencies are dependent on the relation between the conductivity of the medium and cell (see section. 2.1.2.5 and 2.1.2.6).

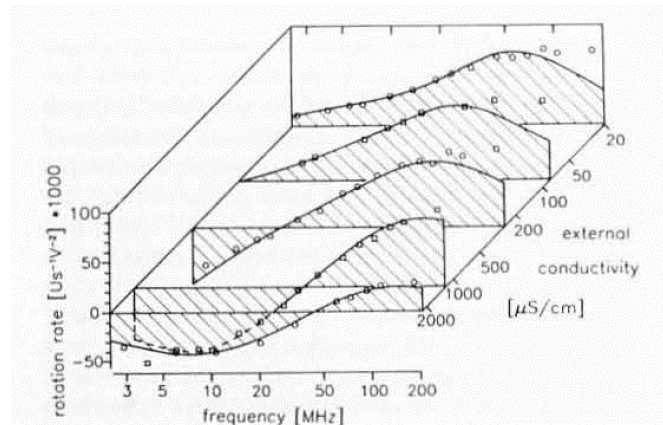


Figure 2.7: Electrorotation spectrum of *Saccharomyces cerevisiae* in different conductivity levels for the external medium. The spectrum is taken from (Hölzel and Lamprecht, 1992) and represents experimental data.

Similar electrorotation spectra is found in (Hölzel, 1997) shown in figure. 2.8. Here as in the figure. 2.7 electrorotation spectra of baker yeast (*Saccharomyces cerevisiae*) is shown for different levels of external medium conductivities are presented. Figure. 2.8 shows a correlation between the increase in the first characteristic frequency surrounding the first rotation peak (R1) to the increase in conductivity of the external medium. The second characteristic frequency surrounding the second rotation peak (R2) is also shifted to higher frequencies with the increasing conductivity levels of the external medium. Hölzel used a four-shell spherical cell model for the

least-squared fit of the spectra. In (Hölzel, 1997) makes a notation of that some spectra taken below 3 KHz showed a transition from anti-field rotation at $0.7 \mu\text{S}/\text{cm}$ to co-field rotation at $0.7 \mu\text{S}/\text{cm}$. In section.2.1.2.5 it is metioned through conductivity testes performed by ?

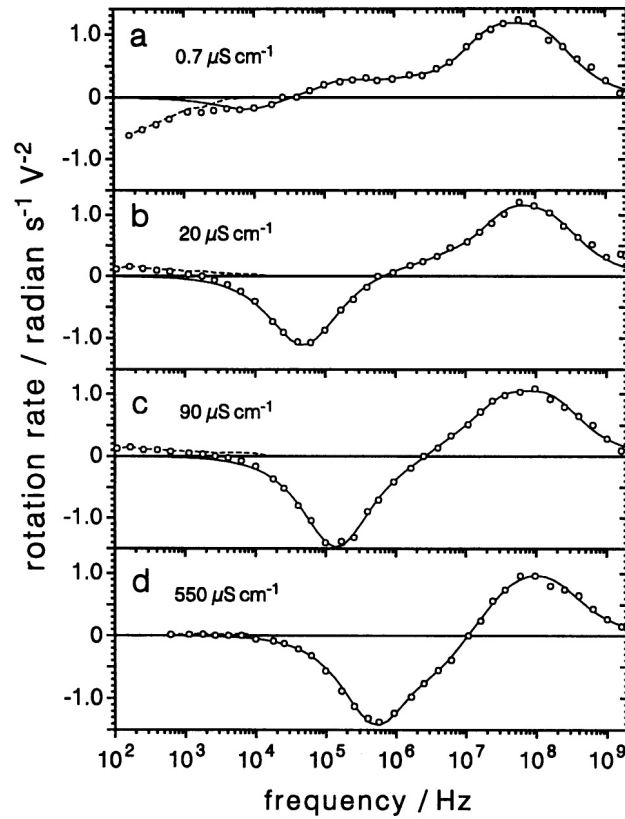


Figure 2.8: This figure illustrates an electrorotation spectrum of the yeast cell (*Saccharomyces Cerevisiae*) for four different values of conductivity in the external medium. The curves represent least-square fits to the data above 3 KHz according to a four-shell model. The dashed line below 20 KHz represents the difference between experiments and simulation.

2.1.2.6 Characteristic equations derived and explained by RC-models

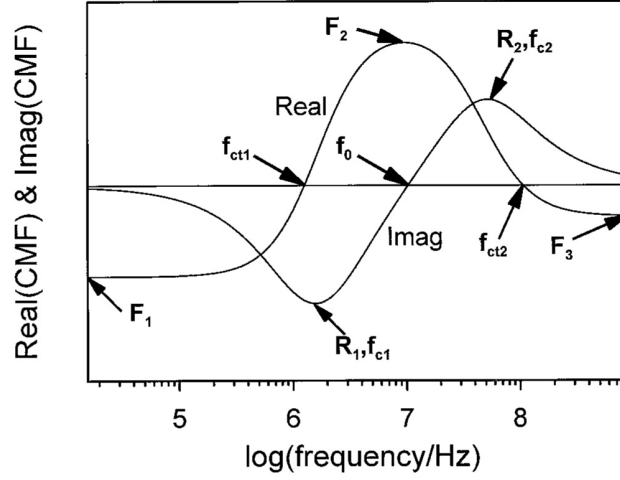


Figure 2.9: ” Schematic DP ($\text{Real}_{\text{CMF}^*}$) and ER ($\text{Imag}_{\text{CMF}^*}$) spectra. For DP, characteristic force plateaus (F_1 , F_2 , F_3) and critical frequencies (f_{ct1} , f_{ct2}), for ER torque peaks (R_1 , R_2), characteristic frequencies (f_{c1} , f_{c2}) and the characteristic frequency of no torque (f_0) are marked.”

In this section, a set of equations derived by Gimsa and Wachner published in (Gimsa and Wachner, 1999) is presented and explained. The equations are based on two different RC models fitting the two dispersions observed in an electrorotation spectrum, the membrane dispersion, and the bulk conductivity dispersion. The equations presented is the rotation rate (R_1 , R_2) for both electrorotation torque peaks and their coherent two characteristic frequencies (f_{c1} , f_{c2}) and the critical frequencies (f_0) where the plot of the imaginary part of the CMF crosses the x-axis. In (Gimsa and Wachner, 1999) there are also presented equations for the three DEP plateaus (F_1 , F_2 , and F_3) and the two critical frequencies (f_{ct1} , f_{ct2}) where the DEP forces is zero. To derive the characteristic equations the membrane properties were expressed by area-specific conductance ($g = \sigma_m/d$) and capacitance ($C = \epsilon_0\epsilon_m/d$) where σ_m , ϵ_0 , ϵ_m , and d are denotations for the membrane conductivity, permittivity of free-space, membrane permittivity and membrane thickness. The equatorial radius of the object is denoted r . ξ is a denotation for a factor derived from the influential radius (see equation. 2.1.20).

$$\frac{r_{infl}}{r} = \frac{1}{1-n} \quad \xi = \frac{r_{infl}}{r} - 1 \quad , \text{ where e.g. } \xi = 0.5 \text{ for spherical models} \quad (2.1.25)$$

Derived equations for DEP spectra and cell deformation

For DEP spectra and cell deformation the following characteristic equations are derived: (Gimsa and Wachner, 1999):

$$F_1 = (\xi + 1) \frac{r g(\sigma_i - \sigma_e) - \sigma_i \sigma_e}{r g(\xi \sigma_i + \sigma_e) + \sigma_i \sigma_e} \quad (2.1.26a)$$

$$F_2 = \frac{(\xi + 1)(\sigma_i - \sigma_e)}{\xi \sigma_i + \sigma_e} \quad (2.1.26b)$$

$$F_3 = \frac{(\xi + 1)(\epsilon_i - \epsilon_e)}{\xi \epsilon_i + \epsilon_e} \quad (2.1.26c)$$

$$f_{ct1} = \frac{1}{2\pi r C} \sqrt{\frac{\sigma_e^2 \sigma_i^2 - \sigma_e \sigma_i r g((1 - \xi)\sigma_i - 2\sigma_e)}{(\sigma_i - \sigma_e)(\sigma_e + \xi \sigma_i)}} - r^2 g^2 \quad (2.1.26d)$$

$$f_{ct2} = \frac{1}{2\pi \epsilon_0} \sqrt{\frac{(\sigma_i - \sigma_e)(\sigma_e + \xi \sigma_i)}{(\epsilon_e - \epsilon_i)(\epsilon_e + \xi \epsilon_i)}} \quad (2.1.26e)$$

Derived equations for ER spectra

The characteristic equations for ER spectra are derived(Gimsa and Wachner, 1999):

$$R_1 = \frac{-(\xi + 1)^2 \sigma_i^2 \sigma_e}{2(\sigma_e + \xi \sigma_i)(r g(\sigma_e + \xi \sigma_i) + \sigma_e \sigma_i)} \quad (2.1.27a)$$

$$R_2 = \frac{(\xi + 1)^2 (\sigma_i \epsilon_e - \epsilon_i \sigma_e)}{2(\sigma_e + \xi \sigma_i)(\epsilon_e + \xi \epsilon_i)} \quad (2.1.27b)$$

$$f_{c1} = \frac{1}{2\pi r C} \left(\frac{\sigma_e \sigma_i}{\sigma_e + \xi \sigma_i} + r g \right) \quad (2.1.27c)$$

$$f_{c2} = \frac{1}{2\pi \epsilon_0} \left(\frac{\sigma_e + \xi \sigma_i}{\epsilon_e + \xi \epsilon_i} \right) \quad (2.1.27d)$$

$$f_0 = \frac{1}{2\pi} \sqrt{\frac{\epsilon_0 r g^2 (\epsilon_e \sigma_i - \epsilon_i \sigma_e) + \sigma_i^2 (\epsilon_0 \epsilon_e g - C \sigma_e)}{\epsilon_0 r C^2 (\epsilon_e \sigma_i - \epsilon_i \sigma_e) + \epsilon_0^2 \epsilon_i^2 (\epsilon_0 \epsilon_e g - C \sigma_e)}} \quad (2.1.27e)$$

Simplified derived equations for ER spectra

In (Gimsa and Wachner, 1999) it is noted that for spherical models where $\xi = 0.5$ all equations except R_2 and f_0 can be simplified. The simplified characteristic equations for ER spectra is found in appendix A in (Gimsa et al., 1991). Simplified equation for DEP is also given in (Gimsa et al., 1991) but is not presented.

The simplified characteristic equations for ER spectra are:

$$R_1 = \frac{-1.5\sigma_i}{(2\sigma_e + \sigma_i)[gr(1/\sigma_e + 2/\sigma_i) + 2]} \quad (2.1.28a)$$

$$f_{c1} = \frac{1}{2\pi rC} \left(\frac{1}{1/2\sigma_e + 1/\sigma_i} + rg \right) \quad (2.1.28b)$$

$$f_{c2} = \frac{2\sigma_e + \sigma_i}{[2\pi\epsilon_0(2\epsilon_e + \epsilon_i)]} \quad (2.1.28c)$$

Argued in (Gimsa and Wachner, 1999) an RC approach allows for the easiest simplification for the derivation of the equations above. The equations describe the main parameter dependencies of characteristic points of cell deformation, e.g., DEP, ER, induced transmembrane potential. While the deformational and DEP forces are proportional to the real (in-phase) part of the CMF the ER torque forces is proportional to the imaginary part of the CMF. The CMF is related to changes $\Delta\Psi_c^*$ (see figure.2.1.11, equation.2.1.29a) and depends on the axis ratio and the influential radius(see equation. 2.1.30)

From (Gimsa and Wachner, 1999) it is explained that the CMF for a given axis ratio a spheroid may *"theoretically reach two extreme values which correspond to the two extreme cases for the relative polarizabilities of medium and object. Biological cells, insulated by their low conductive membrane of high specific capacitance may, depending on field frequency, approach these two cases when suspended in a low conductive medium."*(Gimsa and Wachner, 1999). The equations for the minimum and maximum of the CMF is given in figure.2.1.10. Gimsa explains they must correspond to the extrema of the local field and the potential Ψ_e^* ,

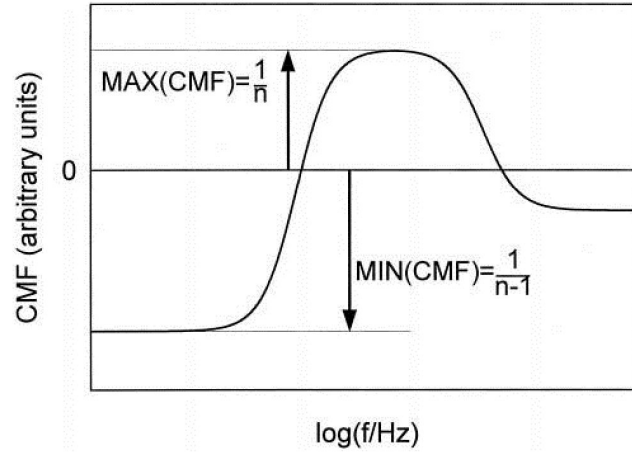
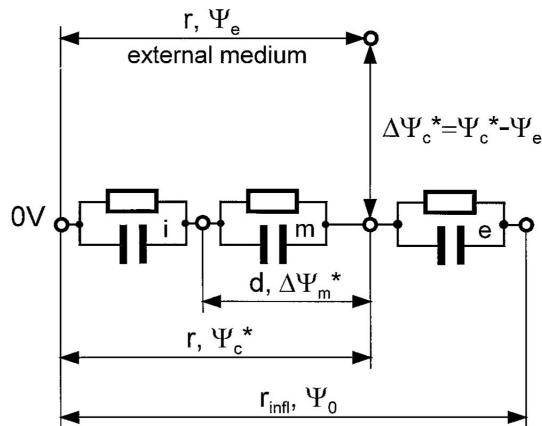


Figure 2.10: "Schematic drawing of the frequency dependence of the CMF of a cell-like object, with low and high relative polarizability at low and medium frequencies, respectively. At very high frequencies the polarizability is determined by the ratio of core and medium permittivities." (Gimsa and Wachner, 1999)

respectively. The local field according to Landau and Lifschitz (1985) the local field within a homogeneous ellipsoid can be expressed as in equation.2.1.29b. In the RC model in figure.2.1.11 the local field is given by Ψ_c^*/r . Its maximum corresponds to the minimum in CMF is Ψ_0/r . This further leads to the relations of r_{infl} and n expressed by equation.2.1.25 (Gimsa and Wachner, 1999). This further led to the possibility to derive equation.2.1.30. Gimsa explains because of equation.2.1.25 allowed "us to establish the dependence of r_{infl} on the axis ratio of the spheroid." (Gimsa and Wachner, 1999). These derivations was used to simplify the expressions



$$CMF^* = \frac{1}{n} \frac{\Psi_e - \Psi_c^*}{\Psi_e} \quad (2.1.29a)$$

$$\text{with } \Psi_e = \frac{r}{r_{infl}} \Psi_0$$

$$\vec{E}_{loc}^* = E - \frac{n \vec{P}^*}{\epsilon \epsilon_0} \quad (2.1.29b)$$

Figure 2.11: Figure (left) is an Rc model consisting of RC pairs i, m and e describing the inner media, the membrane and the external media, respectively. Ψ_e is given in equation.2.1.29 and is the reference potential in the external solution at distance r from the symmetry plane. Over the membrane thickness d the potential difference $\Delta\Psi_m^*$ is induced. The denotation n is the depolarizing factor (see appendix.A).

of the characteristic equations (equation.2.1.26 to 2.1.28) and express the CMF by impedances in figure.2.11 as given in equation.2.1.30 below (Gimsa and Wachner, 1999):

$$CMF^* = \frac{1}{n} \left(1 - \frac{Z_i^* + Z_m^*}{Z_i^* + Z_m^* + Z_e^*} \left(\frac{r_{infl}}{r} \right) \right) = \frac{1 + \xi}{\xi} \left(1 - \frac{Z_i^* + Z_m^*}{Z_i^* + Z_m^* + Z_e^*} (1 + \xi) \right) \quad (2.1.30)$$

The scheme in figure.2.11 can be simplified in different ways to describe the three polarization plateaus and the two-dispersion process leading from one to another (see figure.2.9 for R_1, R_2) In figure.2.12 the criterion and simplified schemes for the derivation of the DP and ER spectra characteristics is presented.

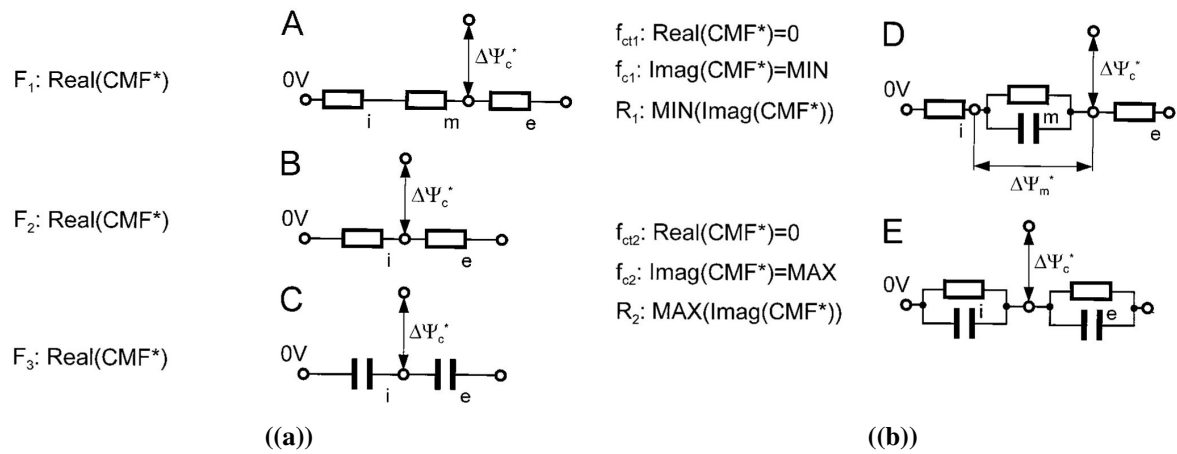


Figure 2.12: "Criteria and simplified schemes for the derivation of the DP (a) and ER (b) spectra characteristics"(Gimsa and Wachner, 1999) according to figure.2.9. Image source: (Gimsa and Wachner, 1999).

With increasing frequency, starting at DC the plateaus can be described by schemes in figure.2.12(a) for A, B and C directly cited from (Gimsa and Wachner, 1999):

Scheme A - First plateau (F_1):

"For DC and frequencies still too low for capacitive membrane bridging the ionic conductivities of all media determine the polarization. The Ohmic resistance of the cell membrane represents the highest impedance. The outer membrane side of the cell will be charged to a potential close to Ψ_0 . In analogy the internal membrane side is close to a potential of 0 V. Accordingly, the induced transmembrane potential $\Delta\Psi_m$ is at maximum."

Scheme B - Second plateau (F_2): *"After capacitive membrane bridging the polarization is described by the balance of the ionic conductivities of the internal and external medium. The induced transmembrane potential vanishes."*

Scheme C - Third plateau (F_3): *"Frequency-independent ionic conductivities are superseded by capacitive currents, and the polarization is described by the permittivity balance of internal and external medium."*

Schemes D and E in figure.2.12(b) is describing *"the transitions in between the plateaus A and B ($\beta 1$ dispersion) and B and C ($\beta 2$ dispersion). Each dispersion yields a phase shift between external field and cell surface potential, generating an ER torque in a rotating field. The torque is proportional to the imaginary part of the CMF"*(Gimsa and Wachner, 1999).

Scheme D - A and B (R_1, f_{c1}): ($\beta 1$ dispersion) From KHz to MHz frequency region. This dispersion is also called the membrane dispersion and scheme D represents where the real part of the CMF is zero, the imaginary part of CMF is at its minimum and R_1 is at its minimum (Often the maximum negative value). In this dispersion, the induced transmembrane potential transitions from its maximum to the induced transmembrane potential vanish after the membrane is completely capacitively bridged. After the membrane is bridged, the polarization is described by the balance of the ionic conductivities of the internal and external medium. Scheme D also describes the frequency-dependence of the dispersing transmembrane potential.

Scheme E - B and C (R_2, f_{c2}): ($\beta 2$ dispersion) which leads into the higher frequency range ($> 1 \text{ MHz}$). This dispersion is also called the bulk-media dispersion. Scheme E describes from where the polarization is described by the balance of the ionic conductivities of internal and external medium to where

the ionic conductivities that are frequency-independent get superseded by capacitive currents and the polarization is described by the permittivity balance of internal and external medium.

2.1.2.7 Electric field variations due to shape and design of the electrodes

In this section field calculation for different electrorotation electrode configurations and field distributions in an electrorotation chamber is presented. The work of Ralph Hölzel from 1993 (Holzel, 1993) surrounded simulations for a four-electrode configuration of two different shapes. The simulations were done to develop a method for calculating the distribution of rotating electric fields. Hölzel explains that by developing such a method it *“should allow one to optimize the electrode shape regarding minimal dielectrophoretic forces and to determine the actual field strength to extend the capabilities of the electrorotational method.”* (Holzel, 1993). The calculations were made by modeling the space between the electrodes in a network of regular resistors with given voltage at the electrodes. The electrode shapes presented from the work of Hölzel will be confined to electrodes of rectangular and circular shape. Hölzel also performed simulations for elliptically shaped electrodes and a variety of size in two dimensions and straight wire-like electrodes in the three-dimensional case. The software used for calculating the potential distribution is not declared but was used to determine the voltages and phases at the resistor network’s nodes. These values were then employed to calculate the field strength and its gradients. For electrodes of rectangular and circular shape Hölzel found out through his calculations that by comparing the spatial distribution of $E^2(x,y)$ and the gradient of E^2 in which areas the main contribution to field inhomogeneities occurred. These areas were found near electrodes with sharp curvatures and in regions of small electrode distance. Hölzel explains *“substantial difference of the weighted field strength between straight and bent electrodes, and makes circular electrodes preferable for electrorotation experiments.”* (Holzel, 1993).

Figure.2.13 illustrates regions with field inhomogeneities where figure.2.13(a) is for rectangular electrodes and figure.2.13(b) is for circular electrodes. The scales in both figures is linear and equal. In figure. 2.14 the dielectrophoretic forces is illustrated as gradient $F_{DEP} \sim -gradE^2$

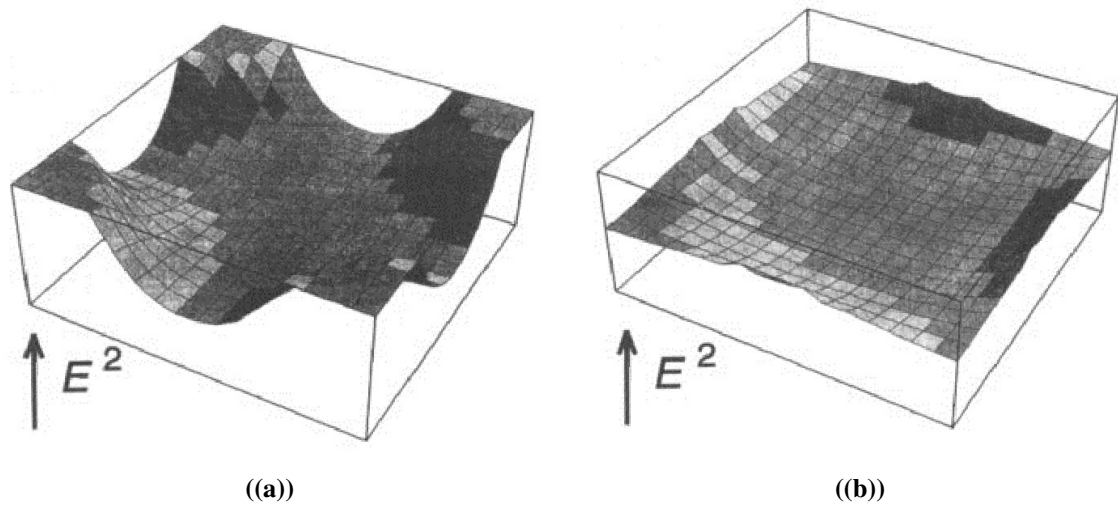


Figure 2.13

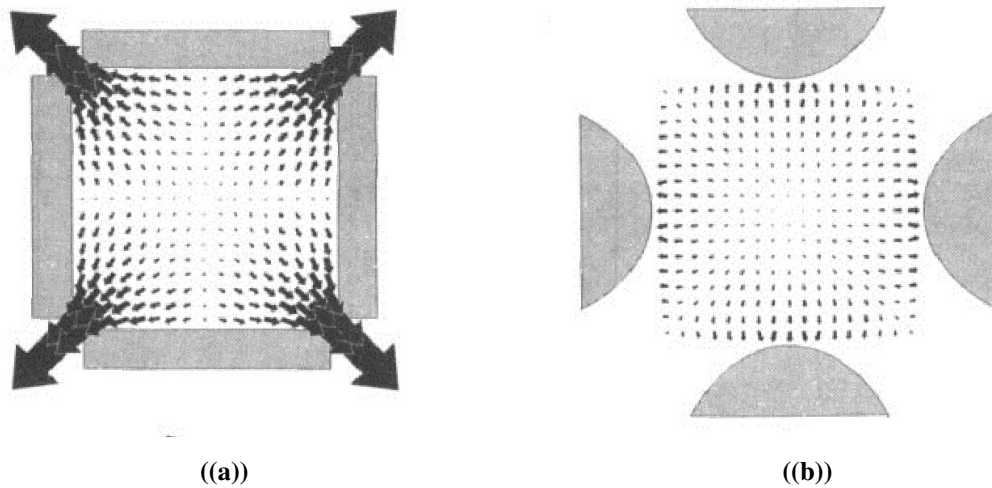
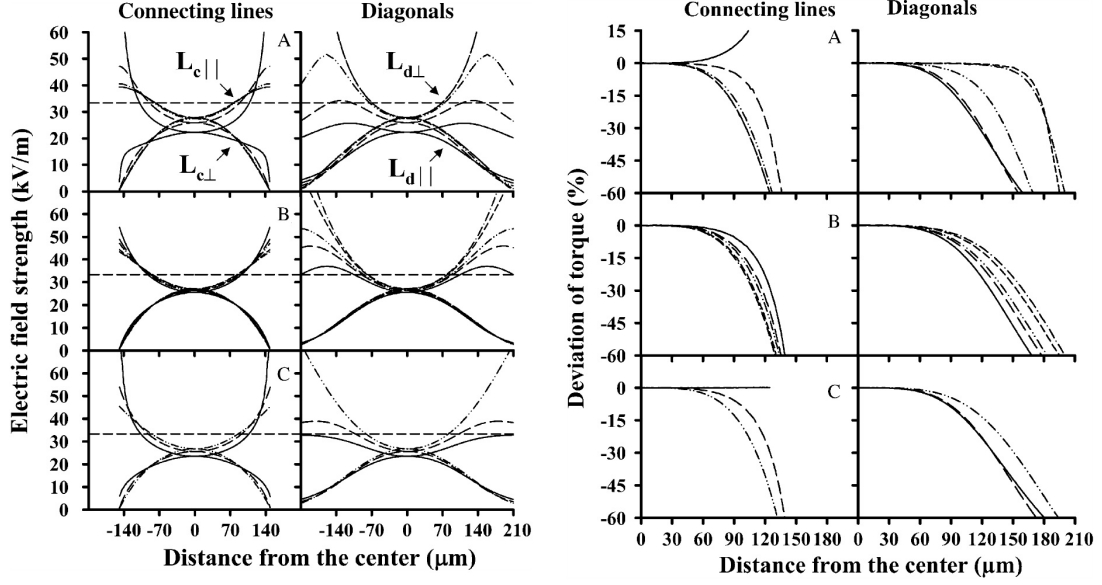


Figure 2.14

Similar studies of (Holzel, 1993) was done by Maswiwat et.al. in 2005 and published in 2006 (Maswiwat et al., 2006) on a four-electrode electrorotation setup for different shapes and sizes. However, with more modern computational technology and simulation tools available. Maswiwat was able to analyze the data from the numerical simulation done by using FEMLAB (Comsol, Sweden) with a sinusoidal signal driving the potentials of $10 V_{pp}$. Analogously, the fields were analyzed at a phase of 45° . The different electrode designs simulated is illustrated in the figure. 2.16. In (Maswiwat et al., 2006) it is explained that the field strength between two opposite electrodes is always influenced by the adjacent electrodes in a forming the perpendic-



(a) Electric field strength deviation according to the distance from the center (μm). (b) Deviation in torque according to distance from center (μm).

Figure 2.15: Figure illustrated deviation in torque and electric field strength according to different electrode designs. In figure (b) squared shaped electrodes are denoted (a), circular (b) and pyramidal and parabolic (c)

ular oriented electrode pair. The influences result in reduced field strength (E_0) in the center of the electrorotation chamber. E_0 is always lower than the calculated field strength for a single pair of parallel electrodes in the same plane ($E'_0 = V/d > E_0$). The correction factor of the circular field in the center is given by (Maswiwat et al., 2006):

$$r = \frac{E_0}{E'_0} \quad (2.1.31)$$

Maswiwat further explains that the electric field distributions for nine different electrode designs (see figure.2.16) showed that the direction and magnitude of the electric field depend heavily on the location within the electrorotation chamber and that of the shape of the electrodes. The field in the central regions is largely homogeneous, and in the vicinity of the electrodes, the field becomes largely inhomogeneous.

In figure.?? (a) the field strength for the different electrode shapes and phase angle calculated from simulations (Maswiwat et al., 2006) is illustrated. The spectra clearly indicated that the field strength decreases rapidly when the distance from the center deviates. The denotations $L_{c||}$, $L_{c\perp}$, $L_{d||}$ and $L_{d\perp}$ is explained as "The electric field strength varies along the connecting

lines $L_{c\perp}$ and $L_{c\parallel}$ and the two diagonals $L_{d\perp}$ and $L_{d\parallel}$ ” (Maswiwat et al., 2006). The diagonal lines is defined for 45° phase angle and the center lines for 0° phase angle. In the simulation performed (Maswiwat et al., 2006) the center field sternest varied between 24 to 28 kV/m, i.e. 72-84 percent of E'_0 . Figure. ?? is shown here to illustrate that the field strength decreases from the center of the electro chamber. The individual calculated for each electrode configuration from the results from Maswiwat’s simulation is found in (Maswiwat et al., 2006).

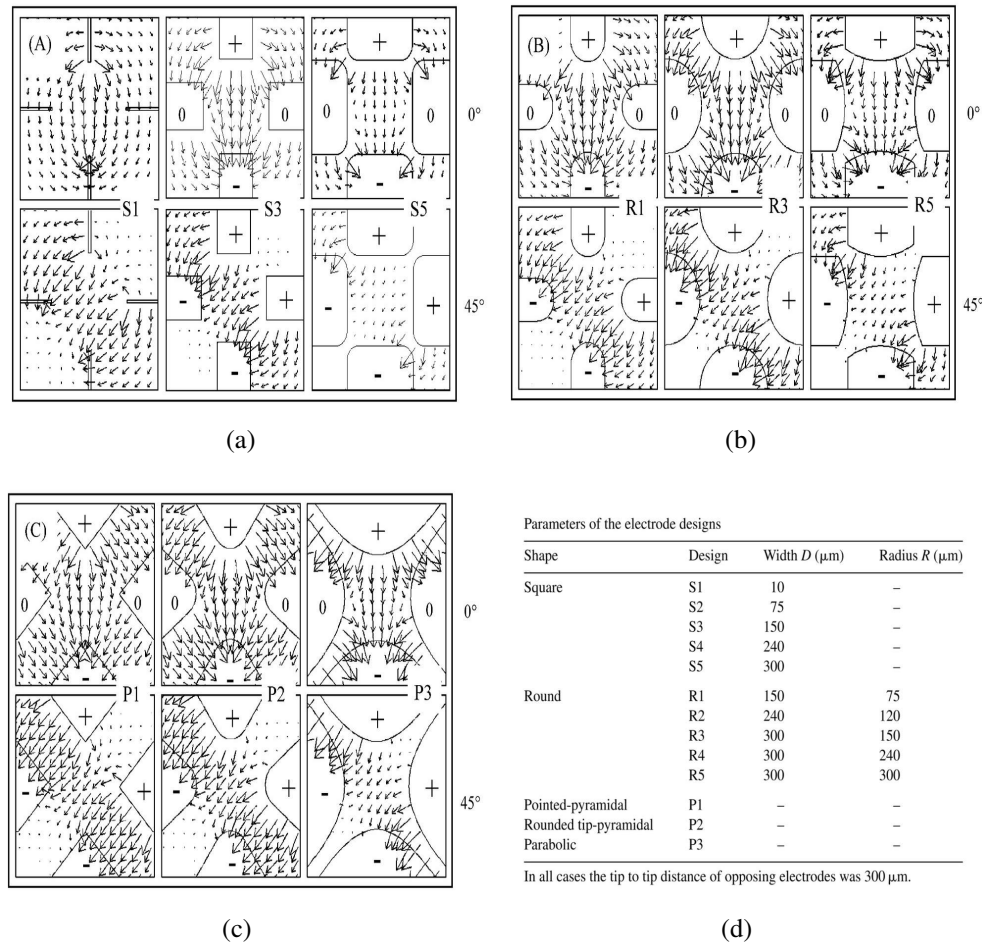


Figure 2.16: Electrode designs and electric field simulations. Top illustrations show a phase angle of (0°) and bottom illustrations a phase angle of 45° . (a) Squared (b) Circular (c) Pyramidal and parabolic an (d) Table for dimensions of the respective electrodes

Figure. ?? (b) from (Maswiwat et al., 2006) the deviation inexperienced torque is graphically presented. The result of these simulations found that by using a torque correction factor (r^2) and it the correction factor increased with the width for all electrode designs. “The torque deviation inside the measuring volume of the chamber is the most important characteristics for the usability of a rotation chamber. For a chip chamber the area with comparable torques limits

the useable area or the size of larger cells.”(Maswiwat et al., 2006). For comparison purposes a 10 percent torque deviation limit was set that resulted in a specific radius distance they called $S_{10percent}$. The circular shaped electrodes were the design that showed most equality according to the center and diagonal connecting lines. The squared electrodes showed very high values within the $S_{10percent}$ limit set for the diagonal, but low values for the center connecting the line. Maswiwat argues that the squared electrodes are less appropriate to use because of the narrow area around the center line the torque deviates less than 10 percent. The pyramidal and parabolic electrodes showed too high differences for the center line and diagonal. In (Maswiwat et al., 2006) the simulations show that an electrode setup with a higher width and rounded tips is the most appropriate according to their torque deviation analysis. It is also noted that *”Additionally, square electrodes generate extremely high field strengths at their sharp edges. This may lead to particle collection at the edges due to dielectrophoretic effects.”*(Maswiwat et al., 2006).

2.1.2.8 Rotational direction and other linked parameters

The rotational direction of a particle of ellipsoidal shape will rotate dependently on the particles dielectric properties, the frequency of the inducing external circulating field and the suspending external medium the particle is immersed in. Decided by these parameters the particle will either rotate with the direction of the rotating field (co-field) or in the opposite direction (counter-field). (Dalton et al., 2004).

From studies made on latex particles in 1987 by Arnold, Schwan, and Zimmerman this relation was explained as following (Arnold et al., 1987):

Forces exerted by an external field on a body submerged in a medium are functions of the complex permittivities of both object and medium (both being isotropic). The real and imaginary parts of the complex permittivities noted as ϵ^* and are further denoted as ϵ^{\Re} and ϵ^{\Im} . The imaginary part ϵ^{\Im} is a result brought from the conductivity. At a given frequency ω and $j = \sqrt{-1}$ and σ is conductivity:

$$\epsilon^* \equiv \epsilon^{\Re} - j\epsilon^{\Im} \equiv \epsilon^{\Re} - \frac{j\sigma}{\omega} \quad (2.1.32)$$

The transformation between permittivity and conductivity uses the relationship $\sigma^* \sim j\omega\epsilon^*$. Sim-

ilarly as in Eq.2.1.32 complex conductivity can be defined as:

$$\sigma^* \equiv \sigma^{\Re} + j\sigma^{\Im} \equiv \sigma^{\Re} + j\omega\epsilon^{\Re} \quad (2.1.33)$$

Further from (Arnold et al., 1987) states that the minus sign in Eq (??) contra Eq.(2.1.33) shows the usual convention. Further (Arnold et al., 1987) explains that a body is considered which is denoted by subscript (2) that is immersed in a medium denoted by subscript (1). A complex factor U^* is further used to simplify following calculations where U^* is considered as a macroscopic application of the *CMF*:

$$U^* \equiv \frac{\epsilon_2^* - \epsilon_1^*}{\epsilon_2^* + 2\epsilon_1^*} = \frac{\sigma_2^* - \sigma_1^*}{\sigma_2^* + 2\sigma_1^*} \quad (2.1.34)$$

If the medium is placed in a rotating external field of strength E it will be induced a rotating dipole moment in the immersed body. (Arnold et al., 1987) explains that a spherical shape of the body/particle is considered in this case where its radius is denoted as a and its complex dipole moment μ^* is given as:

$$\mu^* = 4\pi a^3 E \epsilon_1 U^* \quad (2.1.35)$$

(Arnold et al., 1987) explains that expressions above had at that time been identically derived by (Jones, 1984; Lovelace et al., 1984) and explains that the body will have a force acting upon it as a torque (L) which is a result from the vector cross-product between the external field and the dipole moment. This results in that only the imaginary components of the dipole moment is expected to contribute to following expression where μ'' is denoted as the imaginary part of the dipole moment:

$$L = -E\mu'' \quad (2.1.36)$$

If Eq. 2.1.36 is led by a negative sign it is an indication that the induced dipole moment vector of the body has an angle compared to the external field that is oriented in the opposite direction of the rotation of the field. Consequently, this leads to co-field rotation of the body and is given

by the negative values of the μ'' where only the imaginary components of the dipole moment are contributing. By Eq. (2.1.34) Arnold explains that this will implement that only the imaginary parts also of the complex factor U^* is contributing denoted as U'' . Antifield rotation will be observed when positive values of L from Eq. (2.1.36) is obtained.

Arnold mentions that it is disputable if the factor ϵ_1 from Eq. (2.1.35) should be assigned as complex or real. However, Arnold also mentions that robust and rigorous derivations (Jones, 1984) based on Maxwell stress tensor show that the real part of ϵ is the prominent and the quantitative influencing factor. Hence, the appropriate denotation for ϵ should be ϵ_1 (not ϵ_1^*). This is also consistent with results from (Sauer and Schögl, 1985; Lovelace et al., 1984). Since ϵ_1 is not given as frequency dependent, induced dipole theory underlines that the frequency dependence of torque is directly due to the frequency dependent factor U'' .

(Arnold et al., 1987) briefly elaborates on the relation of rotation speed ($\frac{\Omega}{2\pi}$) and the viscosity of the medium the particle is immersed in. Mathematical derivations show that rotation speeds become independent of the radius of the particle when a steady-state rotational speed (Ω_s) is obtained. Noted that since observed rotation speeds in Arnolds results is normally less than a few hertz, the surface of the microscopic particles used attains minimal Reynolds numbers (no turbulent flow). Arnold explains that as a cause of this the viscous drag is proportional to Ω (Lamb, 1906) where η is the absolute viscosity:

$$N = 8\pi a^3 \eta \Omega \quad (2.1.37)$$

The steady-state rotational speed (Ω_s) is reached when N becomes equal to L . By derivations from (Arnold et al., 1987) it is shown as mentioned above that mathematically with a combination of Eq. (2.1.36) and Eq. (2.1.37) that Ω_s is independent of the radius of the particle:

$$\Omega_s = -U'' \left(\frac{\epsilon_1 E^2}{2\eta} \right) \quad (2.1.38)$$

Arnold describes a case for a nondispersive particle with properties (ϵ_2, σ_2) and the properties

of the medium (ϵ_1, σ_1) that is considered frequency independent. The imaginary part of U^* is derived from Eq. (2.1.34) given following expression:

$$U'' = 3\omega \frac{\epsilon_2\sigma_1 - \epsilon_1\sigma_2}{(\sigma_2 + 2\sigma_1)^2 + \omega^2(\epsilon_2 + 2\epsilon_1)^2} \quad (2.1.39)$$

and differentiation of Eq. (2.1.39) yields the field frequency (f_0) giving further maximum torque:

$$2\pi f_0 = \frac{\sigma_2 + 2\sigma_1}{\epsilon_2 + 2\epsilon_1} \quad (2.1.40)$$

When substituting Eq.(2.1.40) into Eq.(2.1.39) reveals that the torque at maximum at given frequency will be proportional to:

$$U''_0 = 1.5 \frac{\epsilon_2\sigma_1 - \epsilon_1\sigma_2}{(\epsilon_2 + 2\epsilon_1)(\sigma_2 + 2\sigma_1)} \quad (2.1.41)$$

Further it is noted from (Arnold et al., 1987) that the value of f_0 from Eq. (2.1.40) is identical to what is predicted in the works of (Pethig and Willis, 1980; Schwan, 1957) on the Maxwell-Wagner dispersion of a very dilute suspension of particles. The numerator of Eq. (2.1.41) may either be positive or negative, implying that corresponding to this Maxwell-Wagner dispersion the particle rotation can be oriented either in an anti-field or co-field direction, respectively.

In the case above Eq. (2.1.39) to Eq. (2.1.41)) describes a non-dispersive particle. If a dispersive particle is considered, Arnold et al. (1987) explains that supposedly a particle exhibits a dispersion when placed in a field with such a low frequency that the permittivity of the medium can be neglected compared to its conductance. If these frequencies is restricted to values well below the value given by $\frac{\sigma_1}{2\pi\epsilon_1}$ it can be noted that $\sigma \gg \sigma''$ and by that $\sigma^* \approx \sigma$ showing its independent of f . This considerably simplifies the interpretation and therefore, at these low frequencies the conductivity forms of the equations derived above can be used.

Further from (Arnold et al., 1987) it is derived that if the particles dispersion time constant is τ , then:

$$\sigma_2^* = \sigma_{2t} + \Delta\sigma_2 \frac{j\omega\tau}{1 + j\omega\tau} \quad (2.1.42)$$

The denotation σ_{2t} describes the low-frequency limit of the particle conductivity and $\Delta\sigma_2$ is the increment (in most cases positive) in the conductivity related to the dispersion. The substantial basis of σ_{2t} could either be surface conductance or the conductivity through the material of the particle itself. As a notation from (Arnold et al., 1987) it is mentioned that in a case of liposomes or biological cells it would include a term that would be proportional to the membrane conductivity.

Earlier derivation from (Schwan, 1985) on surface conductance is used in (Arnold et al., 1987) to obtain the imaginary part of U^* given as:

$$U'' = \frac{3\sigma_1\Delta\sigma_2\omega\tau}{(\sigma_{2t} + 2\sigma_1)^2 + (\omega\tau)^2(\Delta\sigma_2 + \sigma_{2t} + 2\sigma_1)^2} \quad (2.1.43)$$

while the frequency of the field (f) that results in fastest rotation is given by:

$$2\pi f_0\tau = \frac{\sigma_{2t} + 2\sigma_1}{\Delta\sigma_2 + \sigma_{2t} + 2\sigma_1} \quad (2.1.44)$$

In (Arnold et al., 1987) it is explained that the permittivity (ϵ_1 as the real part) of the particle is neglected in Eq. (2.1.42) to (2.1.44). This is due to the consideration that the high-frequency limit of the particle conductivity must be capacitive and not just a purely real value which Eq. (2.1.42) describes. It is noted that by Eq.(2.1.32) it can be shown that even at conductivities as low as $6 \mu S/cm$ the error of neglecting ϵ_1 is negligible ($< 1\%$) at frequencies below 1.4 kHz. This further implies that Eq.(2.1.43) and Eq.(2.1.44) may be used to describe low-frequency peaks and Eq.(2.1.39) to (2.1.41) can be applied to the higher frequency results (100-500 kHz)

given in (Arnold et al., 1987) for which it is explained that it is not necessary *”to assume that the particle itself is undergoing a dielectric dispersion in order to explain the experimental data”* (Arnold et al., 1987).

2.1.2.9 DC and electrode deterioration

Deterioration or corrosion of the electrodes made of metals will always be present. In electrolysis, it is most common to use direct current (DC), but alternating current (AC) is also used but then for other means than, i.e., to solidify ions in the electrolyte at the electrodes. When DC is used the electrodes have definite polarity (fixed). The cathode is always negative and the anode always positive. In this thesis, all electrodes used are made of platinum which has properties giving the metal good resistance to corrosion and tarnishing. Platinum is grouped as a noble metal. It resists most acids and is used, e.g., as a catalyst in many contraptions. However, platinum immersed in an electrolyte will experience oxidation forming Pt^{2+} or Pt^{4+} . This will occur at the cathode where the platinum electrode will give off some of its electrons. Platinum is *”non-reactive”*, so this process will be a lot slower than that of non-noble metals like iron or zinc, but oxidation will occur in an electrolyte during electrolysis. Platinum is also resisting high temperatures and is a good conductor (Britannica, 2018a). Using DC the oxidation processes will eventually damage and alter the electrodes structure, and they will lose mass because of the electrolysis effects. Using an AC field, the heavier ions cannot follow the alternating current, and the oxidation effects are reduced to a minimum (Nandi, 2013). In Nandies research it is explained that highly mobile ions like H^+ and OH^- which will migrate to its respective cathode and anode, respectively, forming hydrogen gas and oxygen gas. In Nadies research this effect is observed at 50 Hz. Using electrodes with high resistance will in AC produce much heat, but materials like copper, silver, platinum (all good conductors) the heating effects are zero. (Nandi, 2013). To remove the DC contribution and protect the electrodes a capacitor can be placed in front of the electrode creating a high pass filter, and all the lower frequencies get filtered. An offset is often applied to a signal. This is done to ensure the peak-to-peak amplitude of a square wave or sinusoidal signal never becomes less than the recommended supply voltage power, e.g., an integrated circuit. The cutoff frequency is described bot for a low pass filter and a high pass

filter where $f_c CR$ is denoted for cutoff frequency, capacitance and resistance:

$$f_c = \frac{1}{2\pi CR} \quad (2.1.45)$$

2.2 Optical microscopy

2.2.1 Introduction

To measure the rate of rotation for an object manipulated by electrorotation visual data is needed. Optical microscopy is by far the most common approach and to this day the simplest method to accurately observe the excited objects. In order to make accurate observation it is pivotal to make recordings rich in detail, so the objects behaviour can clearly be distinguished and monitored. Rate of rotation can then quite accurately be documented just by observing the rotations within a known time frame. This can either be done by a classic stopwatch sequence or counting the rotations by looking at recordings frame by frame. The challenge lies in the acquisition of the recorded data and it is here the techniques of microscopy come to play. Microscopy is by itself a massive field of knowledge. Techniques are continuously evolving and being developed. The digital age has taken microscopy quantum leaps forward and have given the field a much wider area of use and new possibilities. Microscopy has many branches and the three most prominent are optical microscopy, electron microscopy and scanning probe microscopy (Spm). In this thesis only optical microscopy is used, so theory and explanations will be concentrated around this branch. Although it should be mentioned that the basic principals within microscopy share many of the same aspects and restrictions.

2.2.2 Köhler illumination

In light based microscopy illumination is critical. Only by focusing the light source onto the specimen correctly makes it possible to obtain images of greater resolving power and of high-quality. In bright field or reflective microscopy, the illumination is the most important variable. Köhler illumination was first introduced in 1893 by August Köhler as a method to obtain optimum specimen illumination (Zeiss, 2018c). The method is widely used and more or less recommended by all manufacturers of laboratory microscopes. Olympus is one of the leading companies within microscopy manufacturing and covers the fundamental and basics of theory describing Köhler illumination (Olympus, 2018a). Köhler illumination ensures that the light that covers the specimen is uniform and it reduces glare (Olympus, 2018a). Most modern microscopes are produced in such a way that the collector lens and any other optical component built into the base of the microscope will project an enlarged and focused image of the lamp

filament onto the plane of the aperture diaphragm of the sub stage light condenser that is properly positioned. These pre-adjustments of the lighting from the lamp filament is imperative to further obtain optimal illumination of the specimen. This is achieved adjusting the opening of the condenser diaphragm that controls the angle of all light-rays emerging from the condenser from all azimuths. Since the light plane is not directly focused onto the specimen all impurities as dust or imperfections on the glass surface of the condenser will not affect the lighting at the specimen level and will appear grain less and extended. Closing or opening the condensers aperture diaphragm controls the angle of the cone of light reaching the specimen and it is the aperture of the condenser diaphragm and the working numerical aperture of the objective that determines the total realised numerical aperture of the microscope system. Optimizing these settings will result in greater resolving power and light transmittance.

A more profound and detailed overview of Köhler illumination and the conjugate field and aperture planes is given in appendix E.

2.2.3 Numerical aperture of condenser and objective

2.2.3.1 Condensers numerical aperture

The numerical aperture (NA) of a microscope is more or less always just mentioned as a numeric measure concerning the microscope's objective(s). In truth numerical aperture is also strongly linked to the apparatus's light condenser. Zeiss is one of the leading manufacturer within microscopy and explain the importance of differentiating the numerical aperture of the condenser and the objective (Zeiss, 2018a). Light from the lamp filament is gathered by the condenser and focused into a cone shape that illuminates the specimen with uniform intensity throughout the complete field of view. The total NA obtained by the microscope system is limited to how much light the objective is exposed too. Therefor it is critical that the condenser is properly adjusted to gain optimised settings for the intensity and the angle of light entering the objective front lens.

The numerical aperture and the share size of the light cone is determined by the condensers aperture diaphragm. Adjusting the diaphragm will alter the angle of the illuminating light cone and there by the numerical aperture of the condenser. In optical microscopy illuminating the specimen is the most important controllable variable. The objective used is primarily the deciding factor for maximum obtainable resolution, but for utilising the objectives full potential,

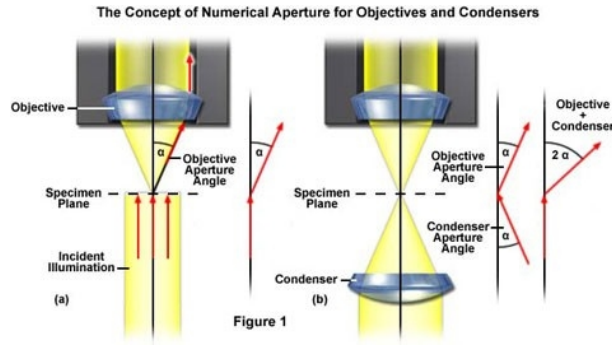


Figure 2.17: Figure 2.17(a) shows a simple microscope system without a condenser. Only a collimated light beam. The light diffracted by the specimen and cover slip is shown as a cone of light that is inverted and have a half-angle (α). This represents the limitation of light that can be gathered by the objective. To increase the effective aperture and resolving power of the system a condenser is added as shown in (b). The condenser generate a light cone on the illumination side of the specimen and by this enabling the objective to gather more light rays passing through the specimen as a result of larger diffraction angles. This increases the resolution of the microscope.(Zeiss, 2018b)

light from the specimen must be focused by the condenser so the cone of light illuminating the specimen coincides with the objective aperture. Recommended settings for the condensers numerical aperture control should be set to circa 80 % of the objective's numerical aperture. Using a higher numerical aperture for the condenser than of the objective will lead to loss of light gathered and by that loss of data. If the condenser aperture is matched correctly to the objective, optimum resolution for the system can be obtained.

2.2.3.2 Numerical aperture of the objective

Numerical aperture (NA) is defined as a measure of the solid angle that covers an objective and expressed as (Zeiss, 2018b):

$$NA = \eta * \sin(\theta) \quad (2.2.1)$$

where θ equals the maximum half-angle the cone of light falling upon or exiting a lens and η represents the refractive index of the immersion medium that occupy the space between the objective and the cover slip protecting the specimen. Some examples on refracting indexes for yellow light (wavelength equal to 589 nanometres : $\eta = 1.0003$ for air, $\eta = 1.333$ for water, $\eta = 2.417$ for diamond (Britannica, 2018b). Looking at equation (2.2.1) it is clear to see that only the refracting index (η) can increase the NA of the objective above 1.0. θ is the half angle of the light cone and can never surpass 90° thereby $\sin(90) = 1$. 180° is the highest angular

aperture a standard objective can theoretically obtain and in practical terms objectives that can master aperture angles exceeding 70 to 80 degrees are only found in high performance systems and are highly expensive.

Different mediums like certain oils (immersion oil) (Nikon, 2018a) as described above can be utilised to increase the numerical aperture. The immersion medium can alter the pathways of the light waves passing in the interface between the cover slip and the lens of the objective and by that increase the amount of light entering the objective. A substantial increase in NA is observed when a objective is designed to work in an immersion medium with a refracting index higher than 1.0. Common mediums are oils, water or glycerine. Figure 2.18 (Olympus, 2018b) illustrates that by closely matching the refracting index of the immersion medium and the material of the cover slip, the light rays will not deviate in the immersion medium due to refraction. The numerical aperture is increased by the factor of η which is the refracting index of the medium used. It should be noted when using immersion medium that has a much lower refracting index than that of the cover slip (for example air) that some light rays of a high obliquity ($\theta < 30^\circ$) will be reflected. This will contribute to internal reflections of light at the surface of the cover slip. this tend to degrade the resolution of the image.

Oil Immersion and Numerical Aperture

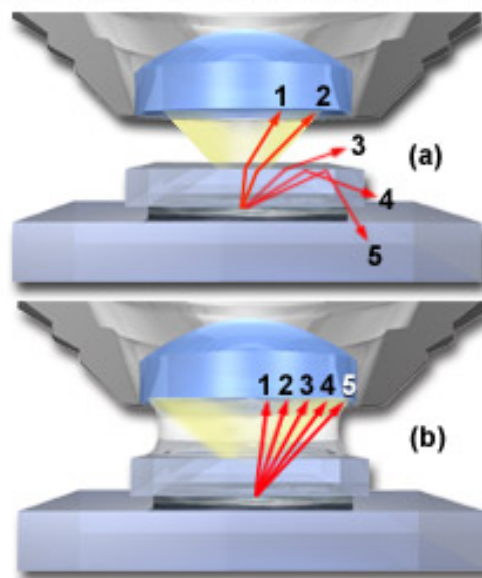


Figure 1

Figure 2.18: (a) is a system where an immersion medium of lower refractive index than of the cover slip is used while in (b) the same system is illustrated but here an immersion medium of equal refracting index has been used (Olympus, 2018b).

Objectives meant to operate in immersion mediums like oil or glycerine have limitation to

the numerical aperture level of the condenser. If an oil objective with the NA of 1.40 is used and the condenser only operated at a NA of 1.0 the systems total NA will be limited to 1.0. In such a system the optimal settings would be that the immersion oil would be placed in the interface between the front lens of the condenser and the underside of the specimen slide as well as the interface as between the first lens of the objective and the cover slip. This will ensure the utilisation of all the benefits from the immersion oil.

2.2.4 Microscope Resolution

Leica Microsystems and Martin Wilson (Wilson, 2016) states that the term "resolution" regarding microscopy is the microscope system's ability to distinguish detail. More carefully explained this states that resolution is described as the minimum distance two distinct points of a specimen can be observed. This is either by the observer or the microscope camera as separate entities.

Numerical aperture of the optical components and the the wavelength of the light used is the prominent factors deciding the resolution of the microscope. In addition to these two factors the diffraction limit of light needs to be considered first described by Ernst Abbe in 1873.

Resolution is closely linked to the numerical aperture when the microscope system's optical components are aligned correctly and working in harmony which will lead to more of the image details will being resolved. The wavelength of the light used to illuminate and image the specimen is also intrinsically linked to the total resolution. Shorter wavelengths of light are more capable of resolving greater detail than longer wavelengths. When dealing with resolution there are three mathematical concepts that needs to be taken into consideration. Abbe's Diffraction limit, Airy discs and The Rayleigh criterion.

2.2.4.1 Airy discs and George Biddell Airy

George Biddell Airy (1801-1892) was an English mathematician and astronomer. In year 1835 he publshied a paper in the Transactions of the Cambridge Philosophical Society entitled "*On the Diffraction of an Object-Glass with Circular Aperture*". Airy wrote this paper very much inspired in the field of astronomy and in it he describes "*the form and brightness of the rings or rays surrounding the image of a star as seen in a good telescope*". Despite that this paper was

written for a different scientific field it is relevant to other optical systems including microscopy (Wilson, 2016).

In a perfectly aligned system an Airy Disc is the optimally focused point of light which can be determined by a circular aperture limited by diffraction. An Airy disc viewed from above appears as a point of light surrounded by concentric rings. These rings are more correctly known as Airy Patterns and is illustrated in figure 2.19.

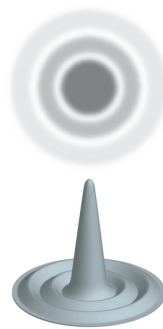


Figure 2.19: An Airy Disc illustrated from above and on the side with its central point having a maximum light intensity in its centre surrounded by concentric diffracted rings(Wilson, 2016).

The diffracted concentric light rings in figure 2.19 is determined by the wavelength of the light and the total numerical aperture the light passes through. The central disc with the highest intensity is referred to as the "airy disc" and the diffracted concentric rings surrounding the disc combined forms "Point-spread function" called an Airy Pattern. In figure 2.19 this pattern is represented by the three-dimensional illustration. The central point of the Airy Disc contains approximately 84% of the light intensity while the remaining 16% is left to the diffraction pattern surrounding this centre point.

The image viewed of a specimen in a microscope is made of many of these points of light and is more appropriate to be viewed as many Airy Patterns than single points of light as the term "Airy Disc" is described.

Resolution is tied to the size of the radius (r) of the central disc in an Airy patterns (Olympus and Spring, 2018). Two adjacent Airy discs are just resolved when the center of the Airy patterns are separated by a minimum distance (D) equal to (r). In an ideal case were the objective is aberration free with uniform circular aperture and the objective's numerical aperture is matched

to that of the condenser the radius (r) is given by the equation:

$$r = \frac{1.22\lambda}{NA(obj)} \quad (2.2.2)$$

where λ is the wavelength of light and $NA(obj)$ is the numerical aperture of the objective (and condenser). For the definition of numerical aperture (NA) see section 2.2.1. If the objective and and condensers numerical aperture is not matched the equation given for (r) is :

$$r = \frac{1.22\lambda}{NA(obj) + NA(cond)} \quad (2.2.3)$$

Both NA for objective and condenser is individually given by equation 2.2.1.

2.2.4.2 Abbe's Diffraction Limit (1873)

Ernst Karl Abbe (1840-1905), a German mathematician and physicist, was the first person to define numerical aperture. Abbe published in 1873 his theories and formulas that explained the limits of diffraction for a microscope. Abbe had discovered and recognised that the images formed of the specimen were composed of multitudes of adjacent, overlapping, intensity-varying, diffraction-limited points known as Airy Discs (See 2.2.4.1) (Wilson, 2016).

Despite all progress within optical microscopy recent years there are still some boundaries that can not be overcome by rational alterations to the objective lens or aperture design. Optical microscopy is governed by sets of physical laws that restricts resolution and this resolution limit is often referred to as the diffraction barrier. An optical instruments ability to distinguish between objects separated by a lateral distance less than half of the wavelength of light used to image the specimen (Silfies et al., 2018).

The process of diffraction involves the spreading of light waves that has illuminated a specimen that is composed of intricate structures. The images of the specimen observed by the optical microscope is composed of multiple point sources of light, the diffraction barrier concept centres around describing the wave fronts of a single point source of light passing through the microscope system contributing to form an image. The emission of wave fronts that is emanating from the specimen plane will be diffracted and by this effectively the wave fronts will be spread forming an image consisting of point sources of the specimen broadened into a diffrac-

tion pattern having a central disc of finite (Airy Disc), but is larger of size than the original point source. Hence, due to diffraction of light, the specimen will never be perfectly represented in the image formed because there exist a lower limit below an optical microscope system are able to resolve all structural details. Additional to the phenomena of diffraction that occurs to divergent light waves in an optical microscope the phenomena of interference also plays it part. Interference can be described as the recombination and summation of two or more superimposed wavefronts. Interference of light in optical microscopy plays a central role in all aspects of forming an image. Both interference and diffraction are responsible for the creating the real image in the intermediate image plane in the microscope. Interference between two wavefronts will double the amplitude of the combined wavefront if they are in phase (constructive interference), but will cancel each other out completely if they are out of phase by 180° (destructive interference). However most inference occurs somewhere in between. The photon energy in a light wave is not in it self doubled or annihilated when two waves interfere. The energy is rather channelled during diffraction and interference processes in direction permitting constructive interference. Because of this diffraction and interference should be viewed upon as phenomena involving redistribution of light waves and photon energy.

As described in section 2.2.4.1 the generated image in the intermediate plane consists of diffraction patterns (Airy Pattern) that is there again a product of interference. Associated with Abbes diffraction theory, the bright central region of the diffraction pattern is referred to as the Zeroth-order diffraction spot while the rings are called the first, second, etc., diffraction rings. When the microscope system is properly focused the light intensity at the minimum between the diffraction rings is considered as zero and this diffraction pattern is also known as the Airy Disc. In terms of resolution, the radius of the diffraction patterns Zeroth-order diffraction spot (Airy Disc), the expression for lateral radius (x,y) and axial radius (z) in the image plane is given by (Silfies et al., 2018):

$$Abbe\ Resolution_{x,y} = \frac{\lambda}{2NA} \quad (2.2.4)$$

$$Abbe\ Resolution_z = \frac{2\lambda}{NA^2} \quad (2.2.5)$$

where λ is the average wavelength of the light used to illuminate the specimen and NA as described in section (2.2.3). From equation (2.2.4) if λ decreases or NA increases, the radius given as Abbe Resolution will get smaller which implicates better resolution. The image spot size produced using green light (550 nanometers) by a 100x magnification objective with a numerical aperture of 0.9 is approximately 300 nanometers, but with same settings with an objective with numerical aperture of 1.4 will result in a radius of 200 nanometers which is almost half.

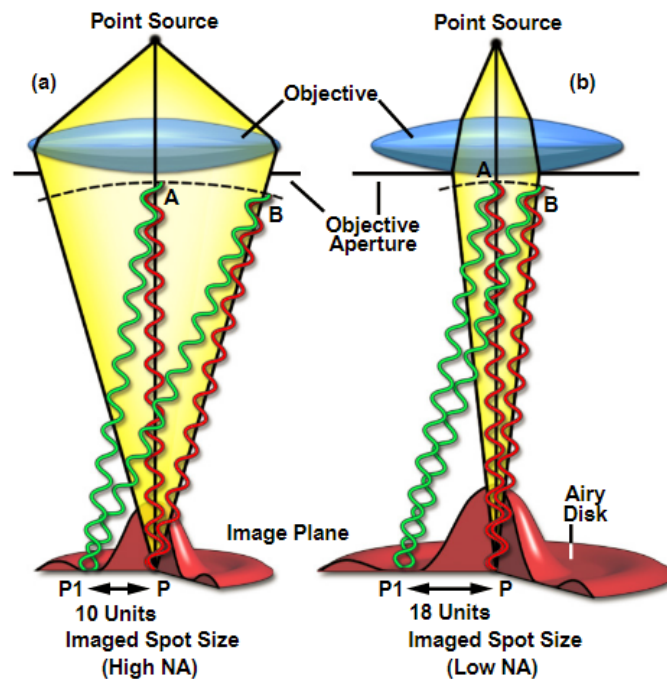


Figure 2.20: Figure above illustrates the effect of the objective aperture angle have on the size of the produced diffraction spot for a standard optical microscope. The point source and its conjugate (P) is shown in the image plane and is illustrated how wavefronts converge in constructive and destructive interference. Figure (a) shows a system of large NA and figure (b) with a smaller NA. The point P1 is moved laterally outward from the central disc of the Airy Pattern in the image plane until destructive interference is experienced at a certain distance which is defined as the location of the first diffraction minimum which by there defines the diffraction spot (Zeroth-order diffraction spot and first diffraction ring). Figure (a) is a higher resolution configuration than (b). The point A and B in the wavefront produce a smaller diffraction spot in (a) with a arbitrary size of 10 units compared to (b) with the lower resolution configuration the arbitrary size is 18 units. In (b) the reduced aperture angle increases the distance between P and P1 because of the narrower gap between A and B. this implies that light emitted by a point source is focused by the objective at the image plane (focus plane), travelling the same distance to arrive in phase and constructively interfere to produce a diffraction spot with high intensity. Destructive interference that leads to lower or zero intensity is generated by wavefronts arriving at the image plane one-half wavelength out of phase. The drop in intensity is gradual along the lateral axis of the diffraction spot and because of this, two point sources with a distance closer together than the size of the diffraction spots radius will appear to be a larger, single spot and are unresolved.

The only mechanisms to optimise spatial resolution and image contrast is to minimize the size of the diffraction-limited spots by decreasing the wavelength of light used to produce the image, increase the numerical aperture or to use an immersion medium having a larger refractive index (see section 2.2.3.2). However, under ideal conditions using the top shelf selection of optics, lateral resolution (x,y) is still limited to a spatial resolution approaching 200 to 250 nanometers. This is due to the transmission characteristics of glass at wavelengths under 400 nanometers and direct physical constraints on numerical aperture.

In contrast, when looking at the Point-spread Function (PSF) we are looking in the axial dimension of the Airy Disc. The elongated geometry of the PSF along the optical axis arises from the nature of the non-symmetrical wavefronts exiting the microscope objective. In optical microscopy axial resolution is even worse than lateral resolution. Equation (2.2.5) shows that with optimal settings the the lower limits using visible light would be in the range of 450-500 nanometers. Imaging highly convoluted objects, such as cellular organelles, diffraction-limited resolution is manifested as poor axial sectioning capabilities and lower contrast in the imaging plane. When imaging three-dimensional shapes, the overall specimen contrast is generally dominated by poor axial resolution that is a result of out-of-focus light due to interference with the PSF (Silfies et al., 2018).

2.2.4.3 The Rayleigh Criterion

The diffraction-limited resolution theory presented by Ernst Abbe in 1873 was later refined by the 3rd Baron of Rayleigh, John William Strutt, English physicist and author. Abbes resolution equation (2.2.4) was further developed by Rayleigh in 1896 and the resolution formula is given as (Silfies et al., 2018):

$$Rayleigh\ Resolution_{x,y} = \frac{0.61\lambda}{NA} \quad (2.2.6)$$

Equation (2.2.6) quantitates the measure of needed separation distance between two airy patterns in order to be able to distinguish each pattern as a separate entities. Rayleigh invented this criterion and it was built upon the work of George Airy. When using the theory of Airy

Discs, if two point-spread functions (PSF) is not overlapping they are distinguishable and "well resolved". They fulfill the Rayleigh Criterion. If the same two Airy Discs just is overlapped by each other by the first minimum of the PSF of both of the discs they fulfill they still fulfill the Rayleigh Criterion but are stated as "just resolved" and distinguishable as two separate points of light. If the the distance between the Airy Discs becomes closer than this, they fail the Rayleigh Criterion and is termed as "not resolved" and the two points of light will not be possible to distinguish them from one another (Wilson, 2016).

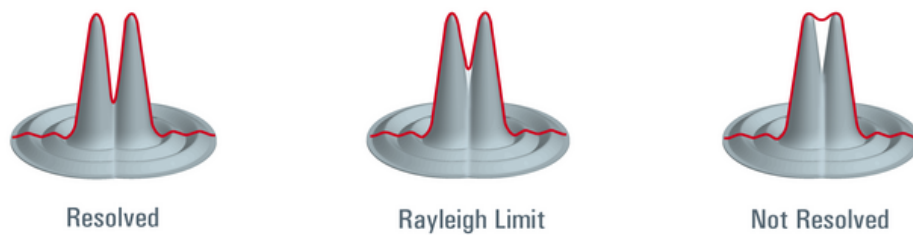


Figure 2.21: The limit of resolution illustrated as overlapping Airy patterns formed by two Airy Discs at different adjacent distances (Wilson, 2016). *Left: Well resolved Mid: just resolved Right: Not resolved*

2.2.4.4 Matching camera and optical resolution

To ensure that the digital image acquired contains all the data of the object the microscopes own resolution is not enough. The Nyquist theorem is just as deciding in digital sampling as in all other fields of sampling. The Rayleigh criterion describes the minimal distance between two airy discs needed to separate them (see 2.2.4). The Rayleigh criterion calculation gives a numerical value for distance and the smaller the distance needed to separate two airy discs the higher the resolution. Digital imaging is related to the pixels that detects the photons and samples the light that builds the image. To fulfill the Nyquist sampling theorem for a digital image the resolution of the smallest object wished to be recorded has to half its size. This means that if you're looking at a particle that is $10\text{ }\mu\text{m}$ the minimum sampling resolution distance needed to sample the particle is $5\text{ }\mu\text{m}$. To extend this further to the digital sampling concerning pixels this will mean that a minimum of two pixels must cover the wanted resolution or one pixel should be half the size of the object recorded. Nyquist sampling ($f = d/2$, where d = the smallest object, or highest frequency wanted to be recorded. (Berkley, n.d.).

Nico Stuurman from the University of California explains using an example where the

Rayleigh criterion is calculated to be of a resolution limit of 220 nm. Using an 100x magnifying objective the resolution limit of 220 nm would correspond to 22 μm in the camera plane (resolution limit x magnifying factor). Fulfilling the Nyquist criteria the pixel sizes used to record the image to match the microscopes resolution would be 11 μm or smaller (At least half of the resolution in camera plane). (Stuurman, 2018).

Method and materials

3.1 Introduction

This chapter contains all aspects regarding the progression through the thesis, concerning used materials and equipment as well as what methods that were applied to prove and investigate the concept of electroration. From paper sketches to the final designed circuit as well as all alteration done as the project advanced. Electroration have never been explored at the University of Oslo before and in the nature of this all designs and methods were approached as a learning-by-doing process. As the process was ongoing, alterations where needed to be implemented to improve the functionality and accuracy of the system. This includes every segment from e.g. circuit design, electrode-well alteration, optimizing signal configurations, correctly using an optical microscope to the basic matters as storing and handling sterile water used in the lab work.

The concepts of electroration was chosen to be investigated and tried for this thesis. In 2013 Professor J. Gimsa from The University of Rostock sent an envelope to Professor O.G Martinsen containing two electrode chambers, some cover slips and a PCB-connector for the electrode chamber and hand written letter of one page with seventeen lines describing how to get started to construct a basic electroration device. The reason for mentioning this ”story” is not just that it is a really charming way to start an approach to something entirely new and unknown, but it severely underlines from where and how this thesis started and how the thesis in its wholeness has been a learning-by-doing process from start to end. (Nikon, 2018*b*).

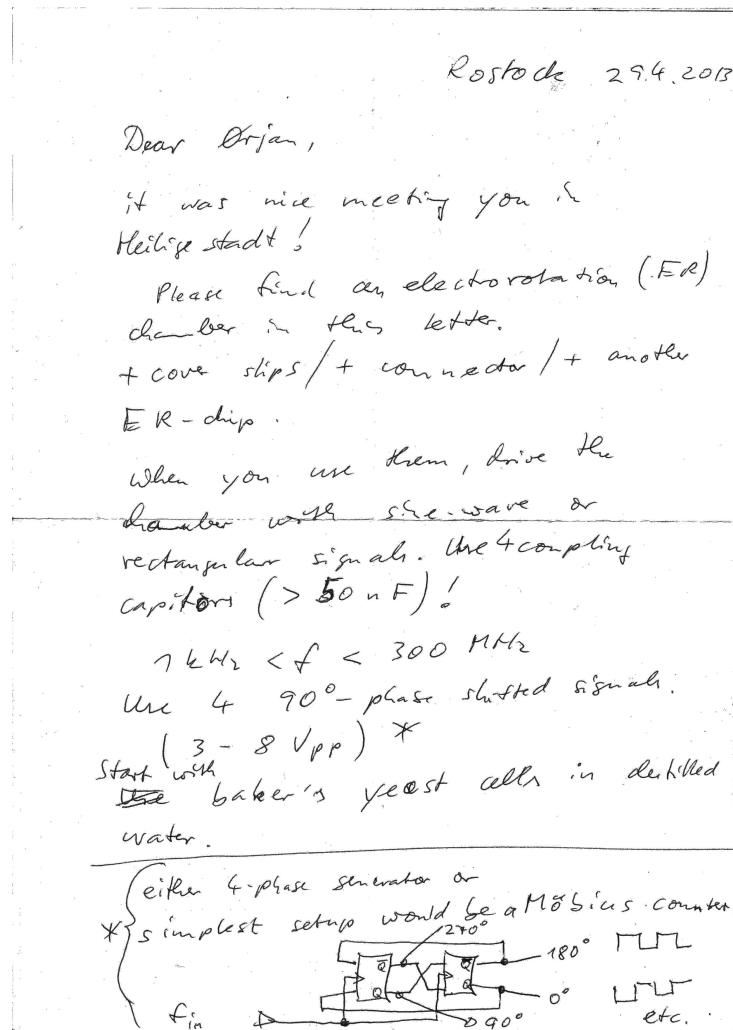


Figure 3.1: The letter from Professor J. Gimsa describing how to get started to construct a basic electrorotation device.

3.2 The circuit from paper sketch to final design

The instructions from the letter mentioned above illustrated in figure. 5.1 explains an approach to construct a basic circuit that will phase shift a signal to four electrodes by 90° so the signal will be shifted to each electrode by 90° , 180° , 270° and 0° , respectively.

3.2.1 The electrode chamber

The heart of the circuit was the electrode chamber. It was acquired from The University of Rostock where it had been designed and made. The electrode chambers is made up of two parallel polymer substrates with a platina electrode layer on top of the bottom substrate. The top substrate is of a smaller dimension than the the bottom substrate and a circular cut has also been made in center. The function of the circular opening in the top substrate works as a well where the electrodes are exposed. The well is is designed to hold a sample of the particle emulsion to be tested. The well has a 0.114 mm depth. The sides of the top substrate leaves ca. 2 mm distance where the bottom substrate with the electrodes are also exposed. The exposed sides here is where its possible to connect the electrode layer to a circuit. All dimensions for the electrode chamber is shown in figure. 3.3 and figure. 3.4. Figure. 3.2 shows the dimensions

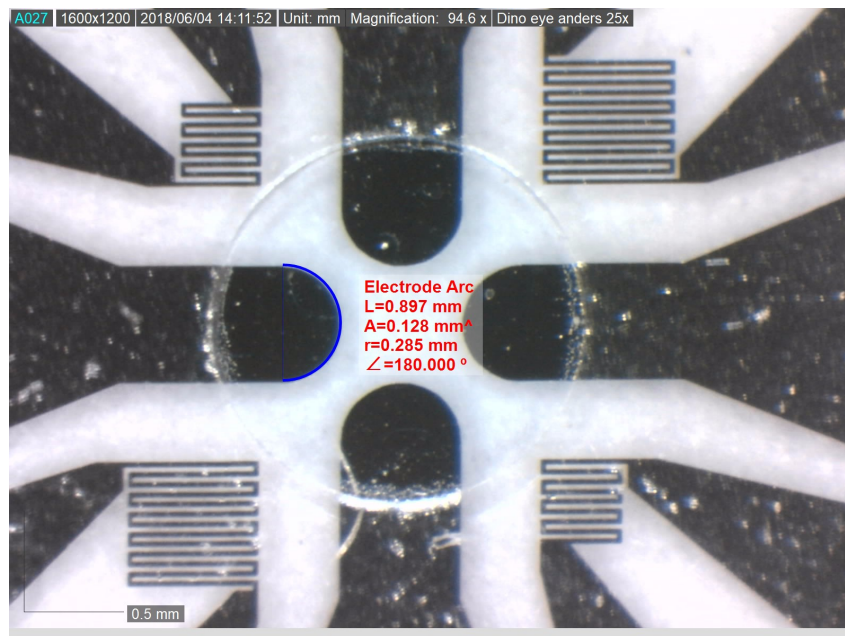
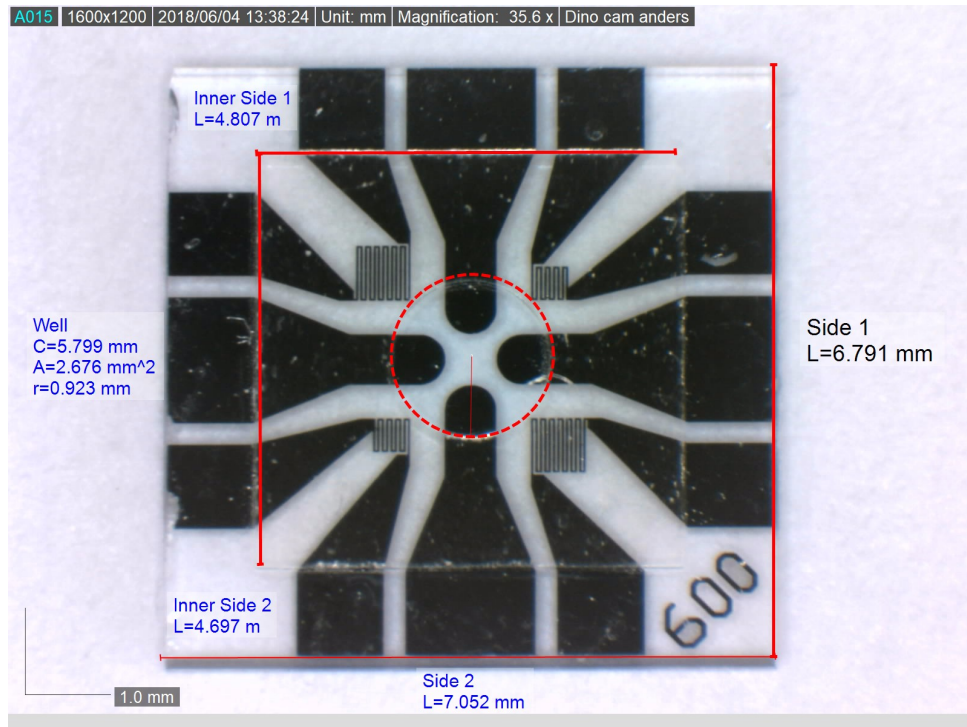


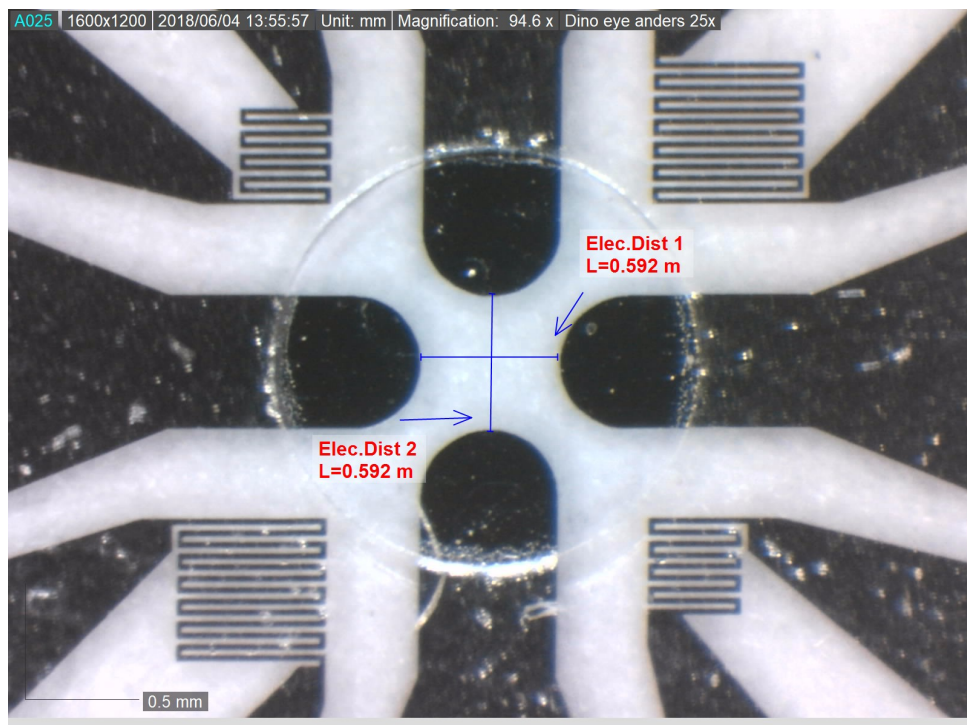
Figure 3.2: Arc of the the electrode tip. Radius of the arc was 0.285 mm resulting in a electrode width of 0.57 mm or $570 \mu\text{m}$.

of the the arc of the electrode tips. The width of the platinum electrodes was $570 \mu\text{m}$ for each

of the four electrodes.

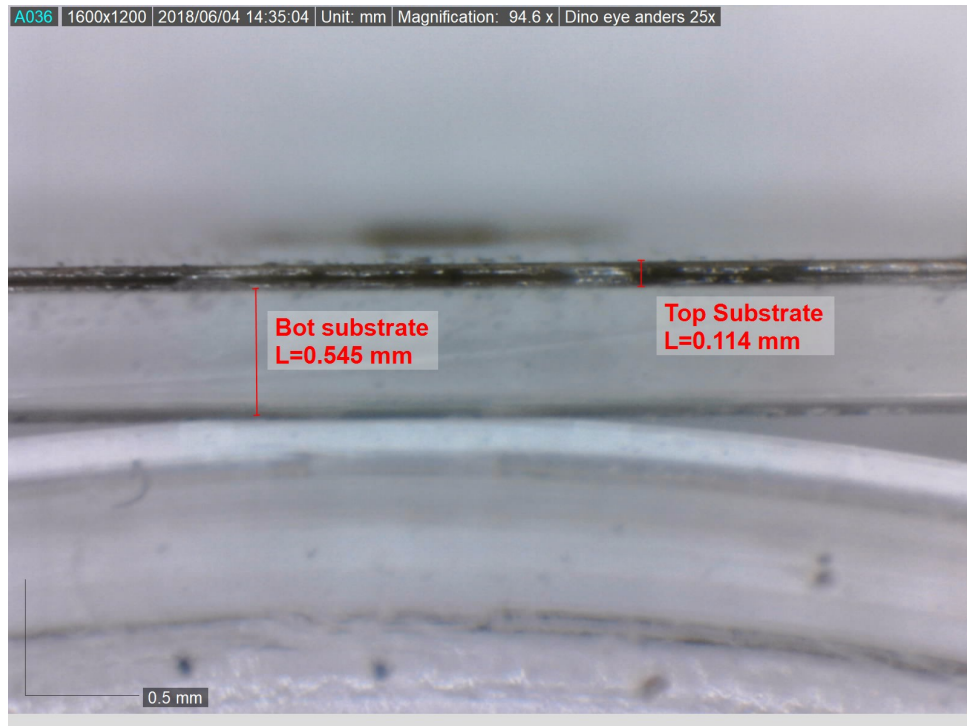


((a)) Fig (a). Top view substrate side measurements.

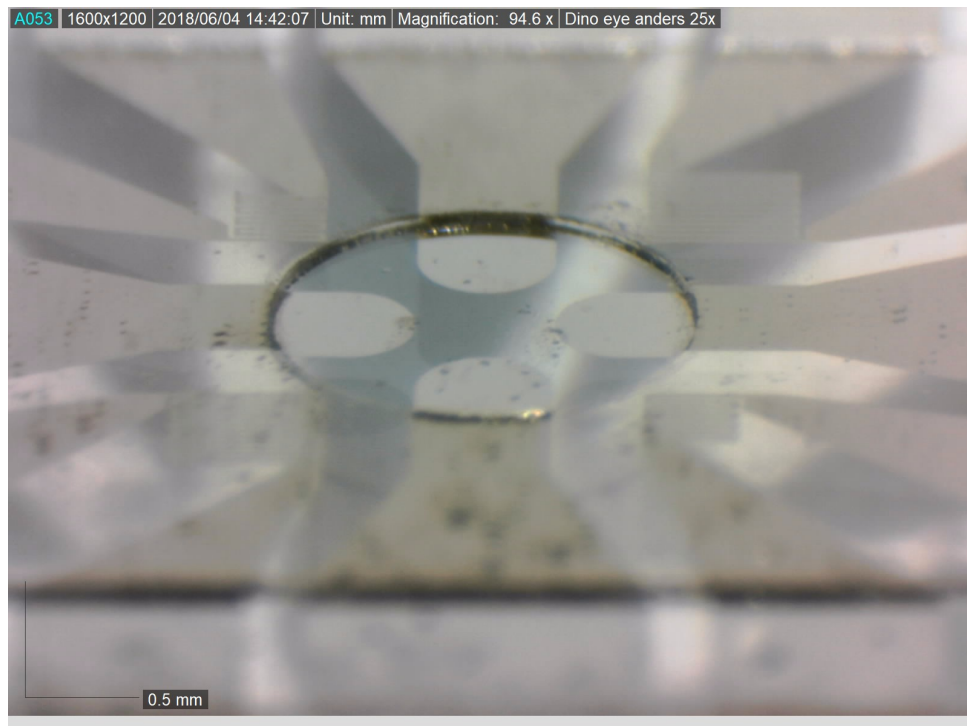


((b)) Fig (b). Distance between electrodes.

Figure 3.3: Measurements of electrode chambers sides, center cavity and electrode distance.



((a)) Fig (a). Top and bottom substrate thickness.



((b)) The cavity in the top substrate where the electrodes are exposed forming a well.

Figure 3.4: Substrate thickness and center cavity of the top substrate

3.2.2 PCB - Design, production and assembly

3.2.2.1 PCB design

The electroration circuit design was realised by using a dual D Flip-Flop as the integrated circuit that phase shifted the signal 90° on each of the four electrodes connected to the electrode chamber. The IC was wired as an alternative ring counter or an Möbius counter. This was realised by connecting \bar{Q}_2 on dual D Flip-Flop to D_1 in a feedback loop and Q_1 connected to D_2 . The four signal pads for each electrode was collected from Q_1 , \bar{Q}_1 , Q_2 and \bar{Q}_2 . Viewed from a direction were north is electrode with phase angle 0° and south electrode is 180° the direction of the electric field will rotate anticlockwise (see figure.3.1). The signal from each electrode was tested at the electronics laboratory at UIO by applying a squared wave clock signal proving the signal was phase shifted 90° for each signal-line (see figure.3.5)

Electrorotation device signal truth table			
Q_1 (270°)	\bar{Q}_1 (90°)	Q_2 (180°)	\bar{Q}_2 (0°)
0	1	0	1
1	0	0	1
1	0	1	0
0	1	1	0
0	1	0	1

Table 3.1: Truth table for the ER-device proving the signal measurements from figure.3.5

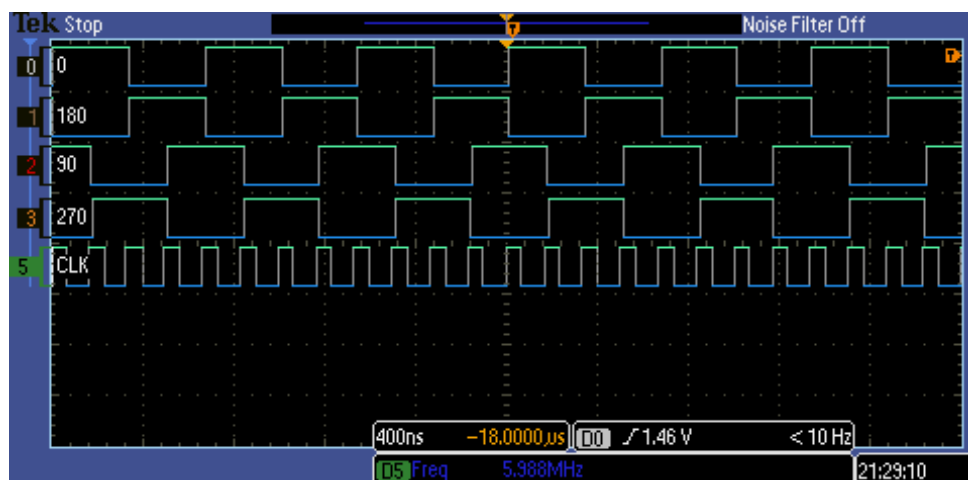


Figure 3.5: Signal measurements done at the electronics laboratory at UIO.

The design for the circuit was done in Cadstar 17.0 from Zuken. Two layers was used to realise the circuit. Top layer contained most of the routing using standard optimal width settings for the signal paths at net route code Nom. 0,20 / 0,15 mm with 0,5 mm thickness and for the power/GND lines were routed in code Nom. 0,20 / 0,15 mm with 1 mm thickness. The bottom layer was designed as a ground plane, but containing one electrode signal line and some routing connections to the dual D Flip-Flop. Routing and circuit schematics designed is illustrated in figure.3.6 and 3.7.

The dimensions of the electrode chamber was carefully measured and implemented into the design. Four pads were placed in correlation to midpoint of all sides of the electrode chamber with correct spacing leaving some space to solder a connection between the signal lines and each respective electrode. The dimensions chosen for the PCB board was 30 X 70 mm which is slightly bigger than a typical microscope slide. These measurements was taken into consideration to fit standard microscope slide holders.

Two decoupling capacitors were implemented in the design on the Vcc input line. This was mainly done to suppress noise in the power signal (especially in the higher frequency range) and the decoupling capacitors also work as small power reservoirs for the IC. Decoupling capacitors are also often named bypass capacitors from bypassing the power supply. It is in general viewed as a good routing practice to implement a decoupling / bypass capacitor on all power lines as close as possible to the Vcc input of the component. In this case the two capacitors with values 10 μ F and 100 nF was placed close to the power connector and the Vcc input of the IC. The capacitors was connected to ground. The dual D Flip-Flop package used was produced by Phillips with model number 74HC74D (Full: 74HC74D-906860Q-Hnn9401P). The maximum clock frequency for the IC is given as 76 MHz and the supply voltage given as $V_{CCmin} - V_{CCmax}$ at 2V to 6V, respectively (Philips, 2003). As a notation the IC was replaced once because of malfunction. Replacing the component and small repairs were done at the electronics laboratory at UIO.

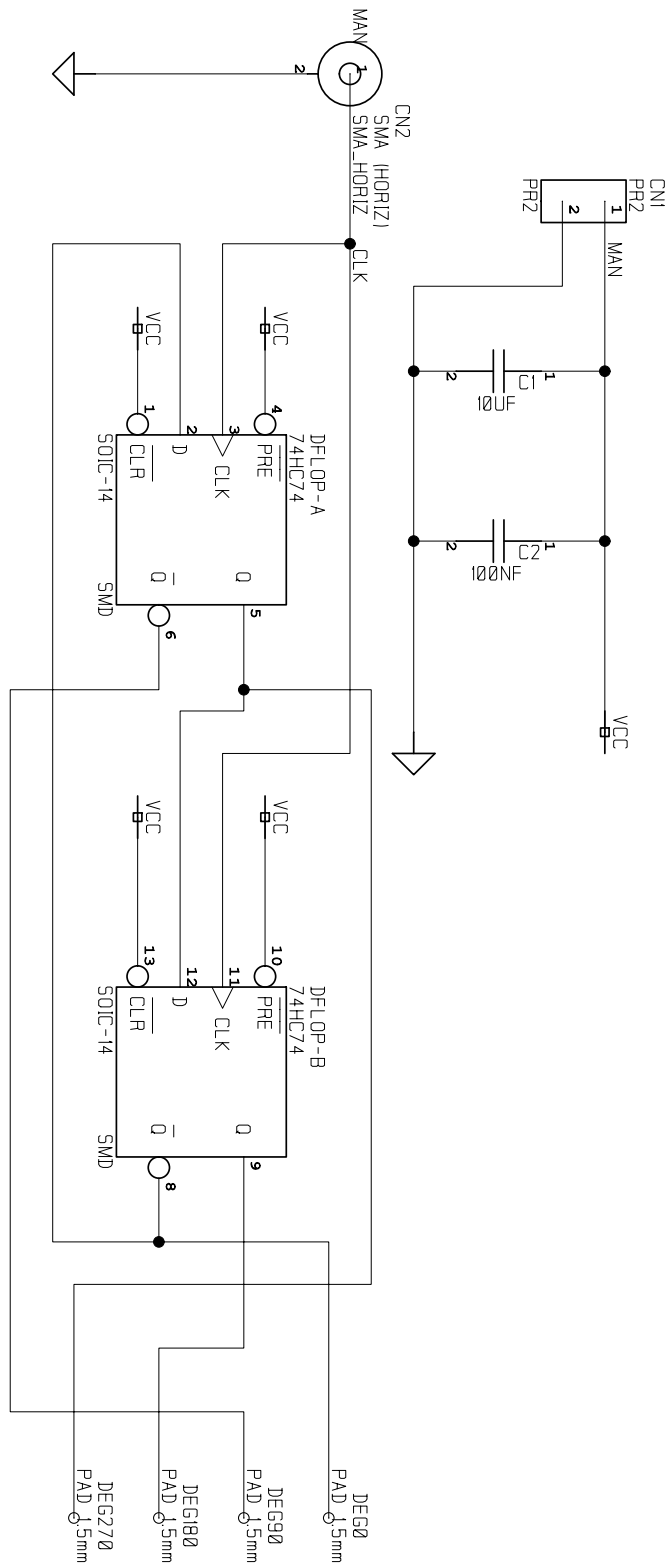


Figure 3.6: Schematics for prototype electrorotation device made in Cadstar 17.0. This was the final setup that was used to produce the final PCB.

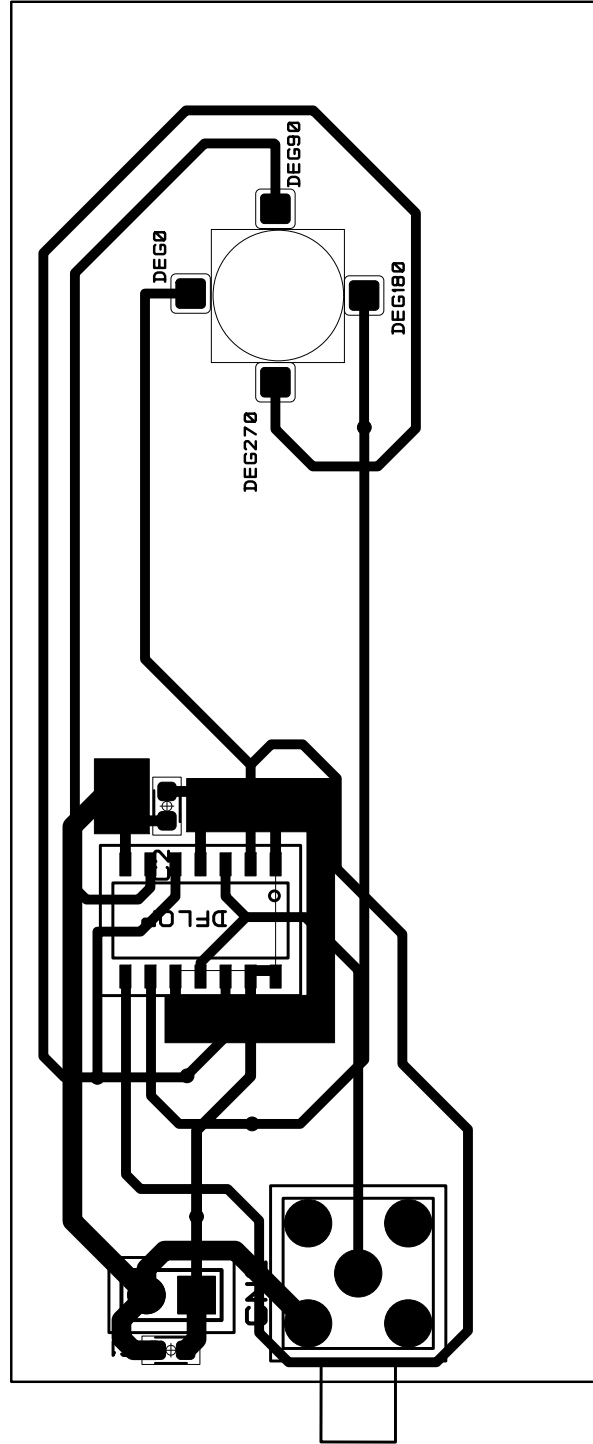
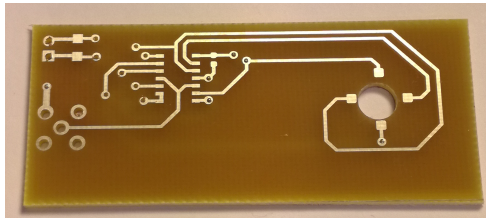


Figure 3.7: Routing schematics for prototype electrorotation device made in Cadstar 17.0. This was the final setup that was used to produce the final PCB.

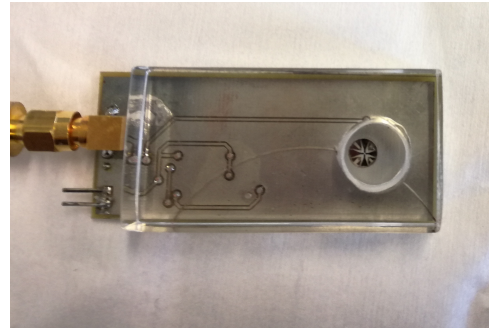
3.2.2.2 Manufacturing the PCB

The PCB design was manufactured by etching. The board material used was of type FR-4 PCB substrate. FR-4 is made of an epoxy fiberglass material and was chosen because of its isolation properties as well as for its strength. The FR-4 substrate used was double copper layered topped with a pretreated photo resist layer. The etching process to produce the final PCB was standard for photo-resist treated PCB boards. In short the procedure was done as follows:

- Printed the final PCB design produced in Cadstar, both layers (bottom and top) onto a transparency sheet and fitted both layers onto the pretreated photo-resist FR-4 substrate after it had been cut to selected dimensions (Removed the protecting film on the FR-4 substrate).
- The PCB with the fitted designed layout was then exposed to UV light for about 10 minutes.
- The PCB is then developed in 1-2 % NaOH (sodium hydroxide). This dissolved the exposed photo-resist leaving only the layout from the PCB design. Washed in water after.
- Then the PCB was put to the etching process done by immersing and washing the board in $FeCl_3$ (ferric chloride). The exposed copper was then etched away leaving the protected paths. Rinsed the board in water.
- Cleaned of the ink and remaining photo-resist with acetone. Rinsed in water
- The almost ready board was then tin-plated done by a three-step chemical process. The tin-plating ensured that the further process of assembling all components done by soldering more precise and delicate. The board was carefully sanded on all edges and all through holes was drilled out. The center of where the electrode chamber was to be mounted was also drilled out. To ensure that enough light from the microscope would be able to pass through the circular throughhole between the electrode pads was drilled by the UIOs mechanical workshop. This was done to ensure no damage to the PCB or any damage to the electrode pads.
- Rinsed the board for the last time in water and applied a flux-coating to further enhance the soldering process and protect the final PCB board.



((a)) PCB board top layer.



((b)) PCB bottom layers. The tin-plated surface is easier to view here.

Figure 3.8: PCB finished etched top and the bottom ground layer. ground

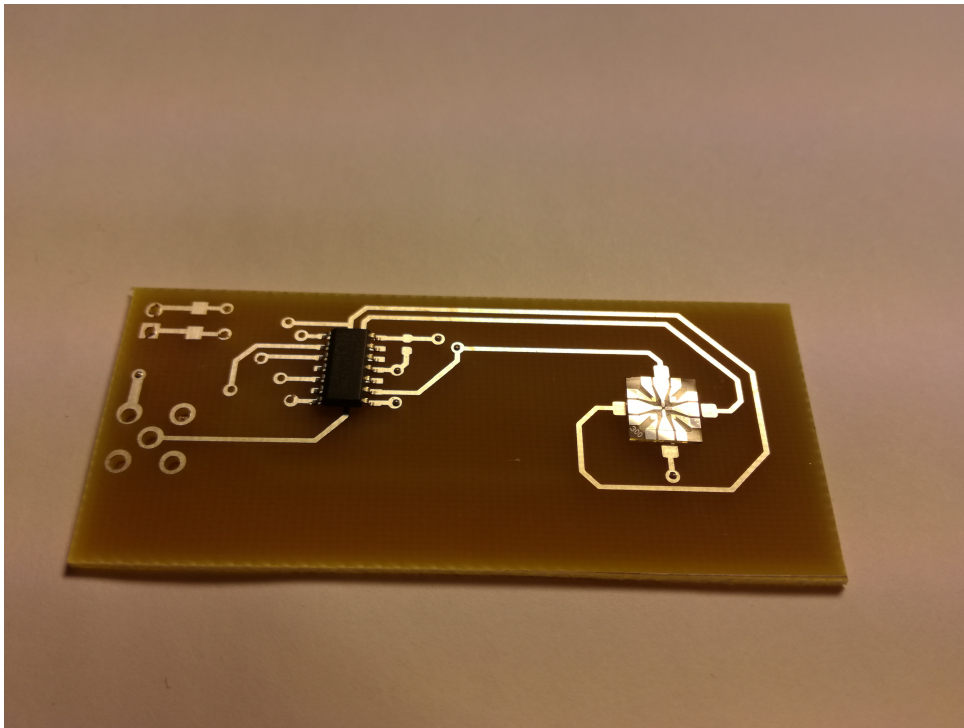


Figure 3.9: PCB top layer with fitted IC and electrode chamber at its respective placement.

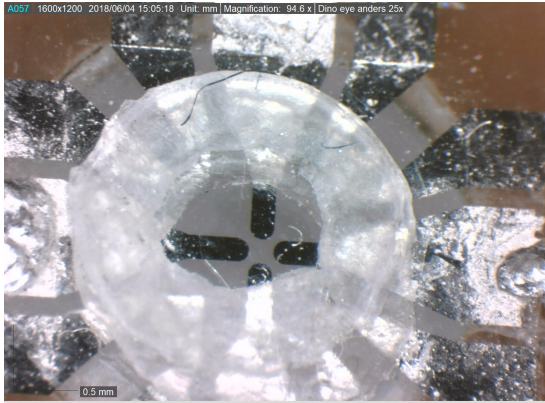
The components were mounted and soldered at the electronics laboratory at UIO. A Sub-Miniature version A connector (SMA) was used for the signal input connection on the circuit. The SMA connector chosen is a coaxial RF connector with standard $50\ \Omega$ impedance and used to optimize the signal input by reducing signal reflections between the signal generator and circuit signal input. A standard $50\ \Omega$ impedance SMA is designed to operate well above the MHz

region so this was more of a precaution than a real problem. A standard coaxial cable of $50\ \Omega$ impedance was used between the SMA connector of the signal generator (also $50\ \Omega$) and circuit to keep the impedance values equal. Signal and power line tracing on the PCB was chosen as to be of larger thickness as it would also reduce the impedance on the trace lines further reduce the risk of reflections. According to the low tracing density used to design the PCB, thicker transmission lines was easier to implement without routing traces to close together. This further reduced the risk of signal loss and noise.

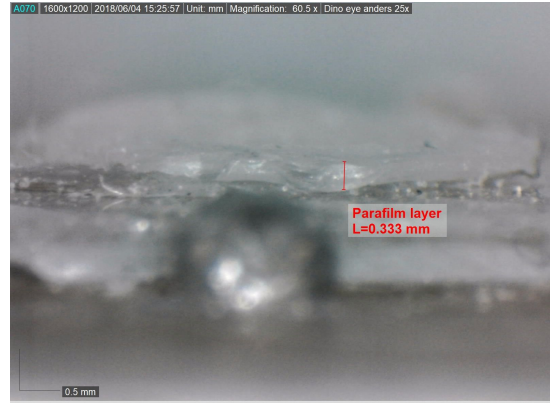
3.2.3 Extending the volume capacity of well in the electrode chamber

The volume capacity of the well of the electrode chamber was increased. This was done by utilizing parafilm which is used as a sealing film for laboratory purposes. The type used was called Parafilm M from the manufacturer Universal Medical and of approximately 0.2 mm thickness. Parafilm M is a semi-transparent, flexible, thermoplastic film with two-way stretch. It was colorless and moisture-proof and is non-toxic and free from plasticizers, primarily composed of polyolefins and paraffin waxes offering good resistance against acids, alkalies, and some organic solvents (Medical, 2018). From the parafilm miniature "rings" was made by using standard hollow metal cable clips. The desired dimensions of the rings was cut out of the parafilm using a small hammer (see figure. 3.10). The rings used was made of a dimension larger than the well, so it covered the whole well of the electrode chamber by a margin of ca. 2 mm. The radius of the electrode chamber's well (see section. 3.2.1) was 0.923 mm, so the outer radius of the rings made out of parafilm had dimensions of approximately 4 mm and the inner radius of 2 mm. Two rings were lightly pressured together giving a new thickness of approximately 0.3 mm. The resultant increase in the volume capacity of the electrode chamber was approximately thirteen times. (from $0.29\ \text{mm}^3$ to $3.77\ \text{mm}^3$).

To fasten the rings to the top-substrate of the electrode chamber hot air was used. Parafilm M becomes soft and adhesive at temperatures of $54 - 66^\circ\text{C}$ (Sigma, 2018). The rings were carefully placed to the wanted area and slowly heated. Some pressure was applied by tweezers to ensure that the now adhesive parafilm was attached properly.



((a)) Top-view of the parafilm ring attached.



((b)) Thickness of the parafilm rings attached to the electrode chamber.

Figure 3.10: The parafilm rings attached to the top substrate of the electrode chamber increasing the volume capacity of the well.

3.3 Preparation of yeast cell samples and storage

The testing cells chosen for this thesis was yeast cells. The yeast used was a dry bakers yeast from the manufacturer IDUN (blue type). Corresponding Data sheet is attached in the appendix (see Appendix C). More information was given by Emma Haglund working as process developer at Jästbolaget per mail (Haglund, 2017). Haglund informed that the yeast used in all of Iduns yeast product is of the stem *Saccharomyces cerevisiae* and for the dry yeast he cell concentration was given as approximately 2×10^{10} per 1 gram dry yeast. The primary difference from fresh yeast to dry yeast is its water content where Haglund informs that their dry yeast contains 5% water. Fresh yeast contains purely yeast while the dry yeast is supplemented with an emulgator (E491) due to help the the drying process. E491 is the substance Sorbitan monostearate (Pubchem, 2018) an is a non-polar substance but solvable in water. The nutritional value groups the used dry yeast listed in the data sheet (see AppendixC) e.g. salt, carbohydrates and fat. Haglund confirms that all nutritional values listed originates from the yeast it self and is not supplemented.

Preparation of the yeast emulsion/solution was done by solving the dry yest in sterile water. The sterile water used throughout this thesis was provided by the manufacturer B Braun. After the seal was broken, every bottle was discarded after each session of tests (kept maximum

twelve hours). This was done to reduce as much as possible the risk of contamination of the sterile water and minimize the exposure to air. Conductivity measurements was performed on the sterile water in the later stages of the thesis to test if the water exposed to air changed the conductivity levels. (see 4.3).

The information given by Haglund surrounding the population of cells per gram of dry yeast was not given as an exact number. The amount of dry yeast needed per emulsion made was of such small quantities that it was decided that it was easier to go through a process by dissolving a known amount of yeast into a known amount of sterile water to further dilute the emulsion until preferable cell count could be observed in the field of view of the microscope. The dry yeast comes in form of very small "pellets" (>1mm). Obtaining an emulsion with a cell count of 10 – 50 cells in the FOV approximately fifty pellets of dry yeast was solved in 3 ml of sterile water. Further the emulsion/solution was then diluted nine times over with sterile water. This concentration gave an emulsion where the yeast cells could be observed separately by more than three to four cell lengths in between. Different concentrations were tested. The prepared emulsion used under testing was kept no longer than two hours before it was remade. All test emulsions were made in 3 ml glass containers that were reused. The used containers and measuring syringes were all tediously washed first in ethanol then washed three times with the same sterile water from B Braun used for diluting.

The sterile water and the bakers yeast were stored away from sunlight and kept in room temperature. In the data sheet it was recommended to not use the yeast after three days prior to the seal on the packet was broken. As a precaution to reduce the risk of the dry yeast to be contaminated, each package of dry yeast was only kept for six hours before it was discarded. The dry yeast was properly sealed after each use within this six hours.

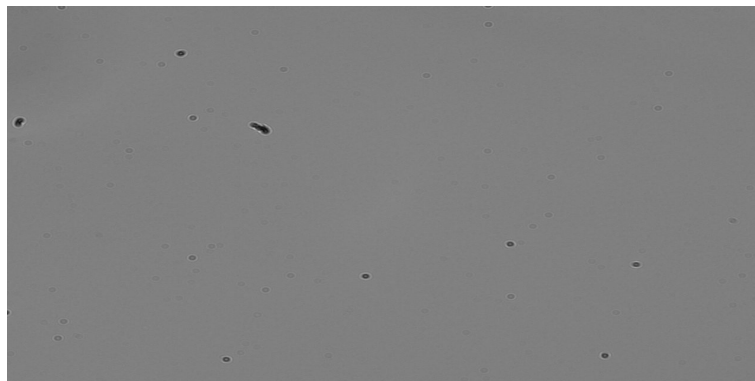
3.4 Cleaning routines for the electrode chamber

Before and after each sample was tested on the electrorotation circuit the electrode chamber needed to be cleaned thoroughly. Because of the small dimensions and risk of damaging the electrode or circuit a cleaning routine was developed. Special wipes and swabs manufactured for use in cleanroom laboratories was necessary to reduce particle and fiber release to keep the cleanliness level of the electrode chamber as optimal as possible. The wipes used was of two types, pre-wetted and dry. Swabs used had a conical tip. the swabs and wipes was manufactured by Texwipes (Texwipe, 2018).

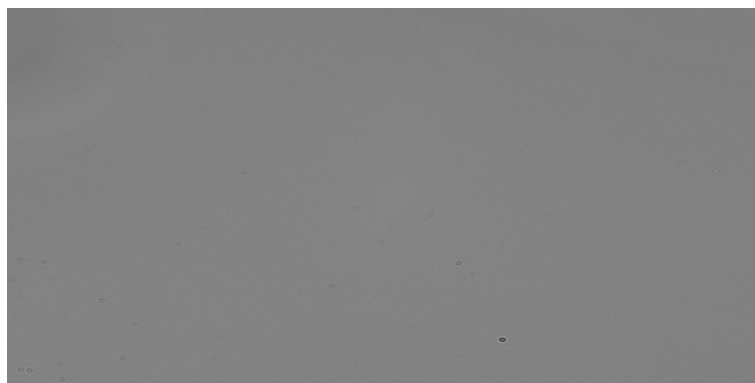
The cleaning routine was done at before the testing sessions started and at the end. Between each new sample was tested the routine also was applied:

- I Used dry wipes to absorb liquid residues.
- II Applied technical ethanol and let it sit for approximately one minute.
- III Used dry wipes to absorb liquid residues.
- IV Cleaned with pre-wetted wipes.
- V Used dry wipes to absorb liquid residues.
- VI Cleaned with swabs and sterile water.
- VII Used dry wipes to absorb liquid residues.
- VIII Cleaned with swabs and sterile water
- IX Used dry wipes to absorb liquid residues.
- X Cleaned with dry swabs.

The results obtained is illustrated in figure.(3.11) below showing the resemblance between cleaning without cleanroom certified wipes and swabs used in the developed routine.



((a)) Cleaned without cleanroom wipes and swabs.

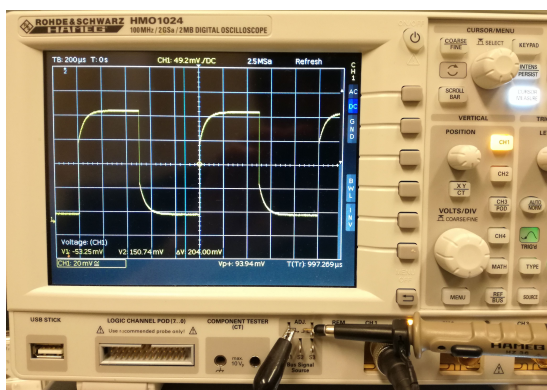


((b)) Cleaned by following all steps of the routine described above in this subsection.

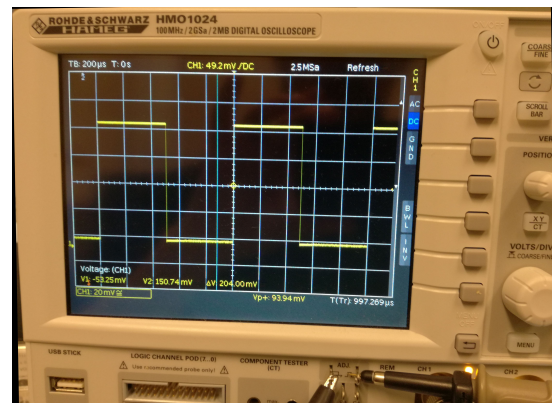
Figure 3.11: Illustrates the level of cleanliness obtained on the electrode chamber using certified cleanroom wipes and swabs

3.5 Calibration of oscilloscope probes

The oscilloscope probes used in this thesis was of model Hameg Hz 36 having a internal impedance of 1 mega ohms with an option to increase the impedance to 10 mega ohms. The probe is a passive voltage probe and suitable for measurement up to 100 MHz. The probe(s) was calibrated against the oscilloscope before every testing session as a routine. Most oscilloscopes have a 1 mega ohm impedance on its channel inputs and so did also the oscilloscope (HMO 1024 100MHz & Rohde and Schwarz) used throughout the testing phase of this thesis. The Oscilloscope has an input capacitance and to compensate for this the probe has an adjustable capacitor connected in parallel. By adjusting this the correct capacitance potential divider ratio between probe and scope was obtained. This was done by testing the probe on the oscilloscopes internal square wave generator by tweaking the adjustable capacitor on the probe until a perfect square wave is obtained (Ltd., 2018) (see figure.3.12).



((a)) Before calibration.



((b)) After calibration.

Figure 3.12: Calibration of the probe after the internal square wave generator on the oscilloscope.

The HMO 1024 100MHz Rohde and Schwarz Oscilloscope had no calibration settings for the oscilloscope itself. User manual provides no information on this other than probe calibrations. However, the oscilloscope was tested for different voltage levels using a multimeter as reference measurement showing correct values. Frequency tests was also performed on the oscilloscope that gave equal test values represented by the signal generator used to perform the test (HMF 2550 & Rohde and Schwarz).

3.6 The microscope setup

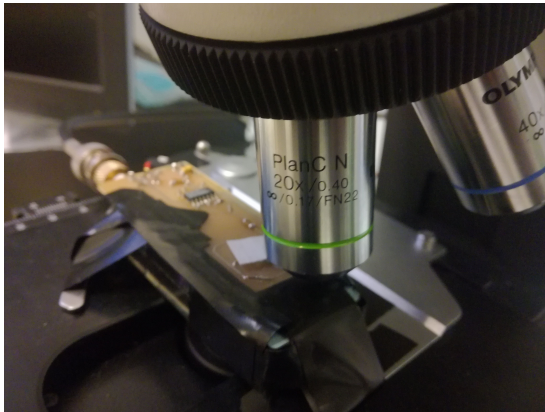
3.6.1 Microscope calibration and setup

The microscope used in this thesis was a Olympus CX41 with a 6 V 30 W halogen light source. The Olympus CX41 is an upright microscope meaning the light source is placed underneath the sample. Every time the optical microscope was taken into use it was set up for Köhler illumination (section E). This was done to provide optimized resolution and contrast. The technique is imperative to bright field optical microscopy. As described in section E obtaining Köhler illumination is done by aligning and focusing the light from the condensers illumination light path. The technique and even more important setting the iris apertures of the microscope to match the objective lens as best possible. A five step procedure was always followed after an guide given by Scientifica (Scientifica, n.d.):

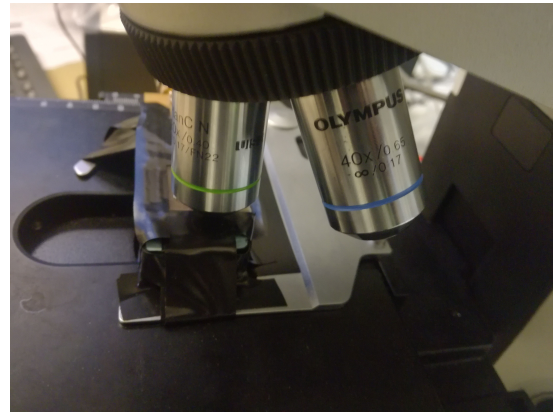
1. The ER circuit was put in position and locked to the slide holder of the microscope. The objective with the least magnification was selected (20x). The microscope was focused onto the tip of one of the electrodes in the center of the chamber and the condenser was brought to its top elevated setting /position.
2. The field iris diaphragm on the condenser was the closed to its minimum. If the darkening circle in the FOV did not appear or was not centered the condenser had to be aligned back to center.
3. The condenser is the lowered from its elevated position until the edges of the dark outer and the illuminating area in center becomes a sharp edge.
4. Then the condensers diaphragm is open until the black edges is just outside the FOV.
5. Then the aperture iris was set so that it occupies ca. 20 percent of the the outer of the field of view. This was done by removing one of the eye-pieces and looking down the observation tube. This step was performed very careful because closing the aperture iris to much will lead to loss of resolution (see section 2.2.4).

This procedure was always performed when switching objective. In this thesis only a 20x(magnification scale) objective and 40x objective was used. Both objectives was produced by Olympus. the 20x is plan corrected, having a numerical aperture (see section.2.2.3.2) value

of 0,40 and designed for cover slip thickness of 0,17 mm. The 40x objective had a numerical aperture of 0,65 and was also designed for cover slip thickness of 0,17 mm. Cover slip thickness used throughout this thesis was chosen after the objectives numerical aperture to obtain an optimal image.



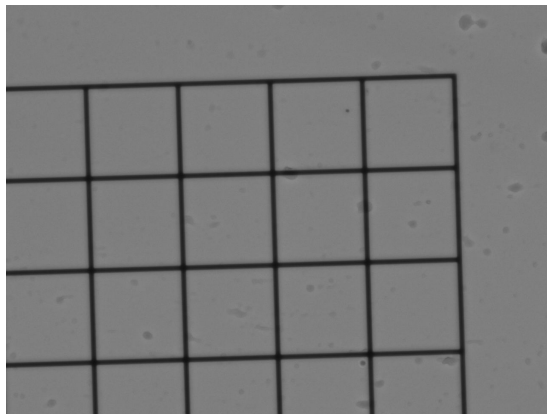
((a)) 20x objective



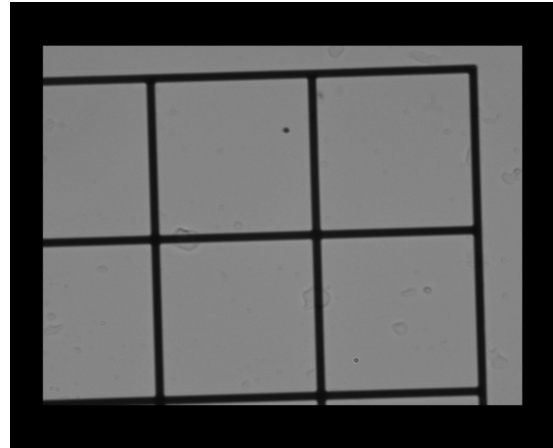
((b)) 40x objective

Figure 3.13: The microscope objectives used in this thesis. The FN value given on the 20x stands for field number and is related to the FOV looking through the eyepiece ($FOV = \frac{FN}{Objectivemagnification}$).

To estimate the microscopes ability to resolve objects dimensions at different magnifications a calibration set from Max Levy Autograph. INC was used. This calibration tool was mainly used to confirm that the acquired microscope setup would resolve yeast cells used in this thesis. *Saccharomyces cerevisiae* was the planed testing cell and dimensions vary from the various stems of the yeast type from 3-10 μm . In the research of Yamaguchi et al.(Yamaguchi et al., 2011) on the whole structural dimension of *Saccharomyces cerevisiae* the used dimension for the major axis given as 3,85 μm with a standard deviation of 0,42 μm . The calibration setup was then performed on a calibration figure featuring a routed network with line width of 2,5 microns and spacing of 50 microns (see figure.)



((a)) 20x magnification - 50 micron spacing - 2.5 micron line width



((b)) 40x magnification - 50 micron spacing - 2.5 micron line width

Figure 3.14: Calibration slides tested to ensure the yeast cells would be resolvable of the microscope setup.

Objective lens and condenser glass was cleaned with objective lens paper before each testing session. The lens paper is lint-less and prepared for cleaning highly polished glass surfaces.

3.6.2 Resolution limitation calculations of the camera needed

In section 2.2.4.4 the dimensions of pixel sizes needed to match the optical resolution given by the microscope system is explained. In this thesis the camera available was DMK 41BU02.H from ImagingSource. The camera was equipped with a half inch monochrome CCD sensor from Sony that has a 1280 x 960 pixel array (8-bit). The camera could record up to 15 fps. The CCD sensors pixel size had a horizontal and vertical dimension of $4.65\ \mu\text{m}$. Pre calculations to what limitations of resolution that was possible to obtain was done as described in section 2.2.4.4 illustrated in table. 3.2. The calculation showed that with the 20x and 40x objectives planned to use for the microscope system would clearly match the Rayleigh resolution converted to the camera plane. The camera used had pixel size of $4.65\ \mu\text{m}$ and would suffice. These calculation was fundamental to ensure the microscope system would suffice to make recordings for the rotation of yeast cell observation in a resolution of good enough quality to distinguish the cells properly.

3.7 Conductivity measurements of sterile water against two different populations of yeast emulsions

Matching camera resolution to optical resolution (μm)				
Wavelength	Magn.	Rayleigh Res.	Camera plane	Min pixel size (Nyquist)
550 nm (Average)	20	0,84	16,8	8,4
	40	0,52	20,6	10,3
500 nm (Green)	20	0,76	15,3	7,6
	40	0,47	18,8	9,4
600 nm (Red)	20	0,92	18,3	9,2
	40	0,56	22,5	11,3

Table 3.2: This table shows where the Rayleigh resolution is calculated for the given microscope setup in this thesis. The column marked camera plane is a conversion from the optical resolution of the microscope to the camera plane. The minimum pixel size needed to match the optical resolution is shown in the last column. The wavelengths used is the average wavelength of halogen light, green wavelength and red light, respectively.

3.7 Conductivity measurements of sterile water against two different populations of yeast emulsions

The conductivity measurements were done at the Pharmaceutical institute of UIO. The measurements were conducted after the prior electrorotation test phase of the yeast emulsions. The same population for the yeast cell emulsion used under electrorotation test was copied for the conductivity measurements. The volume of the emulsion needed to be increased twenty five times to acquire enough emulsion for the conductivity sensor to be submerged sufficiently. The conductivity meter used was model EL3 Conductivity Meter with sensor LE703 from the manufacturer Mettler Toledo.

The 3 ml yeast emulsions prepared in the testing phase needed to be multiplied twenty five times (see section. 3.3). Yeast pellets of the same count was measured with an analytic balance weight of model AE 260 Delta Range from manufacturer Mettler. Four different samples were prepared and weighted. The mean value of these samples was calculated (4.2mg) and multiplied twenty five times (0.105g). The yeast was then solved in 75 ml of sterile water from B Braun and the emulsion used in the test phase was replicated. The yeast emulsion was then diluted with sterile water into two new emulsions with a relation of 1/5 and 1/3 of the original concentration. Sterile water and the two emulsions were then consecutively measured every fifth minute of a total time span of eighty minutes. To ensure homogeneous measurements the emulsion was stirred before each measurement due to sedimentation. The conductivity sensor was washed in sterile water and dried between each measurement. All measurements were performed at a

steady 23°C for all emulsions throughout the time span.

3.8 Anomalies concerning signal output characteristics

A range of measurements for the output signal characteristics was performed for various relation of selected Vcc and signal magnitudes. The frequency range that was used for these measurements spanned from 0 Hz to 50 MHz where signal input/output was measured simultaneously (see section. 4.4 for measurement results). Similar measurements was previously initiated on completion of the electrorotation device. This was done to confirm the system performance was precise (see section. 3.2.2.1). The reason to why these new tests were performed was due to an sudden discovery of an unexpected effect. In the middle of a testing session the circuit seemed to perform normally. It was then noticed that the system was running without any supply voltage connected to the Vcc terminals on the IC. The power supply was disconnected. The data sheet clearly the IC (Philips, 2003) declares a minimum of 2V Vcc and the schematics and design was deemed correct leaving only the IC as the most plausible source for the abnormal and unexpected observation. Further explanations and the implications it had is presented in the discussion (see section. 5.1.4). The measurements was needed to gain an overview and clear understanding of how the system performed under different settings for Vcc and signal input magnitudes.

3.9 Counting cell rotations

After a successful test session was performed the rotation rate for cells needed to be counted. Most test series that was performed was series of twenty-seven recordings for each selected frequency. Before a test session was deemed successful all recordings for each frequency was monitored to ensure that the same cell kept close to the center of the electro chamber for the whole recording session. It was also monitored for that as little as possible or preferably no cell-to-cell interaction occurred. Each recording session that was performed ranged from five to nine seconds. The most optimal cell(s) was singled out and the rotation rate was calculated by visual observation.

The rotation rate measurements was done by visually observing the cell frame by frame. VLC media player was used for this task. The video sequences recorded was set to the highest

frame rate possible which was 15 frames per second for the camera used in the test (DMK 41BU02 - ImagingSource). Visually observing the recordings frame by frame made it possible to easier and more accurate calculate the full rotations and also accurately measure the not fully completed last revolutions the cell had not complete before the recording ended. The cells singled out for measurement was always of larger size. The size of the yeast cells observed varied from small egg-shaped cells to the larger cells which was preferred for the measurements. The larger cells was singled out for two reasons. They were easier to observe and they were more circular shaped. A erasable marker was used to mark the start and end angle and position of the cell. In that way it was possible to count all full rotations and measure the angle of the not completed last rotation. The rotation rate was then calculated from the measurements of the recording and used to plot the different electrorotation spectra (see equation.4.2.1).

Results

4.1 Introduction

In this chapter all of measurable and acquired data gathered through this thesis is presented. The data presented is directly related and decisive for the interpretation of the results of this thesis. Data that indirectly still is relevant but had no influence on interpretation or is conclusive to the results is presented in the appendix.

This section contains the hearth of this thesis which is the electrorotation spectra based on measurement performed on yeast cells manipulated by electrorotation. The chapter also contain conductivity measurements and a profound measurement regarding different signal input/output measurements. All calculations, interpretations and explanations regarding the data of this chapter will be presented in the discussion chapter.

4.2 Electrorotation spectrum's for *Saccharomyces cerevisiae*

In this section, the results from completed electrorotation specters are presented. The word completed implies the spectra presented is complete in the form that all measurements have been done for all frequencies measured without any discontinuities.

All input voltages declared are peak-to-peak values. Given, e.g., a 5 V input signal will denote an amplitude of 2.5 V. This notation is used throughout the thesis. A 50 % offset was always applied to the generated signal to keep the square wave signal pulse. A threshold of 0 V

is declared in the data sheet for the IC (Philips, 2003).

Incomplete and discarded testing sessions are not presented in the results. In appendix D an overview of all relevant test sessions performed in this thesis is presented. The overview declares which test session that deemed successful or discarded. All test sessions in this thesis have kept its original index/name as the test sessions are indexed/named in the file structure of the raw data. The original indexes were kept on purpose to ensure the correct recordings presented as data in this thesis can be recollected from the raw data.

The following electroration spectrum's (ROT) from figure. 4.1 to 4.5 that follows was recorded with an amplitude of 4 V for Vcc and a 4 V peak-to-peak input signal with 50 % offset. The frequency range spans from 2 KHz up to 50 Mhz. The ROT spectra are measured from of dry baker yeast cells in sterile water (see section. 3.3). R1 marked at the first characteristic frequency is the rotation peak of the spectrum measured. Negative values indicate anti-field rotation and positive values co-field rotation. The fitted curve is Lorentzian. The cell counts in the FOV recorded varied from less than 20 to almost 100 cells. The ROT values were calculated from:

$$ROT = \frac{2\pi}{E^2 * T} \quad (4.2.1)$$

where the E and T are denotations for the external field strength and the time for one revolution, respectively. The ROT values have been scaled for illustrative causes. When the curves cross the x-axis, it indicated no rotation.

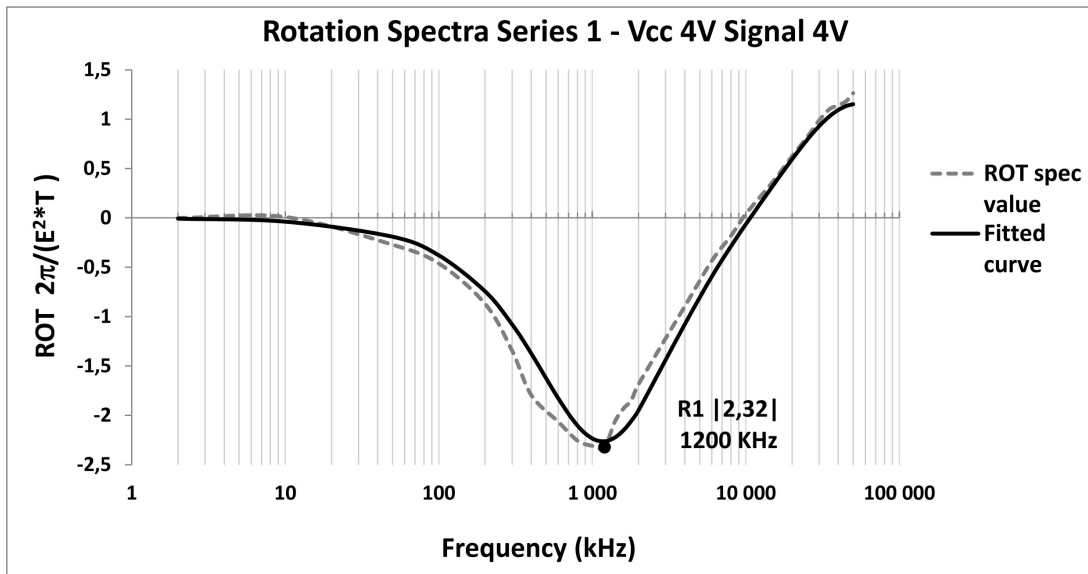


Figure 4.1: Complete series for all frequencies measured for one single cell without any interaction from other cells. Series 1 was measured within the FOV with cell count < 20.

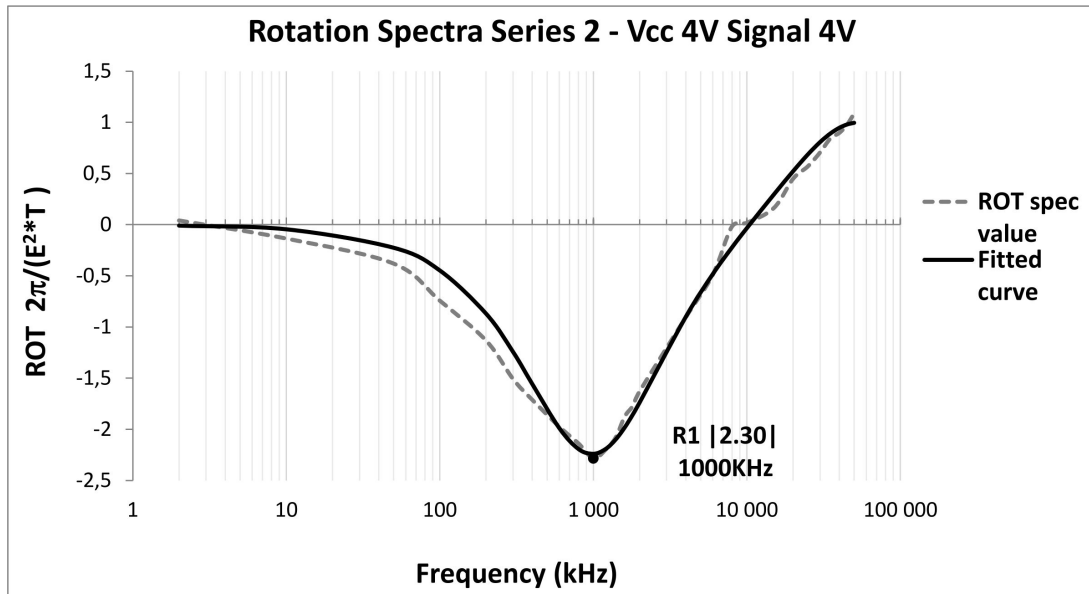


Figure 4.2: Complete series for all frequencies measured for one single cell without any interaction from other cells. Series 2 was measured within the FOV with cell count $\gg 20$. The Cell that was measured was ca. 80 percent of the size of most other cells.

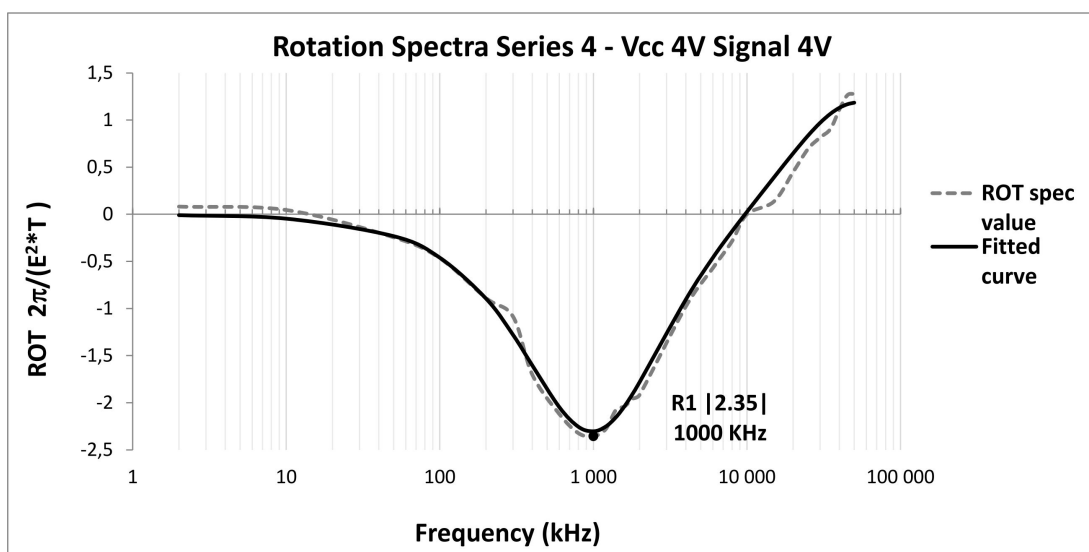


Figure 4.3: Complete series for all frequencies measured for one single cell without any interaction from other cells. Series 4 was measured within the FOV with cell count < 20 .

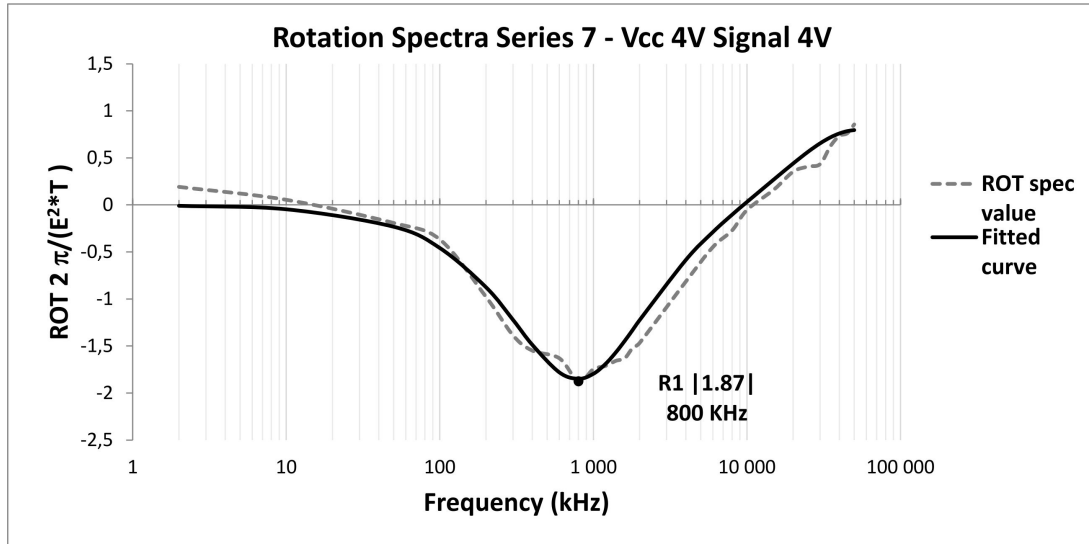


Figure 4.4: Complete series for all frequencies measured for one single cell with cell-to-cell interaction. Series 7 was measured within the FOV with cell count $\ll 20$. This spectrum differs from all other spectrum presented due to cell-to-cell interaction throughout all frequencies.

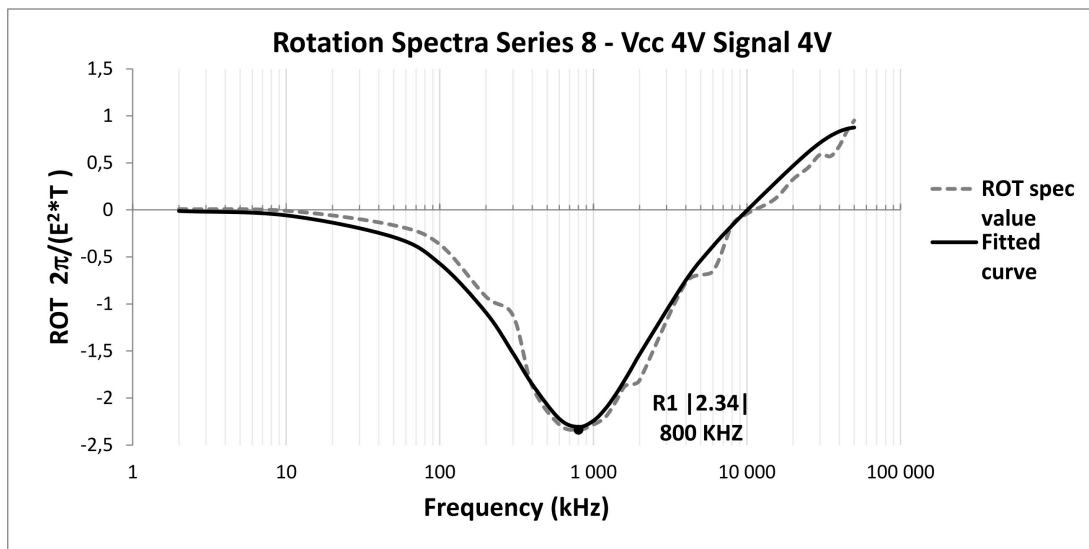


Figure 4.5: Complete series for all frequencies measured for one single cell without any interaction from other cells. Series 8 was measured within the FOV with cell count < 20 .

The next following electrorotation spectrum's (ROT) from figure. 4.6 to 4.9 that follows was recorded with an amplitude of 5 V for Vcc and a 5 V peak-to-peak input signal with 50 % offset. The frequency range spans from 2 KHz up to 50 Mhz. The ROT spectra are measured from of dry baker yeast cells in sterile water (see section. 3.3). R1 marked at the first characteristic frequency is the rotation peak of the spectrum measured. Negative values indicate anti-field rotation and positive values co-field rotation. The fitted curve is Lorentzian. The cell counts in

the FOV recorded varied from less than 20 to almost 100 cells. The increased field amplitude in the following spectrum's leads to faster rotation rates but also gave rise for the DEP forces to become more evident. The cells were moving out of the center of the electrode chamber either started to migrate to areas of lower or higher field densities. The cells are far from isotropic or homogeneous, so this was an expected effect as DEP forces scale with field amplitude.

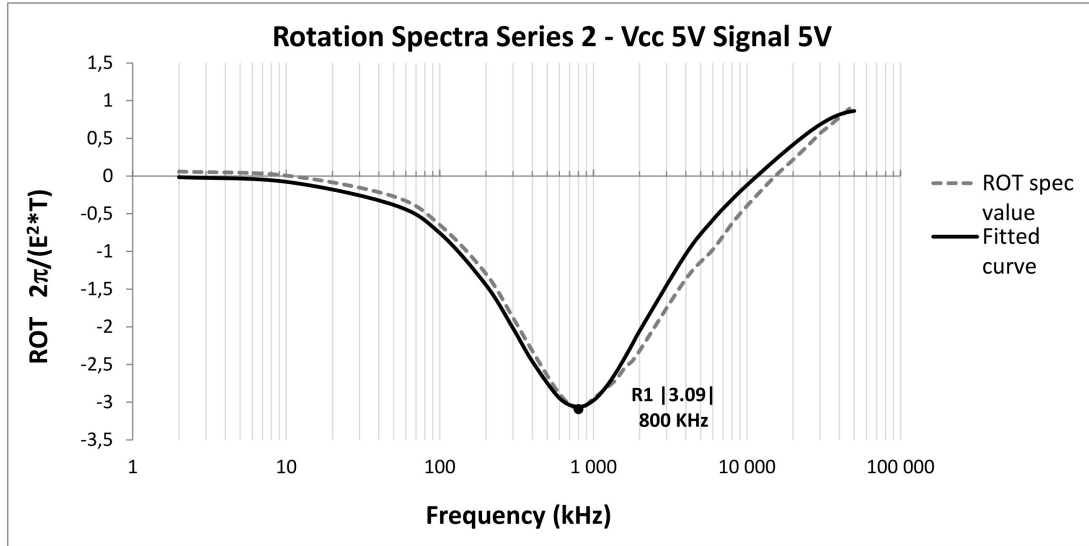


Figure 4.6: Complete series for all frequencies measured for one single cell without any interaction from other cells. Series 2 was measured within the FOV with cell count < 20.

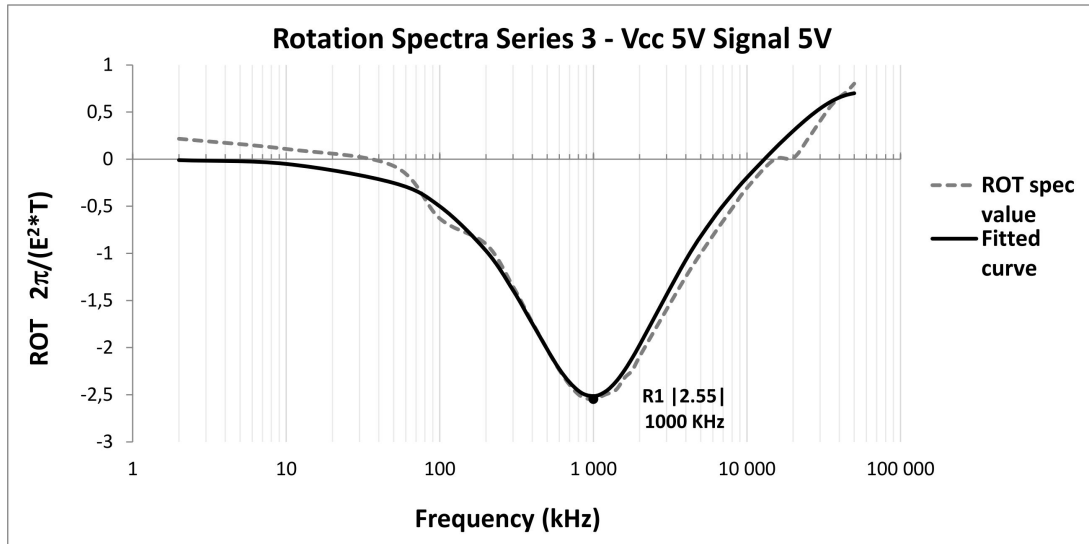


Figure 4.7: Complete series for all frequencies measured for one single cell without any interaction from other cells. Cell measured was of slightly more elliptical shape. Series 3 was measured within the FOV with cell count > 20.

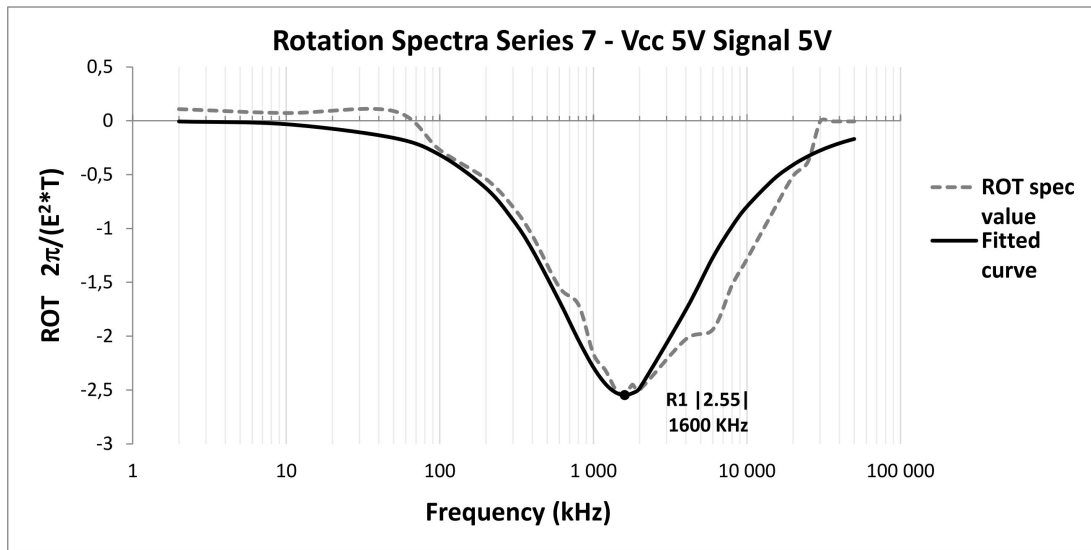


Figure 4.8: Complete series for all frequencies measured for one single cell without any interaction from other cells. Series 7 was measured within the FOV with cell count $\gg 20$. This series showed no positive ROT values and ergo no co-field rotation in the higher frequency range.

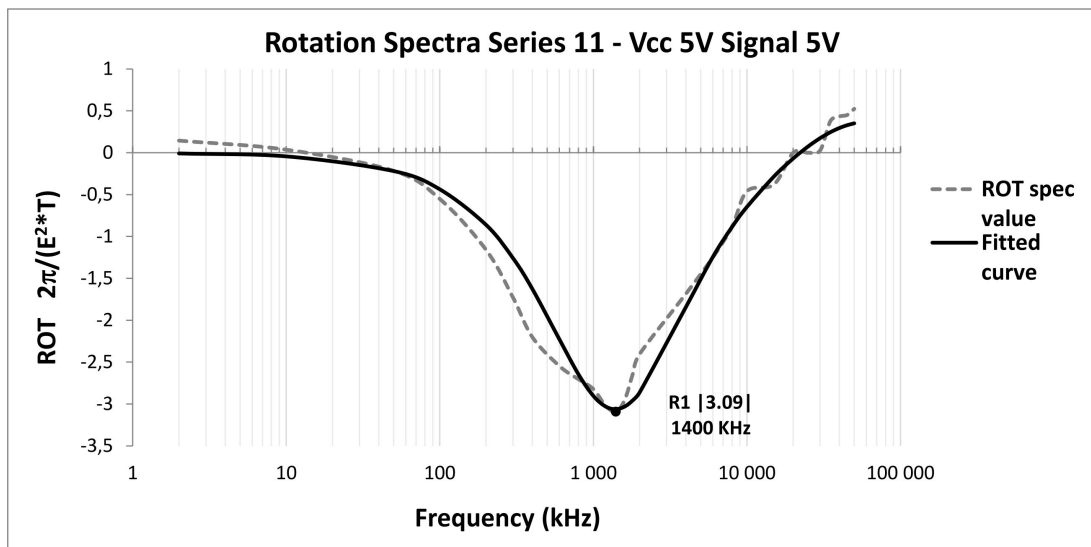


Figure 4.9: Complete series for all frequencies measured for one single cell with brief cell to cell interaction between 10 to 30 MHz. Series 11 was measured within the FOV with cell count $\gg 20$.

4.3 Conductivity measurements

Table 4.1: Conductivity measurements for sterile water and yeast cell emulsion over time. Min, 1/5 emulsion, and 1/3 emulsion are abbreviations for minutes, one fifth and one-third dilution of the start emulsion with sterile water (see section.3.7). The values are graphically illustrated in figure.4.10.

Conductivity measurement ($\mu\text{S}/\text{cm}$)							
Min	Sterile water	1/5 emulsion	1/3 emulsion	Min	Sterile water	1/5 emulsion	1/3 emulsion
0	1,0	5,6	9,3	45	1,3	6,9	11,5
5	1,0	6,1	10,3	50	1,4	7,2	12,2
10	1,0	6,4	10,5	55	1,5	6,9	11,4
15	1,0	6,4	10,2	60	1,5	7,1	11,8
20	1,0	6,4	10,2	65	1,5	7,1	11,4
25	1,1	6,7	10,6	70	1,6	7,1	11,6
30	1,2	6,6	11,1	75	1,7	7,1	11,7
35	1,2	6,8	11,0	80	1,6	7,3	11,8
40	1,3	6,8	11,3				

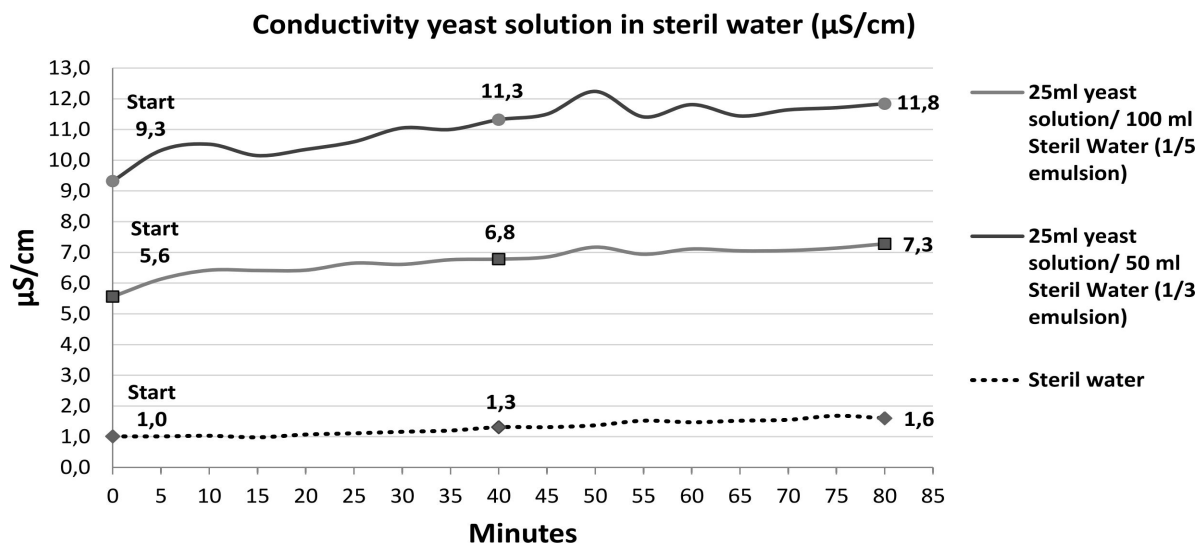
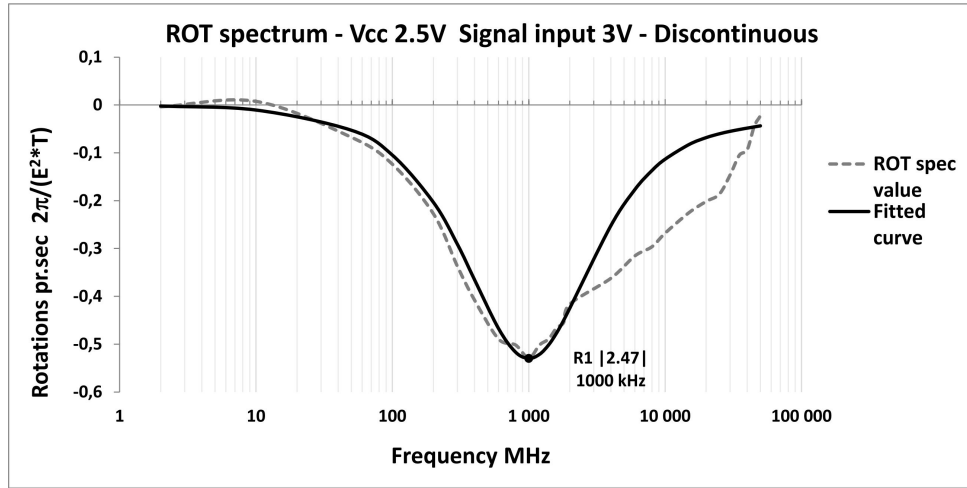


Figure 4.10: The figure illustrates a rise in conductivity levels over time. The undiluted start emulsion was measured to be 22 $\mu\text{S}/\text{cm}$.

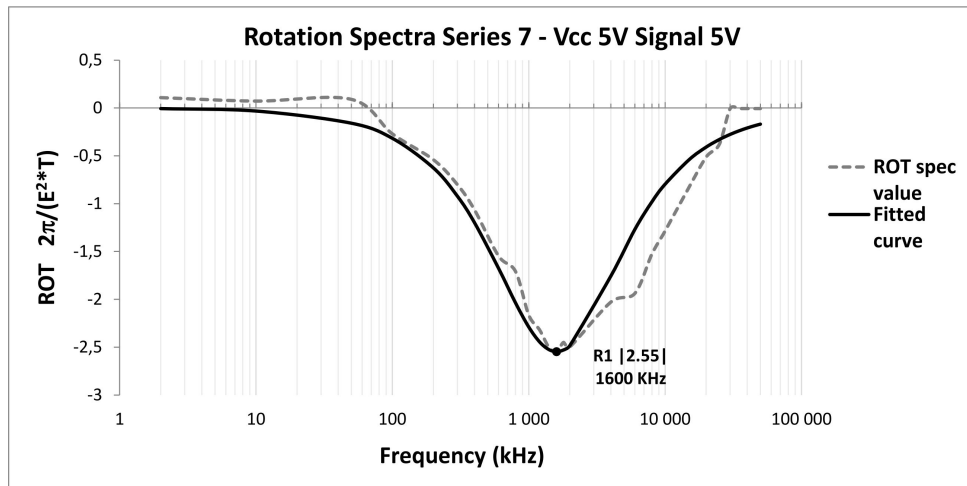
Figure. 4.10 above illustrated a modest conductivity increase in the sterile water and the two different emulsions. The most significant rise per percent is the sterile water increasing 60 % while the 1/5 and 1/3 diluted emulsions increases 30 % and 27 % respectively. However, the conductivity levels have risen 0.6 $\mu\text{S}/\text{cm}$ for the sterile water, and 1.7 $\mu\text{S}/\text{cm}$ and 2.5 $\mu\text{S}/\text{cm}$ for the 1/5 and 1/3 diluted emulsions stating the most evident rise in conductivity is for the highest populated emulsion.

4.4 Relation measurements between signal input magnitudes and supply voltage (V_{cc})

In section. 3.8 the explanation to why and how a range of measurements for the output signal characteristics was performed. The measurements were initiated to get an overview of how output potential and output frequency correlated to the selected input parameters. The observation that the IC still functioned even without any supply voltage connected showed that the measurements were needed. As the irregularities in the signal output were detected, it was apparent to put all previous observations and tests under scrutiny until a better understanding of what parameters the output signal had under different settings. To gain some indication for which parameters to test for real-time visual observation was used to monitor the electrorotation effects on bakers yeast for different settings of input magnitudes tested for the frequency range used previously (2kHz to 50 MHz). Different observations were obtained that indicated a significant decrease in frequency or field amplitude for V_{cc} and input signal settings lower than 3 volts. As an example, one of these indications was given when the supply voltage was set to 0V. Similar cell behavior was observed at higher frequencies ($>1\text{MHz}$) as in the lower regions (0-2KHz). The yeast cells have shown a tendency to migrate to the electrodes in the lower frequency region and at the same time displaying short radial centripetal oscillations for the yeast cells situated closer to the center of the electrode chamber giving a clear indication of deviation from previously similar performed electrorotation experiments on bakers yeast. The new more extensive measurements for input/output signal parameters confirmed that the indicated deviations were real. Not only for V_{cc} values that were declared under the threshold given in the datasheet but also for values declared plainly within the recommended range for the IC. Visual observations alone was not enough to reveal and distinguish the sudden decrease in the output signal. The obtained discontinuous electrorotation spectra followed the same pattern found through previous testing sessions and were highly misleading. In figure. 4.11 it is illustrated how similar the discontinuous and continuous spectrum's are.



((a)) The discontinuous spectrum above illustrates similar patterns to that of contentious. By visual observation and as the spectrum illustrates, the rotation rate seems normal up to the first characteristic rotation peak R1. After rotation peak R1 the rotation rate is expected to decrease between the transition from the first to the second dispersion. The spectrum follows the same pattern, but the observed decrease in rotation rate is caused by an exponential decrease in the field magnitude as well as frequency. Not the transition from the membrane dispersion to the bulk dispersion in a continuous spectrum.



((b)) This spectrum is contentious throughout the whole frequency range. In section. 2.1.2.8 is elaborated and in this case the dipole moment of the cell never changes sign because of increased conductivity of the external medium to a higher value than the conductivity of the cell.

Figure 4.11: Similarities in a discontinuous and contentious ROT spectrum.

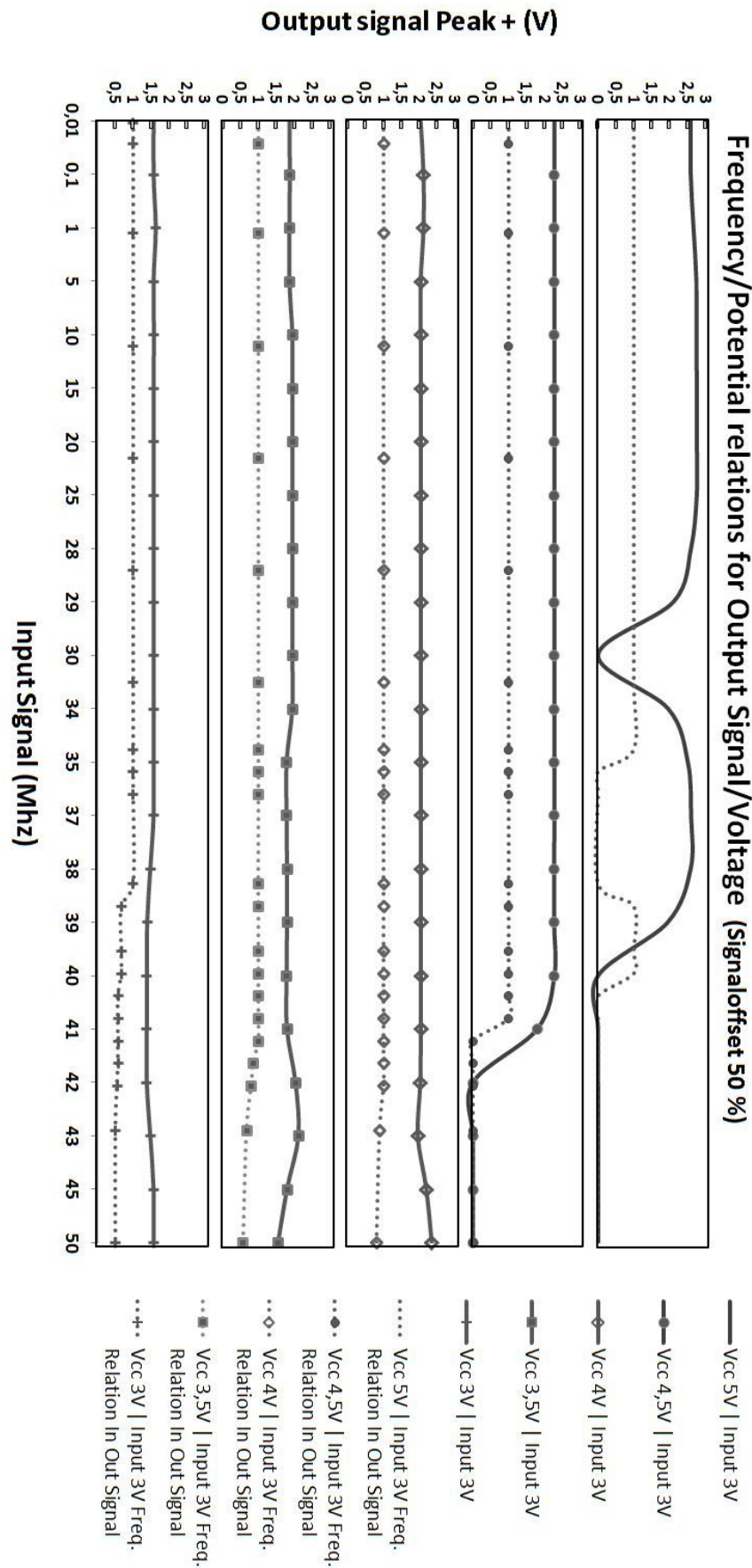


Figure 4.12: Differences in the output signal related to magnitude setting for the supply voltage and signal input.

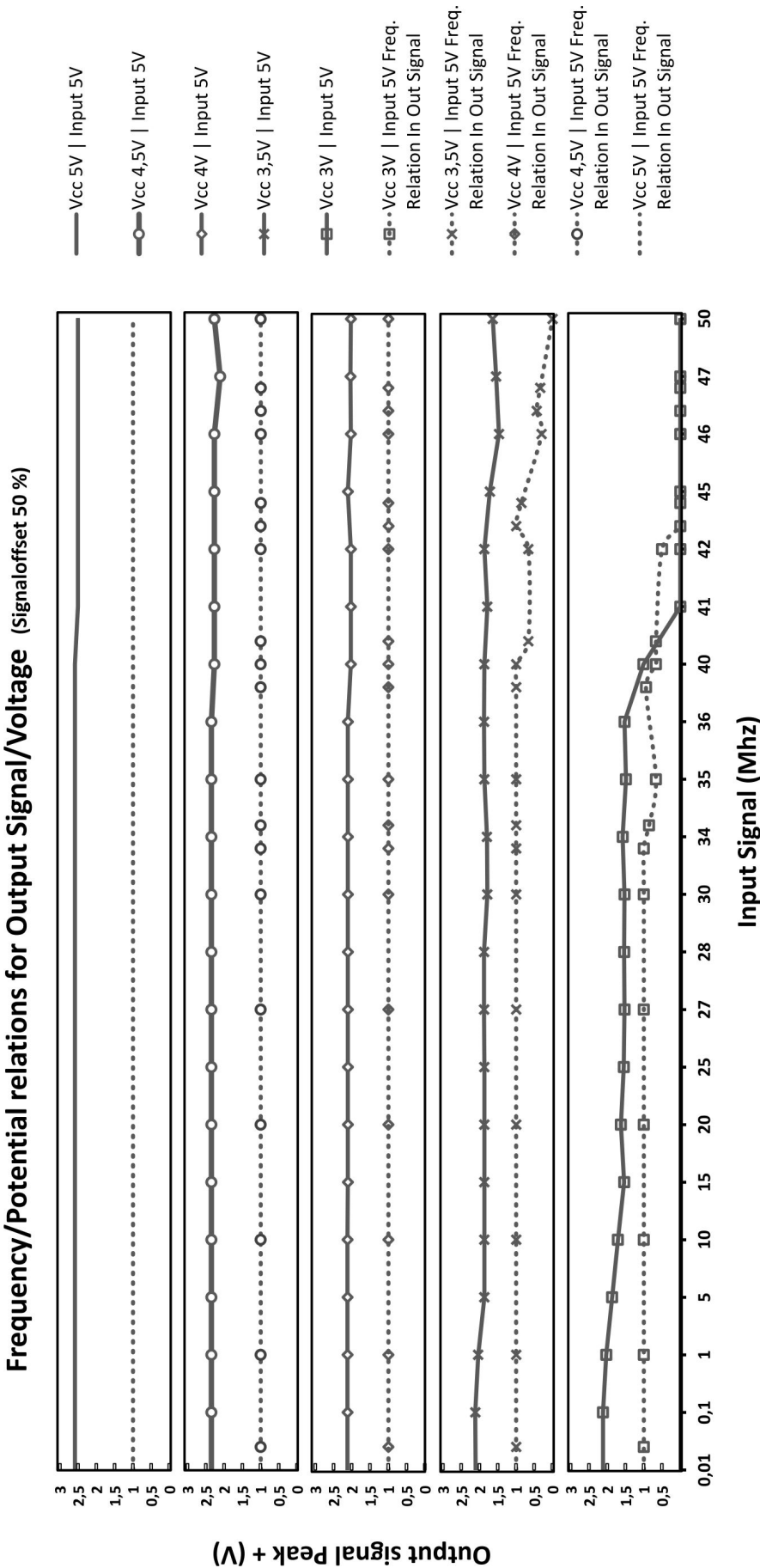


Figure 4.13: Differences in the output signal related to magnitude setting for the supply voltage and signal input.

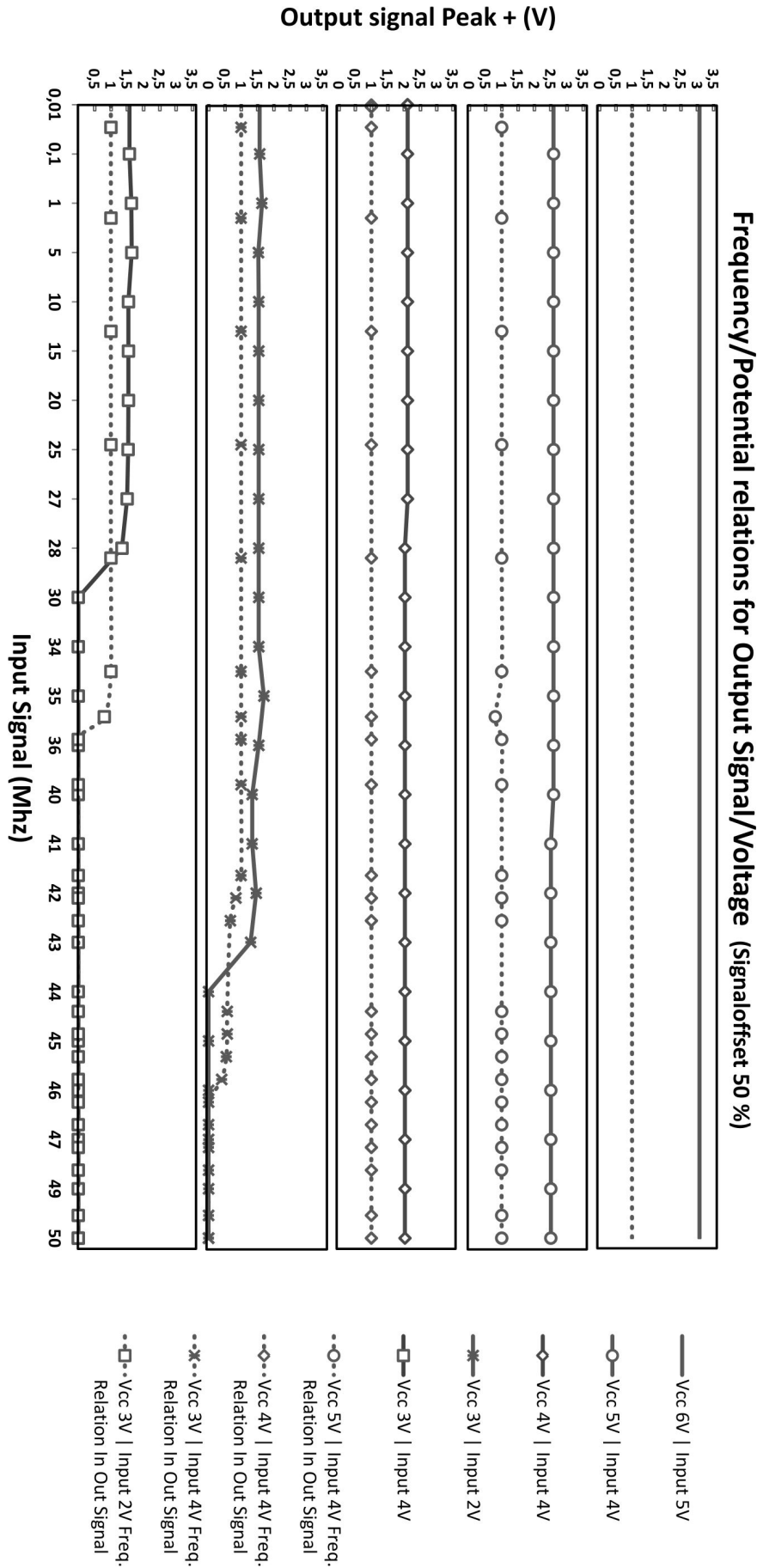


Figure 4.14: Differences in the output signal related to magnitude setting for the supply voltage and signal input.

Discussion

This chapter presents a discussion encircling the multiple electrorotation spectra obtained from the measurement results. These spectra were obtained by manipulating yeast cells by the electrokinetic effect electrorotation. All experiences gained, obstacles met, what could have been done differently, and the implications it meant for the result of this thesis is analyzed in this chapter.

The primary goal of the thesis was to investigate the concept and establish a fundamental understanding of electrorotation as a technique to manipulate objects for analytical purposes. Electrorotation has not been studied or investigated before at the University of Oslo, so a profound background study of the fundamental theory and past research was needed before the concept could put to the test. Followingly, the thesis in its wholeness has been a scientific feasibility study approach as a learning-by-doing process from start to end.

5.1 A broad analysis of the system setup

In this section will every critical element needed to create the system with capabilities to perform electrorotation measurements be discussed. All aspects discussed in this section played its part in making ER measurements possible. Without each element, the measurements would not be possible to perform, or the quality of the result would be degraded. The section discusses all from correctly handling sterile water, how a strip of parafilm was decisive for the whole project to the art of using microscopy.

5.1.1 Ensuring the accuracy of the results and the reproducibility

The number of successful test series in this research project was limited. It proved difficult to get a complete frequency range recorded without cells interacted with each other or deviated out of the center of the electrode chamber. Each test session was relatively fast to record where each recording only lasted from five to eight seconds of a total of twenty-seven recordings per session (approximately 2-5 minutes per session). The time-consuming part was the preparations before and after each session where cleaning the electrode chamber after each session was by far the biggest time consumer. In section.3.4 the cleaning routine developed was followed after each session and was tedious work. Most started test sessions was aborted due to cell migration or cell-to-cell interaction as the session was monitored over the microscope's live-feed and the electrode chamber needed to be cleaned. The cleaning routine was developed to ensure as similar initial conditions as possible for each new session started.

All tests were performed in a non-laboratory facility which was far from ideal as it proved difficult to reproduce a controlled environment. However, all parameters that were possible to control was systematized and put into routines concerning mainly the yeast samples, the sterile water and the cleanliness of the electrode chamber and all tools used to prepare the samples. (See section.3.4 and 3.3). The room temperature was fairly stable as most measurements were done when no other persons used the same facilities. The temperature was fairly stable at 22-23°C for every test session performed. All medium used was stored at the same temperature. The air quality also proved to be a challenge as impurities as dust and particles were multiple times discovered in the emulsions prepared for testing.

All in all the test sessions was time-consuming and tedious, but as the test period progressed over time, all routines that were developed was improved, and the reproducibility and initial conditions resulted in a better success rate for complete sessions. The more scientifically challenges discovered was ensuring more or less the same cell count for each prepared emulsion and the implications yeast cell have on the conductivity of the suspending medium. This is discussed in more detail in section. 5.1.3. All conclusions drawn from the results of the experiments are made on the basis that multiple variables influenced the system, controllable and uncontrollable, but much effort was made to isolate as many variables as possible to ensure better accuracy and reproducibility. Other obstacles of was discovered through the process that had a much more critical impact on the measurements, e.g., evaporation, unwanted electrolytic effects, abnormal

analog circuit behavior, resolution restrictions and so forth. All of these obstacles is explained in more detail in their respective sections of the discussion.

5.1.2 Choosing the system setup for the specific task

In retrospect of the whole process leading up to when all measurements and testing were performed, the experience learned is that the system setup (electrode chamber and microscope) must be accurately designed and chosen according to the specific size of the object planned to be characterized by electrorotation. Biological cells and spheroidal particles differ significantly in dimensions and volume. Where one system setup will be perfect for a yeast cell of $5\mu\text{m}$, it will be non-functional for a cell three times larger. In this thesis, it was proved to be a decisive factor in the success rate for the acquired data during measurements both for the electrode chamber as well for the microscope system used. Both electrode chamber and microscope has finite limitations underlining that careful planning for the system setup is imperative. In the next subsections, the microscope system used in this thesis and the electrode chamber will be discussed in more detail focusing on the implication of the limitations the system setup had for the measurements.

5.1.2.1 Suitability of the microscope system

In this thesis using a microscope was essential as all observations of measurements are done visually. An optical microscope was used throughout the testing sessions. In optical microscopy, light is the decisive factor for all aspects of resolution and limitations. Setting the microscope to Köhler illumination was done every time the microscope was used (see section.?? and section.??). Köhler illumination was the only method that could be implemented to increase the quality of the images acquired due to limitations in availability of different microscopes and objectives. The 20x and 40x objectives was more than sufficient to observe the yeast cells, but after some calculation on the resolution limits set by the resolution limits of the microscope and the digital CCD sensor chip in the camera it became evident that the size of the yeast cells was close to the limits of the microscope system (microscope and camera) used(see section.3.6.2). Calculations showed that the theoretical limits of resolution in camera plane were $8.4\mu\text{m}$ for the 20x objective and $10.3\mu\text{m}$ for the 40x objective according to the Nyquist sampling theorem. However, in microscopy, it is always possible to gain better resolution but then often enough

when pressing the limitations of the system you lose some other functionality, e.g., it is possible to acquire digital sensors that can detect more light at smaller pixels, but then the framerate of the camera decreases. Another example is using color sensors. If the measurements depend on optical observations with color, it is more than possible but because of the design of each detector (pixel) is larger than a monochromatic sensor you lose light leading to a decrease in resolution (Stuurman, 2018). Therefore as in this thesis, it became vital to customize the system to the size of the yeast cells that were to be measured. The yeast cells varied from 4-6 μm and that is close to the resolution limitations of the microscope setup. Close to the limitation other factors also become more significant and will reduce resolution. Chromatic aberrations is an example (see. appendix ??) where objects can appear blurry the closer you get to the resolution limits. In worst case scenario this can lead to misinterpretation of the measurements. Optical aberrations (appendix. E) was observed throughout all test session, but was not an obstacle in acquiring images of good enough quality to make accurate and correct observations. However, in this thesis, it became very important to get a profound understanding of all aspects of optical microscopy as many of these effects that lower the resolution becomes more and more evident as the resolution limitations of the microscope system are approached. Having this competence, it was possible to distinguish what the image was illustrating and made it possible to conclude with certainty that the observations made was valid.

The ER chamber was produced with substrates that are transparent, making it suitable for both upright and inverted microscopes implying that the selection range of suitable microscopes "doubled". In this thesis, it was a significant advantage due to the accessibility of microscopes at UIO. The microscope was needed for the whole measurement phase which was expected to last one to two months but in the end lasted three months. It was imperative that during the whole measurement phase that the microscope setup was undisturbed as the whole electroration system was integrated with the microscope. This was a time saving factor as the alternative would have been that the integrated microscope/electroration system would be needed to be customized every time it had been altered. This increased the accuracy of the measurements.

5.1.2.2 Suitability of the electroration chamber

The electroration chamber is the hearth of the system. The chamber used in this thesis was acquired from the University of Rostock, and there was no opportunity to alter any of its spec-

ifications or dimensions (for dimensions see section. 3.2.1). It was acquired a total of two chambers from Rostock, so damaging both of them would have had substantial impacts on the progress of this thesis. As a cause of this, the design and handling of the ER chamber were always done with the utmost care.

The electrorotation chamber consists of four equally dimensioned platinum electrodes. Deterioration is always a subject that needs to be monitored when the metal is exposed to an electrolytic solution, and a potential difference is between the electrodes is applied. Platinum is highly resistive against deterioration and corrosion since it is a noble metal (see section.2.1.2.9), but immersed in an electrolyte platinum will always experience oxidation, and over time it will damage the electrodes. This can lead to deformation of the electrodes in such a magnitude that the electric field will be altered and eventually be the cause of an increase in the inhomogeneities in the electric field. This can render the electrorotation chamber unreliable and at utmost unusable (Inhomogeneities in the field give rise to DEP forces exerted on the cell or particle. See section.2.1.2.7 and 2.1.2.2).

The electrolytic effects primarily occur with DC and at low frequencies (1-2 KHz). As explained in section.2.1.2.9 a capacitor can be placed in series in front of the electrode and by that implement a high pass filter removing the DC offset and DC contributions in the signal and the lower frequencies to hinder electrolytic effects and protecting the platinum electrodes. Capacitors of 80nF were implemented on all four signal lines leading to each respective electrode. Calculations were not done for the selected value, but the signal lines were measured on an oscilloscope ensuring that the DC contribution was removed. The calculations were not performed because of the unknown resistance value of the electrodes and in the famous letter from Rostock (figure.5.1) there was a notation of using capacitors with values more significant than 50nF, and the closest capacitor that was possible to acquire was 80nF. This was noticed early in the testing phase and at the same time problems were experienced by formations of gas bubbles in the medium tested under an ER session. This was identified as most likely forming of hydrogen and oxygen gas forming at each respective cathode and anode (see section.2.1.2.9). Even at AC far up in the KHz range heavier ions will not be able to move to the electrode of attractive potential difference, but heavily mobile ions like H^+ and OH^- is still able to migrate to its respective cathode and anode forming hydrogen gas (H_2) and oxygen gas (O_2). When this was discovered sometime in the early test stage, the capacitors were implemented, and it

removed all formation of gas as well as the DC contribution mention above.

In section.2.1.2.7 electric field simulation was presented for different designs of electrodes. In figures. 2.13 and 2.14 calculated field distribution of areas of high field inhomogeneities and the dielectrophoretic force vectors, respectively, are illustrated. Figure (b) in both figures represents the circular electrodes and are similar to the setup used for the ER chamber used in this thesis. The simulation and calculations done by Holzel (1993) were represented in the observation done in this thesis. In dielectrophoresis charged cells or particles migrate to areas of higher or lower field densities (see section.2.1.2.2). Under measurement sessions, it was observed a rapid migration as soon as the power was applied to the supply voltage. Yeast cells migrated to the center of each electrode, to the areas between each adjacent electrode pair and somewhere pushed to the center. Figures. 2.13(b) and 2.14(b) illustrated higher field inhomogeneities in all these areas except the center of the ER chamber but that can be explained by the center of the chamber the electric field is more or less, and no DEP force is affecting the cells. This causes the migrating cells to lose momentum the closer it comes to the center of the chamber. Another mechanism to explain this behavior is that the DEP forces affecting the cells are driven by the inhomogeneities in the electric field. From the studies of Maswiwat et al. (2006) similar simulations as to Holzel (1993). Maswiwat's calculations for round tip electrodes shows how the electric field strength is at its highest in the center along the center line from each parallel electrode. Its only natural to come to the conclusion that some cells will be attracted to the center, but as explained above the closer the cell migrates toward the center of the chamber the more homogeneous the field becomes causing it to lose its momentum (see figure.2.15(a)). In Figure.2.16 field density vectors are presented for six different shapes of electrodes. In figure.2.16(b) the closest similarity to the electrode setup used in this thesis is a design in between R3 and R5 in the figure. However, the electrodes used in this thesis is almost $200\mu\text{m}$ larger in width. The electric field simulations done by Holzel (1993) and Maswiwat et al. (2006) indicates that circular electrode design increases homogeneous field in the center of the chamber. Maswiwat et al. (2006) did a more extensive simulation and implies that an electrode setup with a higher width and round tips is the most appropriate setup due to torque deviation analysis (see figure.2.15). Both studies Holzel (1993) and Maswiwat et al. (2006) corresponds with observations made in the measurements of this thesis.

Due to the field calculations described above and the similarities found for the electrode designs used in this thesis a last but significantly vital factor to discuss is the importance of the electrode chamber is customized to the dimensions of the biological cells or spheroidal particles chosen to be measured. If the chamber is over-dimensioned, it will be unproblematic concerning electrorotation. Small cells or particles will be polarized and a dipole moment will be induced. Most significant factor will likely be a decrease in the field strength as the field strength is proportional to the potential (V) applied divided on the distance (d) between the electrodes $E = V/d$ (which can be positive as it lowers the DEP forces involved due to the induced dipole moment scales with the external field squared for both ER and DEP). However, if the chamber is under-dimensioned according to the size of the cell measured, the areas where the field is homogeneous relative to the size of the cell will decrease. Eventually the field experienced by the cell will become strictly inhomogeneous relative to the size of the cell, and DEP forces will always act upon the cell causing it to migrate to areas of higher or lower field densities, making it impossible to keep the cell in the center of the ER chamber for a continuous electrorotation measurement (see section.2.1.2.2).

A topic that is not covered in this thesis but was observed is cell-to-cell interaction wherein ER two cells often form pairs and in DEP cells form "pearl chains". In the studies of Sancho et al. (2010) it is concluded that formations of "pearl-chains" of cells influenced by DEP may occur and particularly for the frequencies where a transition between positive and negative DEP. For ER experiments Sancho concludes that it was observed that a pair of cells rotates around each other in an orbital pattern. Sancho et al. (2010) has found that this behavior is dependent on the field frequency and the distance between the two cells. Sancho explains that as the distance increases. Sancho claims that when distance another cell is approximately 1.6 times their diameter the torque calculated for an isolated cell differs by ten percent (decrease). The orbital torque between the cells also decreases significantly with an increase in the distance between the cells (Sancho et al., 2010). Similar observations were detected in the test sessions of this thesis and correspond well to the field range described by Sancho et al. (2010) for the formation of "pearl-chains". These observations became more evident as the cell density of the emulsion tested increased. Formation of cell-clusters was observed with increased cell densities between the dispersion as frequency increased described in section.2.1.2.6. This corresponds well to the observation made by Sancho where these pearl chains seemed to form between the transition

between positive and negative DEP which is in the frequency ranges where the transition from the membrane dispersion to the bulk dispersion occurs. It is plausible that the formation of these "clusters" is a result of Sanchos observations. Regarding Sanchos observations concerning the orbital spin between a pair of cells dependent on the distance of separation, it is plausible that the same observations were made in the test sessions as well. Sancho reports that a ten percent decrease was observed in the rotational frequency when a cell pair was at a distance of 1.6 the diameter of the cells. This corresponds well to the derivation of the influential-radius concept of Gimsa (see section.2.1.2.6 and equation. 2.1.25). The influential-radius concept has a factor of 1.5 implying that the cell will attract the equipotential plane that is located at the "influential radii" which is in case of a sphere 1.5 the radius from the cell's symmetry plane which for simplification in Gimsa's theory is set to being 0 V (see figure. 2.4 from Gimsa et al. (2014)). By the support of the theory of the influential-radius concept the cells, if of spherical shape, the cells will attract the equipotential plane of the field 1.5 times their radius making it plausible that the cells will interact with another according to Sancho's observations. The cell-to-cell interaction was observed in this thesis throughout the testing sessions, but all test sessions where interaction between cells occurred more than once per measured frequency was discarded and viewed as a discontinues measurement.

5.1.3 Suitability of yeast samples

In this thesis the chosen test cells for the electrorotation experiments was dry yeast (*Saccharomyces cerevisiae*). In section.3.3 all information surrounding the preparations of the yeast cell emulsions is described. Routines was developed for how long the yeast was kept before discarded and stored. Same routines was developed for the sterile water used throughout this thesis. These routines was implemented to ensure a better accuracy for each testing session and as similar initial starting condition as possible. This segment of the measurement phase could have been significantly improved. Even though the thesis is a feasibility study and the whole project was a "scientific" learning-by-doing process. A more profound understanding should have been acquired earlier in the project on the specific chemical and biological processes occurring when yeast is suspended in water. As the project progressed it became evident that this competence was needed to fully understand the implications it could have on the measurement results. Dry bakers yeast was used because of the simplicity that the yeast cell goes into a "de-

activated” stasis under the drying process for then to become active again when reintroduced to moisture. The dry yeast was chosen due to simplification as many other segments of this thesis demanded full attention. This could have been a huge mistake as the only certain parameter that is possible to easily manipulate in electrorotation experiments on yeast is the conductivity of the external medium which can alter characteristic frequencies and rotation rates (see section.2.1.2.5). In this thesis the spectra obtained probably did not get significantly affected by this as the conductivity measurements (section.4.3). This will be discussed more in detail under 5.2. The facilities where the testing phase was performed was not equipped to perform precision measurements mass or volume as the equipment needed was not available, but these problems was more or less overcome since there was no need for exact cell counts for the yeast emulsions prepared. The significant error done was not washing the cell emulsion numerous times to remove as much as possible of the emulgator (E491) that is the only separate ingredient in the dry yeast used. The emulgator is a non-polar substance and solvable in water (see section.3.3). There has not been measured what impact this emulgator could have on the conductivity in this thesis, but conductivity measurements indicates very small increases in the conductivity levels for the prepared yeast emulsions (see section.4.1). The most significant error that was overlooked was when introducing dry yeast to water the osmotic pressure will cause the cells to increase significantly in size and volume. The yeast cells (*Saccharomyces cerevisiae*) has a flexible membrane and cell wall, so osmotic pressure causing water to drift into the cell is fairly harmless and does not cause many cell deaths (Lodish et al., 2000). Dry yeast cells that get introduced to water and start ”breathing” again will ions and waste products into the external medium, but as the conductivity measurements show the increase in conductivity levels is too significant4.1) indicating that the waste and ion leakage from the yeast cells to the external medium is not so substantial.

5.1.4 Performance deviation due to the amplitude relation of signal and supply voltage for the integrated circuit

The measurements in section. 4.4 presents profound discontinuity when specific relations of V_{cc} and signal input magnitudes are used. After the discovery of this ”abnormal” system behavior, the IC was early singled out as the cause for the problem. It proved difficult to find related literature giving an exact answer for how the IC could still operate with too low supply

voltage. Senior Engineer Stein Nielsen at the ELAB (Electronic Workshop UIO) was consulted, and Nielsen could explain the observed "phenom". Nielsen explains that the reason for the "abnormal" expected behavior lies in how the package surrounding the analog logic circuitry of the dual D Flip-Flop is designed. Nielsen elaborated that in all IC's and circuits there are built in protection mechanisms to shield the logical circuit for and system for sudden fluctuations on input ports. In this case, the very same protection mechanisms were the reason why the IC still could seem to be operating even though it had too low or no supply voltage driving the IC. Some of the built-in protection mechanisms that are relevant in this case are diodes that are used in the package of the IC. The diodes function is to lead damaging fluctuations out of the IC to the Vcc port and protect the IC. This is possible because most voltage supplies have more or less no input impedance. A given an example could be where the signal input carries a sudden rise in voltage of, e.g., 1000V. All of this rise in potential will flow through the Vcc port and to the voltage supply instead of through the IC. It is in this Nielsen explanation lies. In the design of the circuit, a decoupling capacitor was placed close to the IC, as it always should be, to ensure that the IC's have access to steady and even power for operation. In this case, the decoupling capacitor functioned as a battery when the supply voltage was non-existing or too low to power the IC. It was in one of these settings this problem was detected. The Vcc was set to 0V and the amplitude of the signal set to 4 volts which meant that the potential over the protection diode was also then 4 V (3.3 V as silicone diodes has a potential drop of 0.7 V typically). The silicon diode started to lead, and then the decoupling capacitor started to charge. This signal was a square wave leading also to discharge of the capacitor that meant it was pouring energy into the IC. In this case, the combination of the protection mechanisms of the IC and the decoupling capacitor meant for better functionality became the source of errors. A range of measurements was then needed to get a clear and consistent overview of which settings for Vcc and signal input to use to obtain an accurate and stable output signal for testing.

Simplified overview of an IC with protection diode

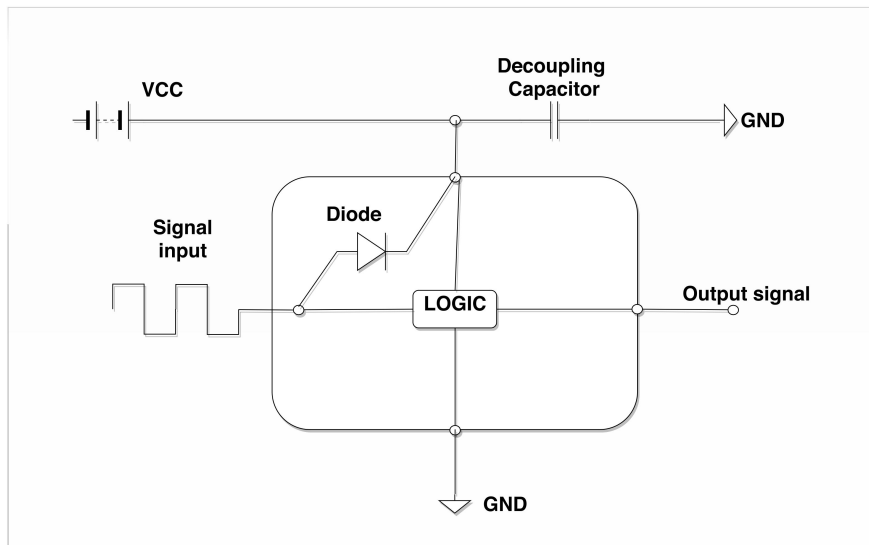


Figure 5.1: Illustration shows how the protection diode is connected to the Vcc terminal. The connection path through the diode, Vcc terminal and further back to the voltage source have more or less no resistance. This will be the path of least resistance and how the diode protects the IC against sudden fluctuations on the signal input.

There was also implemented a decoupling capacitor of $60\ \mu\text{F}$ close to the Vcc input on the device. This capacitor further extended the effects of the "phenom" described above as it prolonged the functionality of the IC capabilities where it should not have been able to operate in the first case. This capacitor could store even more charge and also became a battery to the circuit powering the smaller decoupling capacitor and the IC. The abnormal effect became evident through the measurements. At certain settings for the Vcc and signal input, the frequency and potential started to drop relative to frequency increase. The higher up in the frequency range tested, the larger the decrease in frequency and potential was observed on the output signal. At the "lower" frequencies tested (2kHz to 10 MHz) tested the IC seemed to be functioning normally as the yeast cells were still rotating and the resulting rotation spectra that were obtained had many similarities to specters found in the literature on bakers yeast (e.g., see figure 2.8). The cells rotation rate is expected to start to decrease after the first characteristic rotation peak is passed and further leading into the next dispersion (R_1 to R_2). In this case, the cells rotation rate decreased because the external field amplitude and frequency were decreasing due to the IC's lacking capabilities to follow the increasing signal frequency (not enough voltage). This is why the graphical and visual presentation made it difficult to distinguish. All observations

were showing an expected pattern. The test sequence should have been discarded as all other measurements performed resulting in a discontinuous testing sequence. By comparing the reference spectra from the figure. 2.8 obtained on the same yeast cells to that of the two measured spectra in the figure. 4.11(a) (discontinuous) and figure. 4.11(b)(contentious) it illustrates how difficult it was to distinguish the discontinuous spectrum.

This was proven by soldering different resistors in parallel on to the Vcc input to GND. No change was observed with resistors of significant values ($M\Omega$), but as soon the resistor was in the lower kilo resistance range the effects diminished, and the IC would not function as expected from the start. The reason was that for the lower values of the parallel resistor, the faster it "emptied" the stored charge on the bypass capacitor leading to insufficient power to operate the IC.

Nielsen's explanation was further grounded by reproducing the same effect observed at ELAB. This was realized by using similar passive components equally connected as in the dual D Flip-Flop where it was proven that the signal from the input would charge the decoupling capacitor for then again discharge and power the circuit.

5.2 Measurement analysis of the electrorotation spectra

Figure.5.2 is the same spectrum from figure.4.5 except a calculated curve has been added. the calculated curve is Lorentzian fitted for the calculated values given from the simplified equations for f_{c1} and R_1 from equations.2.1.28 and R_2 and f_{c2} is given from equations.2.1.27. The calculated curve is based on a single-shell model with standard parameters for model calculations. The values used is found in figure.5.3 except for the measured value from the conductivity measurements performed in this thesis was implemented into the derived equations(see table.4.1). The value of $6.4\mu S/cm$ which was measured after ten minutes was chosen. However, it was seldom in the later stages of the measurements on yeast cells that the prepared emulsions was kept any longer than twenty minutes prior to a max of two hours in the earlier stages of the test period before they were discarded The conductivity measurements were performed in the later stages of this thesis as a direct cause to the mistakes done which is explained in section.5.1.3. The yeasts impact on the conductivity levels was not as dramatic as first feared as the table.?? demonstrates. Hölzel and Lamprecht (1992) found no shift in the characteristic

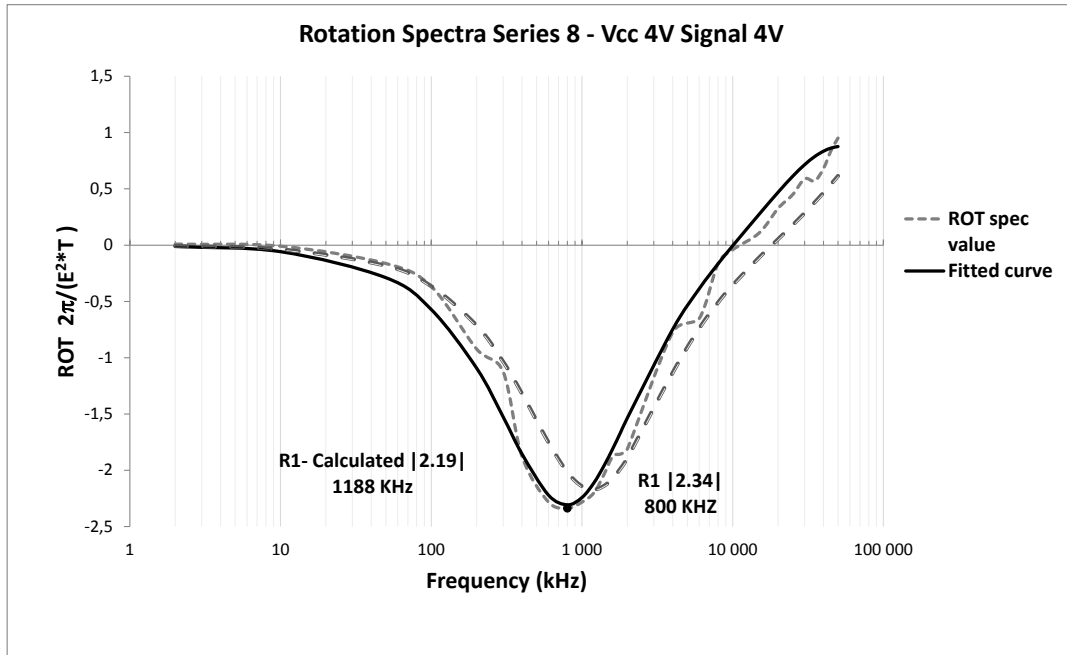


Figure 5.2: Complete series for all frequencies measured for one single cell without any interaction from other cells. Series 8 was measured within the FOV with cell count < 20 . The spectra has been added the calculated spectrum through the characteristic equations from section.2.1.2.6. The calculated curve is Lorentzian fitted for the calculated values for R_1 R_2 f_{c1} and f_{c2}

frequency before the emulsion tested has increased its conductivity levels of almost $300 \mu\text{S/cm}$ so the small changes in the conductivity levels that were observed in the conductivity measurements indicate that it had no significant impact. The calculated curve deviates from the measured values by a higher frequency for the characteristic frequency f_{c1} and have a small but notable lower rotation rate. The parameters used for the calculations are based on the RC models of a single-shell model with the influential radius used for a spherical model (1.5) where the measured curve is based on measurements on a yeast cell that has a cell wall in addition to the membrane which is the only parameter for the single-shell model. The yeast cell will have many more parameters that will deviate from the "ideal" parameters used for the calculation. Best educated guess that can be singled out to explain the increased characteristic frequency and the lower rotation rate is found in equation.2.1.9 which describes the torque the cell experiences. The volume of the yeast cell could be larger than the derivations of the characteristic equations are based on. There was done no dimensional measurements directly on the yeast cells tested

but by observations, the sizes varied. The cells singled out in the measurements were larger in the population. Smaller cells often deviated more in shape and were more difficult to count the number of revolution for. The larger cells were always more circular and varied less in size and shape. In section.5.1.3 it is explained that yeast cells introduced to a solution of almost pure water it will experience osmotic pressure and water will drift into the cell. This causes the cell to substantially increase in size (Lodish et al., 2000). As an educated guess, the larger cells observed had been affected by the osmotic pressure in a larger scale than other cells observed under test sessions. This could be an explanation of how the cells varied in size as well as an explanation as to why the measured cell had a higher rotation rate than that of the calculated. As a last notation, the characteristic equations (equation.2.1.28) could also give another explanation for the lower rotation rate R_1 of the calculated curve because of the conductivity levels used in the calculations could have been of higher value than the external medium in the yeast emulsion measured had. Under measurements, it should have been noted how old the emulsion used was. If the conductivity levels were more or less equal the increased characteristic frequency in the calculated curve according to the measured curve would be directly linked to the membrane. In the calculations, it is used a membrane thickness of 8 nm wherein both Hölzel (1997) and Hölzel and Lamprecht (1992) the membrane of the yeast cells studied is 3 to 4 nm. This would explain the the increase in the characteristic frequency from equation.2.1.28 for f_{c1} .

In figure.2.9 the different dispersions of the ER spectra are illustrated. The first dispersion is where the membrane will be bridged as frequency rises to the bulk dispersion where the membrane is capacitively bridged (See section 2.1.2.6). The acquired Rot spectrum's illustrated in the resulting chapter represents the expected spectrum from 2.9. However, with the signal generator not able to deliver frequencies over 50 MHz the second rotation peak and second characteristic frequency were not possible to obtain. Close to 50 MHz in all spectra obtained for 4 V signal input and 4 V supply voltage the curves show a decrease in rotation rate. This is an indication of the second rotation peak and characteristic frequency. For the spectra obtained for 5 V signal input and 5 V supply voltage, all series show the same indication as for the 4 V spectra except the rotation spectrum Series 7 4.8. Series 7 never passed the to positive values for the rotation. This could be an indication of that the induced dipole moment (equation.2.1.4) never changes sign due to the external media has too high conductivity levels to that of the cytoplasm of the cell. It could also be and sign of the membrane of the cell is breached, and

all inner cytoplasmic content is exchanged with the outer medium causing the dipole moment to become zero. In this case, the cells seem to stop rotating. In the field of view there are over 100 cells so the chance of all cells having their membrane perforated at the same time is highly unlikely. Series 7 (figure.4.8) is most probably a discontinuous spectrum due to loss of signal in the higher frequency range.

Concerning the choice of frequencies that were singled out to plot the electrorotation spectrum after it was made a wrong decision. In the early phase of the testing sessions, it was experienced problems with the evaporation of the test emulsion, so a shorter time frame to complete the measurements was needed. In this period a frequency range was decided upon spread out evenly from 2000 kHz to 50 MHz. This sequence was kept throughout the whole test period. There was not considered that the electrorotation plots were to be plotted logarithmically. Therefore there are fewer data-points in the lower frequencies range than in the higher frequencies. Series 7 (figure.4.8) is a clear indication of this fault. The first two frequencies it was observed a minimal co-field rotation, but the spectra are plotted between the data points and falsely indicate a minimal co-field rotation all the way up to 100 kHz.

The short time frame for the measurements was solved by implementing an extension on top of the electrode chamber made from parafilm. (see section.3.2.3). In the early test phase evaporation was a significant problem. The well on designed into the electrode chamber could not hold enough fluid to complete whole sequences. The construction made from parafilm immediately solved this problem. After the extension of the well was implemented no problems related to evaporation was experienced.

All the measurements performed in this thesis did not result in enough data to do a statistical analysis. The successful tests were too few to do and standard deviation calculations and so forth. The test sets were also reasonably different in the form of the cell count through all measurements. However, the calculated spectra from the characteristic equations built on RC-model for electrorotation fits the measured result, showing a very similar trend and comparing the calculated curve to all spectra obtained it is possible to conclude that electrorotation has been performed on yeast cells and the spectra are valid.

The manual calculation for the characteristic equations is listed in appendix F.

TABLE 1 Standard parameters for model calculations on the single-shell spheroid

Parameter	Value
Axis length along the symmetry axis (c)	$0.5\ \mu\text{m}$ – $50\ \mu\text{m}$
Equatorial radius (r)	$5\ \mu\text{m}$
Membrane thickness (d)	$8\ \text{nm}$
Conductivity	
Internal	$0.53\ \text{S/m}$
Membrane	$10^{-6}\ \text{S/m}$
External	$0.12\ \text{S/m}$
Relative permittivity	
Internal	50
Membrane	9.04
External	80

Figure 5.3: Standard parameters for model calculations on the single-shell spheroid. the table is found in Gimsa and Wachner (1999)

Conclusion and future progress

This thesis proved to be challenging on many fronts as the thesis touched interdisciplinary field drawing on biophysics, cell biology, microscopy and electrical engineering. Electrorotation was an entirely new field, and the background research needed to get a basic introduction to all aspects of the electrokinetic effect was time-consuming. Literature available on electrorotation is minimal concerning published books and material used in general education. Most of the theory needed to acquire the competence to perform, understand and interpret electrorotation was found in several published articles. More or less all of these articles were new frontier research, and many different approaches exist to explain electrorotation. To separate the most direct and relevant material took more time than expected. It was needed to follow the work of some pioneers within the field to get a more continuous and complete understanding of all theory. After almost three months of thorough research, a basic knowledge of most the aspects of electrorotation was obtained. The electrorotation device was designed and prototyped. All initial test proved that the electrorotation device constructed was accurate and fulfilled the requirements needed to perform electrorotation test on particles. The device was finally put to the test on yeast cells, and it was confirmed that the cells rotated with and against the field according to which frequency that was applied. The first goal of this thesis was achieved.

The second primary goal has been to perform electrorotation measurements on yeast cells (*Saccharomyces cerevisiae*), analyze the results and establish a connection to the theoretical concept of electrorotation. As this thesis is a feasibility study, many details concerning the performance of the built electrorotation system were customized as testing was ongoing. The thesis was a scientific learning-by-doing process from start to end, and the understanding of the

theory became more and more profound. Several successful test measurements were obtained even though it proved to be a difficult task. Most test series was discarded due to discontinuous observation and system failure. The most frequent reason for the discontinues spectra obtained was cell migration due to dielectrophoretic effects.

Numerous test sessions were discarded, but due to extensive testing, a good range of successful test series was acquired. The resultant electrorotation spectra were analyzed and compared the results to electrorotation spectra found in published articles there were strong indications that correct electrorotation sequences had been performed.

To validate the results a spectrum was calculated from a set of characteristic equations derived from an RC model describing the transition from the first dispersion (the membrane-bridging dispersion) to the second dispersion (the bulk-conductivity dispersion). Standard parameters for model calculations were used for the calculations in combination with the conductivity measurements for the yeast emulsions used throughout this thesis. The resulting spectra did not deviate significantly, but more importantly, it showed that the measured spectra from the testing session contained all the correct data. The electrorotation spectra obtained in this thesis contained the transition through both dispersions describing electrorotation had been performed on the yeast cell for the given frequency range. This was the proof of concept and electrorotation on yeast cells had been reproduced according to similar electrorotation experiments on yeast cells.

The third optional goal was sadly not possible to investigate. The dimensions of the electrode chamber were not customized to the size of the biomagnetic beads available in this thesis. Two different types were tested. The first was almost ten times as big as the yeast cells and keeping it in a homogeneous field proved impossible and the second type was $1\mu\text{m}$ in diameter. The biomagnetic beads were too small for the microscope camera to distinguish.

Bibliography

Arnold, W. M., Schwan, H. P. and Zimmermann, U. (1987), 'Surface conductance and other properties of latex particles measured by electrorotation', *The Journal of Physical Chemistry* **91**(19), 5093–5098.

URL: <https://doi.org/10.1021/j100303a043>

Berkley (n.d.), 'Nyquist sampling'.

URL: <http://microscopy.berkeley.edu/courses/dib/sections/02Images/sampling.html>

Bohren, C. F. and Huffman, D. R. (1983), *Absorption and scattering of light by small particles*, Wiley. Google-Books-ID: S1RCZ8BjgN0C.

Britannica (2018a), 'Platinum | chemical element'.

URL: <https://www.britannica.com/science/platinum>

Britannica, E. (2018b), 'Refractive index. Definition and Equation'. Online; accessed 03 March 2018.

URL: <https://www.britannica.com/science/refractive-index>

Dalton, C., Goater, A., Burt, J. and Smith, H. (2004), 'Analysis of parasites by electrorotation', *Journal of Applied Microbiology* **96**(1), 24–32.

URL: <http://onlinelibrary.wiley.com/doi/10.1046/j.1365-2672.2003.02113.x/abstract>

Edmundoptics (2018), 'Distortion | Edmund Optics'. Online; accessed 15 March 2018.

URL: <https://www.edmundoptics.com/resources/application-notes/imaging/distortion/>

-
- Gimsa, J. (2001), 'A comprehensive approach to electro-orientation, electrodeformation, dielectrophoresis, and electrorotation of ellipsoidal particles and biological cells', *Bioelectrochemistry* **54**(1), 23–31.
- Gimsa, J. (2018), 'Combined AC-electrokinetic effects: Theoretical considerations on a three-axial ellipsoidal model', *ELECTROPHORESIS* **39**(11), 1339–1348.
URL: <https://onlinelibrary.wiley.com/doi/abs/10.1002/elps.201800015>
- Gimsa, J., Marszalek, P., Loewe, U. and Tsong, T. (1991), 'Dielectrophoresis and electrorotation of neurospora slime and murine myeloma cells', *Biophysical Journal* **60**(4), 749–760.
URL: <http://linkinghub.elsevier.com/retrieve/pii/S0006349591821099>
- Gimsa, J., Stubbe, M. and Gimsa, U. (2014), 'A short tutorial contribution to impedance and AC-electrokinetic characterization and manipulation of cells and media: Are electric methods more versatile than acoustic and laser methods?', *Journal of Electrical Bioimpedance* **5**(1).
URL: <https://www.journals.uio.no/index.php/bioimpedance/article/view/557>
- Gimsa, J. and Wachner, D. (1998), 'A unified resistor-capacitor model for impedance, dielectrophoresis, electrorotation, and induced transmembrane potential', *Biophysical journal* **75**(2), 1107–1116.
- Gimsa, J. and Wachner, D. (1999), 'A Polarization Model Overcoming the Geometric Restrictions of the Laplace Solution for Spheroidal Cells: Obtaining New Equations for Field-Induced Forces and Transmembrane Potential', *Biophysical Journal* **77**(3), 1316–1326.
URL: <http://linkinghub.elsevier.com/retrieve/pii/S000634959976981X>
- Gimsa, J. and Wachner, D. (2001), 'On the analytical description of transmembrane voltage induced on spheroidal cells with zero membrane conductance', *European Biophysics Journal* **30**(6), 463–466.
URL: <http://link.springer.com/10.1007/s002490100162>
- Goddard, W. A., Brenner, D., Lyshevski, S. E. and Iafrate, G. J. (n.d.), *Handbook of Nanoscience, Engineering, and Technology, Third Edition*, CRC Press.
- Grimnes, S. and Martinsen, . G. (2015), *Bioimpedance and bioelectricity basics*, third edition edn, Elsevier/Academic Press, Amsterdam Boston Heidelberg London. OCLC: 892706642.

-
- Grimnes, S., Martinsen, . G. and Schwan, N. H. P. (2002), ‘Interface phenomena and dielectric properties of biological tissue’, *Encyclopedia of surface and colloid science* **20**, 2643–2653.
- Haglund, E. (2017), ‘Sprsml om gjr dere leverer til orkla/ Idun i Norge’.
- Holzel, R. (1993), ‘Electric field calculation for electrorotation electrodes’, *Journal of Physics D: Applied Physics* **26**(12), 2112.
URL: <http://stacks.iop.org/0022-3727/26/i=12/a=003>
- Hölzel, R. (1997), ‘Electrorotation of single yeast cells at frequencies between 100 Hz and 1.6 GHz.’, *Biophysical Journal* **73**(2), 1103–1109.
URL: <https://www.ncbi.nlm.nih.gov/pmc/articles/PMC1181006/>
- Hölzel, R. and Lamprecht, I. (1992), ‘Dielectric properties of yeast cells as determined by electrorotation’, *Biochimica et Biophysica Acta (BBA) - Biomembranes* **1104**(1), 195–200.
URL: <http://www.sciencedirect.com/science/article/pii/000527369290150K>
- ImageEngineering (2018), ‘Longitudinal and lateral chromatic aberration’. Online; accessed 15 March 2018.
URL: <https://www.image-engineering.de/library/technotes/750-longitudinal-and-lateral-chromatic-aberration>
- Jones, T. B. (1984), ‘Quincke Rotation of Spheres’, *IEEE Transactions on Industry Applications* **IA-20**(4), 845–849.
- Kirby, B. J. (2010), *Micro- and Nanoscale Fluid Mechanics: Transport in Microfluidic Devices*, Cambridge University Press.
- Lamb, H. S. (1906), *Hydrodynamics*, 3d ed. – edn, Cambridge University Press.
URL: <http://openlibrary.org/books/OL7028832M>
- Lodish, H., Berk, A., Zipursky, S. L., Matsudaira, P., Baltimore, D. and Darnell, J. (2000), ‘Osmosis, Water Channels, and the Regulation of Cell Volume’, *Molecular Cell Biology*. 4th edition .
URL: <https://www.ncbi.nlm.nih.gov/books/NBK21739/>
-

Lovelace, R. V. E., Stout, D. G. and Steponkus, P. L. (1984), 'Protoplast rotation in a rotating electric field: The influence of cold acclimation', *The Journal of Membrane Biology* **82**(2), 157–166.

URL: <https://link.springer.com/article/10.1007/BF01868940>

Ltd., J. T. (2018), 'How To Calibrate 10x Probe'.

URL: <https://jyotech.com/Support/HowToCalibrate10xProbe.pdf>

Maswiwat, K., Holtappels, M. and Gimsa, J. (2006), 'On the field distribution in electrorotation chambers Influence of electrode shape', *Electrochimica Acta* **51**(24), 5215–5220.

URL: <http://linkinghub.elsevier.com/retrieve/pii/S0013468606002866>

Medical, U. (2018), 'Parafilm Sealing Film - 50mm (2") Film Width x Roll Length 75m'.

URL: <https://www.universalmedicalinc.com/parafilm-sealing-film-50mm-2-film-width-x-roll-length-75m.html>

Mortimer, Abramowitz, M. W. and Davidson (2018), 'Anatomy of a Microscope and Optical Aberrations'. Online; accessed 15 March 2018.

URL: <https://www.olympus-lifescience.com/en/microscope-resource/primer/anatomy/>

Nandi, P. (2013), 'Effect of alternating current on electrolytic solutions', *IOSR Journal of Engineering* **03**(08), 52–59.

URL: [http://www.iosrjen.org/Papers/vol3_issue8%20\(part-2\)/I03825259.pdf](http://www.iosrjen.org/Papers/vol3_issue8%20(part-2)/I03825259.pdf)

Nikon (2018a), 'Immersion Oil and Refractive Index'. Online; accessed 06 March 2018.

URL: <https://www.microscopyu.com/tutorials/immersion>

Nikon (2018b), 'Nikon | Microscope Solutions | What is aberration?'. Online; accessed 16 March 2018.

URL: <http://www.nikon.com/products/microscope-solutions/explore/microscope-abc/learn-more-microscope/aberration/index.htm>

Olympus (2018a), 'The Köhler Illumination'. Online; accessed 02 Feb 2018.

URL: <https://www.olympus-lifescience.com/en/microscope-resource/primer/anatomy/kohler/>

Olympus (2018b), 'Microscope Optical Components - Immersion Media'. Online; accessed 06 March 2018.

URL: <https://www.olympus-lifescience.com/en/microscope-resource/primer/anatomy/immersion/>

Olympus and Spring, K. R. (2018), 'Airy Patterns and the Rayleigh Criterion - Java Tutorial'. Online; accessed 10 March 2018.

URL: <https://www.olympus-lifescience.com/en/microscope-resource/primer/java/imageformation/rayleighdisks/>

Osborn, J. A. (1945), 'Demagnetizing Factors of the General Ellipsoid', *Physical Review* **67**(11-12), 351–357.

URL: <https://link.aps.org/doi/10.1103/PhysRev.67.351>

Paul, R. and Otwinowski, M. (1991), 'The theory of the frequency response of ellipsoidal biological cells in rotating electrical fields', *J. Theor. Biol* **148**, 495–519.

Pethig, R. (2017), *Placing Dielectrophoresis into Context as a Particle Manipulator*, Wiley-Blackwell, chapter 1, pp. 1–29.

URL: <https://onlinelibrary.wiley.com/doi/abs/10.1002/9781118671443.ch1>

Pethig, R. and Willis, M. R. (1980), 'Dielectric and electronic properties of biological materials by R Pethig. pp 376. John Wiley & Sons, Chichester and New York. 1979. 15', *Biochemical Education* **8**(1), 31–31.

URL: <https://onlinelibrary.wiley.com/doi/abs/10.1016/0307-441228802990102-8>

Philips (2003), '74hc74; 74hct74 Dual D-type flip-flop with set and reset; positive-edge trigger', p. 22.

URL: <https://www.westfloridacomponents.com/mm5/graphics/ds7/74HC74D.pdf>

Pubchem (2018), 'Sorbitan monostearate'.

URL: <https://pubchem.ncbi.nlm.nih.gov/compound/3793749>

Qian, C., Huang, H., Chen, L., Li, X., Ge, Z., Chen, T., Yang, Z. and Sun, L. (2014), 'Dielectrophoresis for Bioparticle Manipulation', *International Journal of Molecular Sciences*

15(10), 18281–18309.

URL: <http://www.mdpi.com/1422-0067/15/10/18281>

Sancho, M., Martnez, G., Muoz, S., Sebastin, J. L. and Pethig, R. (2010), ‘Interaction between cells in dielectrophoresis and electrorotation experiments’, *Biomicrofluidics* **4**(2).

URL: <https://www.ncbi.nlm.nih.gov/pmc/articles/PMC2917873/>

Sauer, F. A. and Schögl, R. W. (1985), in A. Chiabrera, C. A. Nicolini, H. P. Schwan and N. A. T. O. S. A. Division, eds, ‘Interactions between electromagnetic fields and cells’, Published in cooperation with NATO Scientific Affairs Division [by] Plenum Press, New York, p. 203.

Schwan, H. P. (1957), in J. H. Lawrence and C. E. Tobias, eds, ‘Advances in Biological and Medical Physics’, Academic Press, New York, p. 157.

Schwan, H. P. (1985), ‘Dielectric properties of the cell surface and biological systems’, *Stud. Biophys* **110**, 13.

Scientifica (n.d.).

Sigma (2018), ‘p7668pis.pdf’.

URL: <https://www.sigmaaldrich.com/content/dam/sigma-aldrich/docs/Sigma/ProductInformationSheet/>

Silfies, J. S., Schwartz, S. A. and Davidson, M. W. (2018), ‘The Diffraction Barrier in Optical Microscopy’. Online; accessed 10 March 2018.

URL: <https://www.microscopyu.com/techniques/super-resolution/the-diffraction-barrier-in-optical-microscopy>

Sokirko, A. (1992), ‘The electrorotation of axisymmetrical cell’, *Biol. Membr.* **6**, 587–600.

Stille, U. (1944), ‘Der Entmagnetisierungsfaktor und Entelektrisierungsfaktor fr Rotationsellipsoide’, *Archiv fr Elektrotechnik* **38**(3-4), 91–101.

URL: <https://link.springer.com/article/10.1007/BF02092674>

Stoner, E. C. (1945), ‘XCVII. The demagnetizing factors for ellipsoids’, *The London, Edinburgh, and Dublin Philosophical Magazine and Journal of Science* **36**(263), 803–821.

URL: <https://doi.org/10.1080/14786444508521510>

Stuurman, N. (2018), ‘Cameras and Digital Image Analysis’.

URL: <https://www.ibiology.org/talks/digital-image-analysis/>

Texwipe (2018), ‘Texwipe’.

URL: <https://www.texwipe.com/>

Wilson, M. (2016), ‘Microscope Resolution: Concepts, Factors and Calculation’.

URL: <https://www.leica-microsystems.com/science-lab/microscope-resolution-concepts-factors-and-calculation/>

Wilson, M. (2017), ‘Eyepieces, Objectives and Optical Aberrations’. Online; accessed 15 March 2018.

URL: <https://www.leica-microsystems.com/science-lab/eyepieces-objectives-and-optical-aberrations/>

Yamaguchi, M., Namiki, Y., Okada, H., Mori, Y., Furukawa, H., Wang, J., Ohkusu, M. and Kawamoto, S. (2011), ‘Structure of *Saccharomyces cerevisiae* determined by freeze-substitution and serial ultrathin-sectioning electron microscopy’, *Microscopy* **60**(5), 321–335.

URL: <https://academic.oup.com/jmicro/article-lookup/doi/10.1093/jmicro/dfr052>

Zeiss (2018a), ‘Configure your Condenser Numerical Aperture easily’. Online; accessed 04 Feb 2018.

URL: <https://www.zeiss.com/microscopy/us/solutions/reference/all-tutorials/basic-microscopy/condenser-numerical-aperture.html>

Zeiss (2018b), ‘Discover the Concepts of Resolution and Numerical Aperture’. Online; accessed 04 Feb 2018.

URL: <https://www.zeiss.com/microscopy/us/solutions/reference/basic-microscopy/numerical-aperture-and-resolution.html>

Zeiss (2018c), ‘The Köhler Illumination: Basic Knowledge and How Do I’. Online; accessed 02 Feb 2018.

URL: <https://www.zeiss.com/microscopy/us/solutions/reference/basic-microscopy/koeher-illumination.html>

Appendix

A First appendix - The depolarizing factors

Brought from (Gimsa, 2001) he states that to his knowledge the depolarizing factors was first derived for spheroids by (Stille, 1944) in 1944. The depolarizing factors for the general ellipsoid was published completely separate and independent of Stille's work in 1945 by (Stoner, 1945) and (Osborn, 1945).

With the three principal axes of a general ellipsoid a, b and c and where $a > b > c$ the depolarizing factors n_a, n_b and n_c are dependent on the axis-ratio $\beta = \frac{b}{a}$ and $\delta = \frac{c}{a}$ and expressions are given for n_a, n_b and n_c :

$$\begin{aligned} n_a &= \frac{\beta\delta}{\sqrt{1-\delta^2}(1-\delta^2)} (LF(\kappa, \psi) - LE(\kappa, \psi)) \\ n_b &= -n_a + \frac{\beta\delta}{\sqrt{1-\delta^2}(\beta^2-\delta^2)} LE(\kappa, \psi) - \frac{\delta^2}{\beta^2-\delta^2} \\ n_c &= -\frac{\beta\delta}{\sqrt{1-\delta^2}(\beta^2-\delta^2)} LE(\kappa, \psi) + \frac{\beta^2}{\beta^2-\delta^2} \end{aligned} \quad (A1)$$

LE and LF are elliptical integrals of the functions of κ and ψ which there again depends on the axis ratios:

$$\kappa = \sqrt{\frac{1-\beta^2}{1-\delta^2}}, \quad \text{and} \quad \psi = \arccos(\delta) \quad (A2)$$

Elliptical integrals follows:

$$\begin{aligned} LE(\kappa, \psi) &= \int_0^\psi \sqrt{1-\kappa^2 \sin^2(\phi)} d\phi \\ LF(\kappa, \psi) &= \int_0^\psi \frac{1}{\sqrt{1-\kappa^2 \sin^2(\phi)}} d\phi \end{aligned} \quad (A3)$$

With spheroids with two equal axes a and b it is possible to obtain explicit expressions. Oblate form of the spheroid where $a > c$ along one of the axis perpendicular to the symmetry axis one depolarization factor obtains:

$$n_a = \frac{1}{2} \left[1 - \frac{1+e^2}{e^3} (e - \arctan e) \right] \quad \text{where}$$

$$e = \sqrt{\left(\frac{a}{c}\right)^2 - 1} \quad (\text{A4})$$

and for prolate cases where $a < c$:

$$n_a = \frac{1}{2} \left[1 - \frac{1-e^2}{2e^3} \left(\ln \frac{1+e}{1-e} - 2e \right) \right] \quad \text{where}$$

$$e = \sqrt{1 - \left(\frac{a}{c}\right)^2} \quad (\text{A5})$$

In equations (A4) and (A5), e notes the eccentricity of the spheroid. In all cases of the shape of the general ellipsoid, oblate formed or prolate, the sum of the depolarizing factors along the three principal axes are always in unity ($n_a + n_b + n_c = 1$). Along the symmetry axis the depolarizing factor is $n_c = 1 - 2n_a$.

B Second appendix - Equipment used in thesis

Equipment descriptions and materials		
Name	Manufacturer	Description
MSO 2024B	Tektronix	Mixed signal oscilloscope
HMO 1024 100MHz	Rohde and Schwarz	Oscilloscope
HMF 2550	Rohde and Schwarz	50 Mhz Arbitrary Signal Generator
Hameg Hz 36	Hameg	Oscilloscope Probe with 10x dampener
Ps3 - 30SW CV - CC	Unknown	Powersupply CV - CC
Fluke 75	Fluke	Multimeter
M205 C	Leica	Microscope used with camera MC170 HD used only for dimension measurements
CX41	Olympus	Optical Microscope with 6v 30W halogen light source (upwards)
PLanC 20x	Olympus	Magnification: 20x, Numerical Aperture: 0,40, Tube length: infinity, Coverslip thickness: 0,17, Field number: 22
Olympus 40x	Olympus	Magnification: 50x, Numerical Aperture: 0,65, Tube length: infinity, Coverslip thickness: 0,17
DMK 41BU02	Imagingsource	Digital camera : 1/2 inch Sony CCD sensor 1,280960 (1.2 MP), up to 15 fps camera, monochrome
Aqua B. Braun	B. Braun	Sterile water 50 ml Ecocontainer

Dry Yeast (Bakers yeast)	Idun	Dry yeast containing E491 Sorbitan monostearate
VLC media player	VideoLan Organization	Video media player, version 2.2.1 Terry Pratchett
CADSTAR 17.0	Zuken	PCB Design Software
IC Capture 2.4.642.2631	Imagingsource	Image acquisition software for microscope camera
Ethanol CAS No. 64-17-5	Vitlab	Technical ethanol
Parafilm 4 inch	Sigma-Aldrich	Parafilm used to enhance the electrode well volume
Multifunction-Target DA030	Max Levy Autograph INC	Calibration tool for microscope
Vertex Pre-Wetted TX42P	Texwipe	Certified Pre-wetted clean-room wipes. 70%isopropyl, 30%deionized water.
Vertex High Durability TX29	Texwipe	Cleanroom certified dry wipes.
ESD-Safe TX750E	Texwipe	Cleanroom certified swabs. Mini conical tip.
Lens Cleaning Paper	Tiffen	Lens cleaning sheets. Lintless paper prepared for cleaning highly polished glass surfaces.
EL3 Portable Conductivity Meter	Mettler Toledo	Combined PH and conductivity meter.
LE703 Conductivity probe	Mettler Toledo	Probe for medium to high conductivity measurements (10 μ S/cm to 200 mS/cm).
Mettler AE 260	Mettler	Analytical balance with an accuracy of 1 mg \pm 0.1mg

Parafilm M	Universal Medical	Acrylic sealing film meant for laboratory purposes
------------	-------------------	--

Table 6.1: Equipment list (appendix)

C Third appendix - Data sheet for Idun dry bakers yeast

12.09.2017 07:15:37

1 / 2



IDUN INDUSTRI A.S



180 Salgsdatablad/01 Gjær/01 Fersk gjær

SDB-01-0 TQM
1-80011 Godkjente
rev: 03 bøker 1.8
(OSLMG007)

Dokument tittel: Gjær fersk original blå, kartong 12 kg 80011

PRODUKTBESKRIVELSE:

Produksjon av pressgjær innebærer at man legger forholdene til rette slik at gjæren kan vokse og formere seg. Til dette trenger den næring, og gjærens næring består av sukker, gjødningsstoffer, vitaminer og mineraler. Disse stoffene utgjør råvarene for produksjonen. Etter avsluttet vekst blir det fjernet vann, slik at gjæren får en konsistens som egner seg for pakking.

Pressgjær brukes som hevemiddel i all gjærbakst.

BRUKSANVISNING/DOSERING:

Fersk Gjær Original brukes i brød og lettere deiger, deig uten tilsatt sukker eller deiger med en sukkermengde opptil 4% av melmengden.

OPPRINNELSESLAND:

Sverige

INGREDIENSER (fet skrift angir at ingrediensen inneholder et allergen):

Gjær

Allergener:

Ingen

NÆRINGSVERDIER PER 100 GRAM:

Energi (kJ/kcal)	452 / 108
Fett (g)	1,7
derav mettet (g)	0,3
derav enumettet (g)	
derav flerumettet (g)	
Karbohydrater (g)	6
derav sukkerarter (g)	4,4
Kostfiber (g)	8,1
Protein (g)	13
Salt (g)	0,05
Natrium (g)	

KJEMISKE FORURENSNINGSTOFFER:

(Untitled)

D Fourth appendix -Electrorotation test-sessions for completed and non-completed testing series on yeast

Electrorotation test-sessions Completed / Discarded			
Vcc/Signal (V)	Series name	Completion	Comments
4V / 4 V	Test series	Discarded	Test series
2.5V / 3V	Test 2- Series 2	Discarded	Inconsistent field frequencies
2.5V / 3V	Test 3- Series 2	Discarded	Inconsistent field frequencies and formation of gas bubbles in the end
2.5V / 3V	Test 4- Series 2	Discarded	Inconsistent field frequencies, gas bubble detection, uncompleted freq.range
4V / 4 V	Test package	Discarded	Completed, cell-to-cell interaction
4V / 4 V	Yeast Series 1	Completed	Cells <20
4V / 4 V	Yeast Series 2	Completed	Cells>>20
4V / 4 V	Yeast Series 3	Discarded	Cells>>>20, cell-to-cell interaction
4V / 4 V	Yeast Series 4	Completed	Cells<20
4V / 4 V	Yeast Series 5	Discarded	Cells>>>20, cell-to-cell interaction, cell migration
4V / 4 V	Yeast Series 6	Discarded	Incomplete, cell migration
4V / 4 V	Yeast Series 7	Completed	Cells<20 , cell-to-cell interaction, consistent
4V / 4 V	Yeast Series 8	Completed	Cells<20
5V / 5V	Yeast Series 1	Discarded	Cells ;20, cell migration, incosistent
5V / 5V	Yeast Series 2	Completed	Cells<20
5V / 5V	Yeast Series 3	Completed	Cells<20

5V / 5V	Yeast Series 4	Discarded	Cells<20, cell migration, incosistent, in-mobile cells
5V / 5V	Yeast Series 5	Discarded	Cells<20, aborted sequence due to cell migration
5V / 5V	Yeast Series 6	Discarded	Cells<20, cell migration, cell clustering
5V / 5V	Yeast Series 7	Completed	Cells>>20, complete through sequence, some distance from dead center
5V / 5V	Yeast Series 8	Discarded	Cells>>>20, cell-to-cell interactio, cell migration
5V / 5V	Yeast Series 9	Discarded	Cells>>>20, inconsistent
5V / 5V	Yeast Series 10	Discarded	Cells>>20, cell migration, inconsistent
5V / 5V	Yeast Series 11	Completed	Cells >>>20, cell-to-cell interaction between 10 to 30 MHz, consistent

Table 6.2: Electrorotation test-sessions for completed and non-completed series on yeast (appendix)

E Fifth appendix - Additional theory regarding the art of microscopy

Köhler illumination

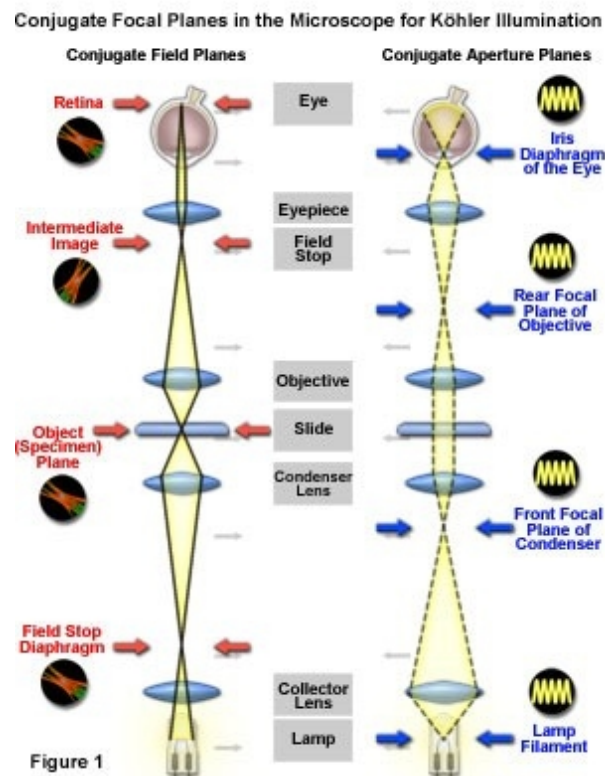


Figure 6.1: Figure above (Zeiss, 2018c) represents the separate light pathways for the specimen illuminating light rays and image forming light rays. This is not a true representation concerning any real separation or segregation of these pathways but meant for visualisation. However the figure illustrates the conjugate field and aperture planes that are critical to properly obtain illumination throughout the microscopes focus areas and obtain Köhler illumination.

The parallel light-rays that pass and are transmitted through the specimen are focused at the back of the focal plane of the objective. This is where the image from the variable condenser aperture and the light source will be seen. The area of the focal plane and throughout the microscope system all other areas that are in common focus Köhler illumination. An object that is in focus in one of these planes are in focus in all of the other conjugate planes. The conjugate planes are divided into four separate planes for imaging and illumination pathways of the projected light from the lamp filament. These four planes together make up the conjugate plane set (image-forming and illumination)

Conjugate planes in the path of the illuminating light rays in Köhler illumination:

-
- Lamp filament
 - Condenser aperture diaphragm (front of the focal plane condenser)
 - Back focal plane of the objective
 - The eye point of the eyepiece (also called Ramsen disk)

Conjugate planes in the image-forming light path in Köhler illumination:

- Field diaphragm
- Focused specimen
- The intermediate image plane (the plane of the fixed diaphragm of the eye piece)
- Retina of the eye or the film plane of the camera

Optical Aberrations

The definition of aberration concerning optics is *"Distortion of an image from the ideal optical image is called aberration. An ideal optical image satisfies the following three conditions.*

- 1. A point object creates a point image.*
- 2. A plane object perpendicular to the optical axis creates a plane image.*
- 3. A figure on a plane perpendicular to the optical axis creates an image similar to that figure."*

(Nikon, 2018b)

There are two main types of optical aberrations in terms of microscopy. Chromatic aberrations and geometrical aberrations (also known as spherical, monochromatic or Seidel Aberrations). Aberrations occur due to errors in lenses are an unfortunate problem that arises when light waves interact with glass lenses. Optical aberrations will cause induced faults in the features to the image viewed through a microscope. Anti reflective coatings, advanced new construction techniques and new modern glass formulations has more or less eliminated most aberrations from today's objectives. Nonetheless it is important to pay attention to these effects,

especially when quantitative high-magnification video or photo microscopy is concerned. Geometrical aberrations are mainly related to the spherical nature of the lens(es) and approximations used to obtain the Gaussian lens equation. Chromatic aberrations arise from the variations of refractive indices each of the different frequencies visible light is composed of. (Mortimer et al., 2018)

Geometrical Aberration

Geometrical aberrations is mainly divided into five constituents (spherical, coma, astigmatism, distortion and curvature of field). Lenses used in microscopy are curved. Light waves passing through the lens at the centre will be refracted less than the waves passing through closer to the outer edge. Light waves that was parallel before entering the lens will not converge to one common focus point because of this but will be spread as different focus points along the optical axis (Wilson, 2017). Microscope manufacturer Nikon explains the constituents of geometrical aberrations (Nikon, 2018b):

Spherical: Spherical aberration is independent to the field of view (FOV) and is proportional to the NA to the power of three. It appear as a circular blur and is the only aberration that appears also in the centre of the field of view. Spherical aberration is the source of all kinds of aberrations.

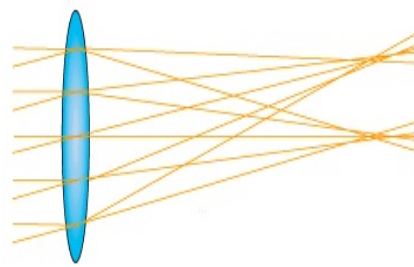


Figure 6.2: Spherical aberration can occur both in longitudinal and transverse orientation.

Coma: This aberration is linearly to the width of the FOV and proportional to the square of the NA. The centre of the FOV is sharp, but as you approach the edge of the FOV the image becomes more and more blurred. This blurriness is similar to a comet-shaped blur, hence the name Coma.

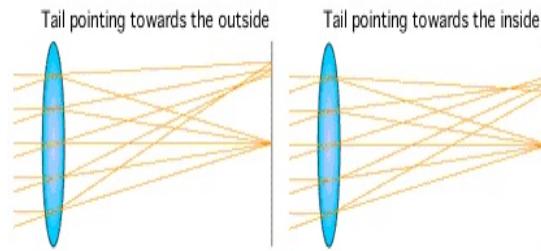


Figure 6.3: As coma aberration is referred to as comet-shaped blur it is said that the aberration has a tail either pointing inwards or opposite.

Astigmatic: This aberration is linearly proportional to the NA and the square of the width of the FOV. Astigmatic aberration is proportional to the NA and proportional to the square of the FOV. Astigmatic aberration depends more strongly on the oblique angle of light beams entering the objective. The aberration is rooted in the off-axis image. A point of light from a specimen will appear as a line or an ellipse and dependent on the oblique angle of light entering the lens the line/ellipse image may be oriented in two different directions, tangential or sagittal.

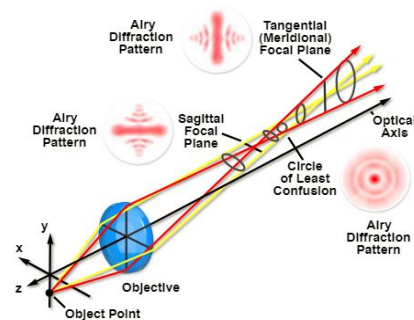


Figure 6.4: Astigmatic aberration presented by the principal axes of the tangential and sagittal light rays and shows how Airy patterns are distorted at given strategic locations of the path of the light waves.

COF: This aberration is proportional to NA and FOV like Astigmatic aberration. Curvature of field becomes more and more prominent as the FOV widens. It is a circular blur emanating outward from the focal point and from the centre as the focal point is moved.

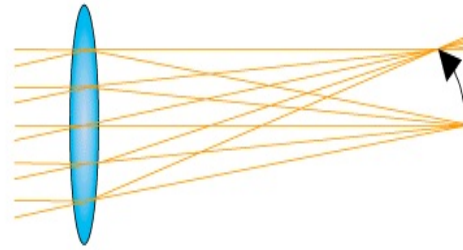


Figure 6.5: As the image plane is moved along the optical axis the circular blur will appear either at the edges or the centre of the image.

Distortion: This aberration is proportional to the width of the field to the power of three and independent of the NA. Distortion is the only aberration without blur. Distortion will not affect image quality in it self and is independent from other forms of aberrations. Distortion describes *"the magnification in an image changes across the field of view at a fixed working distance"*(Edmundoptics, 2018).

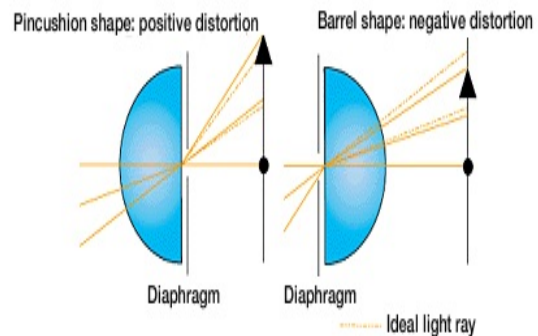


Figure 6.6: Distortion aberration is an effect where "objects" in the image will be represented differently within the same magnification. Rectangular distorted shapes are formed.

Chromatic Aberrations

Chromatic aberration is a defect related to that visible or white light is composed of different wavelengths of light. White light passing through a lens will experience refraction. The different wavelengths will be refracted according to their frequency. Blue light will be refracted at the greatest extent followed in succession by the other wavelengths of the white light's numerous components. Red is the least refracted. This phenomenon is often referred to as dispersion. Therefore, a lens lacks the ability to gather all wavelengths to a common focus, resulting in a slightly different image size and different focal points for each of the wavelength groups. As a result of this, coloured fringes surrounding the image will occur. When each wavelength forms its

own independent focal point along the optical axis of the lens its called longitudinal chromatic aberration. With a lens system not corrected for chromatic aberration a image focused in the blue plane will have objects ringed by red and green. The other part of chromatic aberration is called lateral chromatic aberration. This defect is a dependency of the longitudinal effect. This defect will appear as the point images of detail nearer the periphery of the FOV will be of different size. This defect is explained by the off-axis(optical) light rays fluxes are dispersed passing through the lens and causes the different components of wavelengths to form images at different heights onto the image plane. In white light a blue image detail is viewed slightly larger than that of a green or red detail. This results in colour ringing of the specimen details in the outer region of the FOV. A lens with lateral chromatic aberration illuminated by white light will produce a series of images of the different colour that is overlapped and varying in size (Mortimer et al., 2018).

Figures below are copyrighted by Image Engineering (ImageEngineering, 2018) and illustrates longitudinal and lateral chromatic aberration due to the angle of incident white light through a lens.

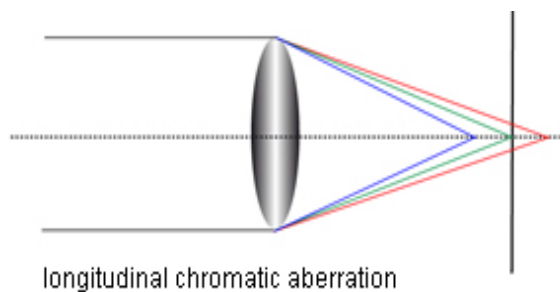


Figure 6.7: Longitudinal chromatic aberration is caused by straight incident white light. The different colour focal planes is placed along the optical axis in longitudinal direction according to the different frequencies of wavelengths. Image source: (ImageEngineering, 2018)

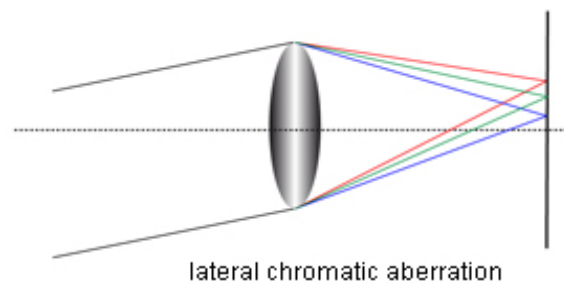


Figure 6.8: Obliquely incident white light passing through the lens causes lateral chromatic aberration. All colours in this aberration are in focus in the same plane, but focused in the same foci. Image source: (ImageEngineering, 2018)

F Sixt appendix - Calculations of characteristic equations based on RC models

TABLE 1 Standard parameters for model calculations on the single-shell spheroid

Parameter	Value
Axis length along the symmetry axis (c)	0.5 μm –50 μm
Equatorial radius (r)	5 μm
Membrane thickness (d)	8 nm
Conductivity	1200 $\frac{\mu\text{S}}{\text{cm}}$
Internal Membrane	0.53 S/m
External Membrane	10^{-6} S/m
Relative permittivity	4–12 S/m
Internal	50
Membrane	9.04
External	80

$$R_1 = \frac{-1.5 \sigma_i}{(2\sigma_e + \sigma_i) \cdot \left[\ln \left(\frac{1}{\sigma_e} + \frac{2}{\sigma_i} \right) + 2 \right]}$$

$$= \frac{-1.5 \cdot 0.53}{(2 \cdot 0.64 + 0.53) \cdot \left[\ln \left(\frac{1}{0.64} + \frac{2}{0.53} \right) + 2 \right]}$$

$$= \frac{-0.795}{(1.81) \cdot [6.25 \cdot 10^{-5} \cdot (1.5125 + 3.773) + 2]}$$

$$= \frac{-0.795}{1.81 \cdot 2.0003335} = -6.219$$

$$g = \frac{\sigma_m}{d} = \frac{10^{-6}}{8 \cdot 10^{-9}} \cdot 5 \cdot 10^{-4} \cdot 0.97 = \frac{6.25 \cdot 10^{-5}}{8 \cdot 10^{-9}} = 7.8125 \cdot 10^{-3}$$

$$C = \frac{\epsilon_0 \cdot \epsilon_m}{d} = \frac{8.85 \cdot 10^{-12}}{8 \cdot 10^{-9}} = 1.10625 \cdot 10^{-3}$$

Figure 6.9: First rotation peak (R1)

Figure 10: Second rotation peak (R2)

$$\delta_{z0.5} R_2 = \frac{(8+1)^2 \cdot (\delta_i \epsilon_e - \epsilon_i \delta_e)}{2(\delta_e + \delta \delta_i)(\epsilon_e + \epsilon \epsilon_i)}$$

$$= \frac{(0.5+1)^2 \cdot (0.53 \cdot 80 - 50 \cdot 0.64)}{2 \cdot (0.44 + 0.5 \cdot 0.53)(86 + 0.5 \cdot 50)}$$

$$= \frac{2.25 \cdot (10.4)}{2 \cdot (0.905) \cdot (105)}$$

$$= \frac{23.4}{190.05} = \underline{\underline{0.123}}$$

$$C = 1,0005 \cdot 10^{-2}$$

$$g r = 6.25 \cdot 10^{-4}$$

TABLE 1 Standard parameters for model calculations on the single-shell spheroid

Parameter	Value
Axis length along the symmetry axis (c)	0.5 μm-50 μm
Equatorial radius (r)	5 μm
Membrane thickness (d)	8 nm
Conductivity	
Internal	0.53 S/m
Membrane	10 ⁻⁶ S/m
External	0.12 S/m
Relative permittivity	
Internal	50
Membrane	9.04
External	80

Figure 6.11: First characteristic frequency (f_{c1})

TABLE 1 Standard parameters for model calculations on the single-shell spheroid

Parameter	Value
Axis length along the symmetry axis (c)	0.5 μm –50 μm
Equatorial radius (r)	5 μm
Membrane thickness (d)	8 nm
Conductivity	
Internal	0.53 S/m
Membrane	10^{-6} S/m
External	0.12 S/m
Relative permittivity	
Internal	50
Membrane	9.04
External	80

$$f_{c1} = \frac{1}{2\pi r c} \cdot \left(\frac{1}{\frac{1}{2\sigma_e} + \frac{1}{\sigma_i}} + r g \right)$$

$$f_{c1} = \frac{1}{2\pi \cdot 5 \cdot 10^{-6} \cdot 1005 \cdot 10^{-2}} \cdot \left(\frac{1}{0.728125 + 1.8467} + 6.25 \cdot 10^{-4} \cdot r \cdot \frac{\sigma_e}{\sigma_i} \right) \cdot \frac{5 \cdot 10^{-6} \cdot 10^{-6}}{8 \cdot 10^{-9}} = 6.25 \cdot 10^{-4}$$

$$c = \frac{60 \cdot 3m}{8.8 \cdot 10^{-12} \cdot 904} = 8 \cdot 10^{-9}$$

$$= 1.005 \cdot 10^{-2}$$

$$= 1188255288.11$$

$$= 1188.23 \text{ kHz}$$

$$\begin{aligned}
 f_{c2} &= \frac{1}{2\pi\epsilon_0} \cdot \left(\frac{\sigma_e + 8 \cdot \sigma_i}{\epsilon_0 + 8 \cdot \epsilon_i} \right) \\
 &= \frac{1}{2\pi \cdot 8.85 \cdot 10^{-12}} \cdot \left(\frac{0.64 + 0.5 \cdot 0.53}{80 + 0.5 \cdot 50} \right) \\
 &= \frac{1}{2\pi \cdot 8.85 \cdot 10^{-12}} \cdot (8.61904 \cdot 10^{-3}) \\
 &= 155\,001\,448.7 \\
 &= \underline{\underline{155\,001.45\text{ kHz}}}
 \end{aligned}$$

TABLE 1 Standard parameters for model calculations on the single-shell spheroid

Parameter	Value
Axis length along the symmetry axis (<i>c</i>)	0.5 μm-50 μm
Equatorial radius (<i>r</i>)	5 μm
Membrane thickness (<i>d</i>)	8 nm
Conductivity	
Internal	0.53 S/m
Membrane	10 ⁻⁶ S/m
External	0.12 S/m
Relative permittivity	
Internal	50
Membrane	9.04
External	80

Figure 6.12: First characteristic frequency (Fc2)